

Compact Helical Antenna for Smart Implant Applications

DISSERTATION

von der Fakultät für Elektrotechnik und Informationstechnik
der Technischen Universität Chemnitz

zur Erlangung des akademischen Grades

Doktor der Ingenieurwissenschaften

(Dr. Ing.)

Vorgelegt

von: **M. Sc. Dmitriy D. Karناushenko**

Geboren am: **04. März 1986 in Novokuznetsk**

Eingereicht am: **22.05.2017**

Gutachter: **Prof. Dr. Oliver G. Schmidt**

Prof. Dr. Frank Ellinger

Tag der Verleihung: **19.10.2017**



Leibniz Institute
for Solid State and
Materials Research
Dresden



TECHNISCHE UNIVERSITÄT
CHEMNITZ

**DEUTCHLAND
2017**

Online link: <http://nbn-resolving.de/urn:nbn:de:bsz:ch1-qucosa-230942>

Abstract

Compact helical antenna for smart implant applications

135 Pages, 52 Figures, 3 Tables, 395 References

Medical devices have made a big step forward in the past decades. One of the most noticeable medical events of the twentieth century was the development of long-lasting, wireless electronic implants such as identification tags, pacemakers and neuronal stimulators. These devices were only made possible after the development of small scale radio frequency electronics. Small radio electronic circuits provided a way to operate in both transmission and reception mode allowing an implant to communicate with an external world from inside a living organism. Bidirectional communication is a vital feature that has been increasingly implemented in similar systems to continuously record biological parameters, to remotely configure the implant, or to wirelessly stimulate internal organs. Further miniaturisation of implantable devices to make the operation of the device more comfortable for the patient requires rethinking of the whole radio system concept making it both power efficient and of high performance. Nowadays, high data throughput, large bandwidth, and long term operation requires new radio systems to operate at UHF (ultra-high frequency) bands as this is the most suitable for implantable applications. For instance, the MICS (Medical Implant Communication System) band was introduced for the communication with implantable devices. However, this band could only enable communication at low data rates. This was acceptable for the transmission of telemetry data such as heart beat rate, respiratory and temperature with sub Mbps rates. Novel developments such as neuronal and prosthetic implants require significantly higher data rates more than 10 Mbps that can be achieved with large bandwidth communicating systems operating at higher frequencies in a GHz range. Higher operating frequency would also resolve a strong issue of MICS devices, namely the scale of implants defined by dimensions of antennas used at this band. Operation at 2.4 GHz ISM band was recognized to be the most adequate as it has a moderate absorption in the human body providing a compromise between an antenna/implant scale and a total power efficiency of the communicating system.

This thesis addresses a key challenge of implantable radio communicating systems namely an efficient and small scale antenna design which allows a high yield fabrication in a microelectronic fashion. It was demonstrated that a helical antenna design allows the designer to precisely tune the operating frequency, input impedance, and bandwidth by changing the geometry of a self-assembled 3D structure defined by an initial 2D planar layout. Novel stimuli responsive materials were synthesized, and the rolled-up technology was explored for fabrication of 5.5-mm-long helical antenna arrays operating in ISM bands at 5.8 and 2.4 GHz. Characterization and various applications of the fabricated antennas are successfully demonstrated in the thesis.

Keywords: Helical antenna, rolled-up polymeric tubes, strain-engineering, injectable antenna, specific absorption ratio, S-parameters, self-assembly, polymeric platform, bridging element, finite element methods.

Table of Contents

Abstract	iii
List of acronyms	1
1 Introduction	3
1.1 Motivation	6
1.2 Objectives	9
1.3 The thesis structure.....	10
2 Background	11
2.1 Wireless medical implantable devices	11
2.1.1 Telemetry and drug delivery.....	13
2.1.2 Bioelectrical interfaces.....	15
2.2 Implantable wireless communication systems.....	18
2.2.1 Types of communicating systems.....	18
2.2.2 Electromagnetic radiation in a biological environment.....	20
2.2.3 Designs of implantable antennas	24
2.3 Rolled-up self-assembling technology.....	29
3 Fabrication and characterization methods	33
3.1 Thin film technology	33
3.1.1 Photolithography.....	33
3.1.2 E-beam deposition.....	35
3.1.3 Sputter deposition	37
3.1.4 Chemical deposition.....	38
3.2 Characterization methods	40
3.2.1 Profilometry.....	40
3.2.2 Vector network analyzer.....	41
3.2.3 Scanning electron microscopy and focused ion beam milling	42
4 Platform for self-assembled structures	45
4.1 The sacrificial layer.....	45
4.2 The hydrogel layer.....	46
4.3 The polyimide layer.....	48
4.4 The polyimide for bi-layer lift-off process.....	51
4.5 The frame solution.....	51
4.6 The encapsulation solution	52
5 Results and Discussion	55
5.1 Modelling of the compact helical antenna	55
5.1.1 Definition of parameters and 3D geometry of an electromagnetic environment	56
5.1.2 Helical antenna layout and optimization of geometrical parameters	56
5.1.3 Targeting in-vivo implant applications.....	61
5.1.4 Self-assembly of helical antennas from the planar state.....	65
5.2 Experimental realization of compact helical antenna.....	70
5.2.1 Substrate cleaning.....	70
5.2.2 Adhesion promotion of the glass surface.....	70
5.2.3 Patterning of the sacrificial layer.....	71

Table of content

5.2.4 Patterning of the hydrogel layer	71
5.2.5 Patterning of the polyimide layer	71
5.2.6 Structuring of metal electrodes	72
5.2.7 Self-assembly process.....	74
5.2.8 Encapsulation of antennas.....	76
5.3 Characterisation of compact helical antennas	79
5.3.1 Return loss.....	79
5.3.2 Transmission between two normal mode helical antennas.....	80
5.3.3 Implanted antenna	81
6 Conclusion and Outlook	85
6.1 Conclusion.....	85
6.2 Outlook.....	86
References	87
List of figures	115
List of tables	117
Selbständigkeitserklärung	119
Acknowledgements	121
Research achievements	123
List of publications	123
Cover page	125
Accepted patents.....	126
List of oral presentations.....	126
List of poster sessions.....	126
Theses	127
Curriculum-Vitae	129

List of acronyms

AA	Acrylic acid
Ar	Argon
ATP	Adenosine triphosphate
BaTiO₃	Barium Titanate
BCI	Brain-computer interface
Bis-GA	Bisphenol A-glycerolate (1 glycerol/phenol) diacrylate
BP	Benzophenone
BPDA	3,3',4,4'-Benzophenonetetracarboxylic dianhydride
BSE	Back scattered electrons
C	Circumference
DEGMEE	Diethylene glycol monoethyl ether
DETPA	Diethylenetriaminepentaacetic acid
DI	Deionized
DMAc	N,N-Dimethylacetamide
DMAEMA	Dimethylaminoethyl methacrylate
DRA	Dielectric resonator antenna
DUT	Device under the test
E-Beam	Electron beam
EDTA	Ethylene diamine tetra acetic acid
EMI	Electromagnetic interference
ESA	Electrically small antennas
FCC	Federal Communication Commission
FEM	Finite element methods
FIB	Focused ion beam
FL	Functional bilayer
GPS	Global positioning system
GSG	Ground signal ground
HCl	Hydro chloric acid
HDODA	1,6-hexandiol diacrylate
HEMA	N-(2-hydroxyethyl)methacrylate
HG	Hydrogel
IEEE	Institute of Electrical and Electronics Engineers
ISM	Industrial, Scientific and Medical
L	Length
La	Lanthanum

List of acronyms

LVDT	Linearly variable differential transformer
MDA	4,4'-Methylenedianiline
MDEA	Methyl diethanolamine
MICS	Medical Implant Communication Service
MSA	Micro strip antennas
NaOH	Sodium hydroxide
NEP	1-Ethyl-2-pyrrolidone
NMM	Negative index meta materials
OS	Operating system
PAA	Polyacrylic acid
PCB	Printed circuit boards
PEAMA	Poly(ethylene-alt-maleic anhydride)
PEGDA	Poly(ethylene glycol) diacrylate
PEMA	Poly(ethylene-alt-maleic anhydride)
PGMEA	Propylene glycol monomethyl ether acetate
PI	Polyimide
PIFA	Planar inverted-F antenna
PMDA	3,3',4,4'-Pyromellitic dianhydride
PoC	Point of care
PTFE	Polytetrafluoroethylene
RF	Radio frequency
RFID	Radio frequency identification
S11	Return loss
SAR	Specific absorption ratio
SE	Secondary electrons
SEM	Scanning electron microscope
SL	Sacrificial layer
TEA	Triethylamine
TMAH	Tetramethyl ammonium hydroxide
TMSPM	3-(trimethoxysilyl) propyl methacrylate
W	Width
Ω	Ohm

1 Introduction

Communication is a natural, inescapable feature of a civilization or any socially organized biological system. Such an organization is highly beneficial for biological systems to resolve higher order objectives and its implementation is feasible only by collectively behaving species and hardly affordable by a single organism. Survival, social interaction and intellectual development of a human would not probably happen without the communication. Mankind went a long way through centuries developing efficient ways of information delivery over short and long distances, using speech and writing, passing through the era of smoke and fire signaling (Figure 1.1b) towards postal services and even animals for faster communication (Figure 1.1b), telegraphy and modern means of ultra-fast communication.

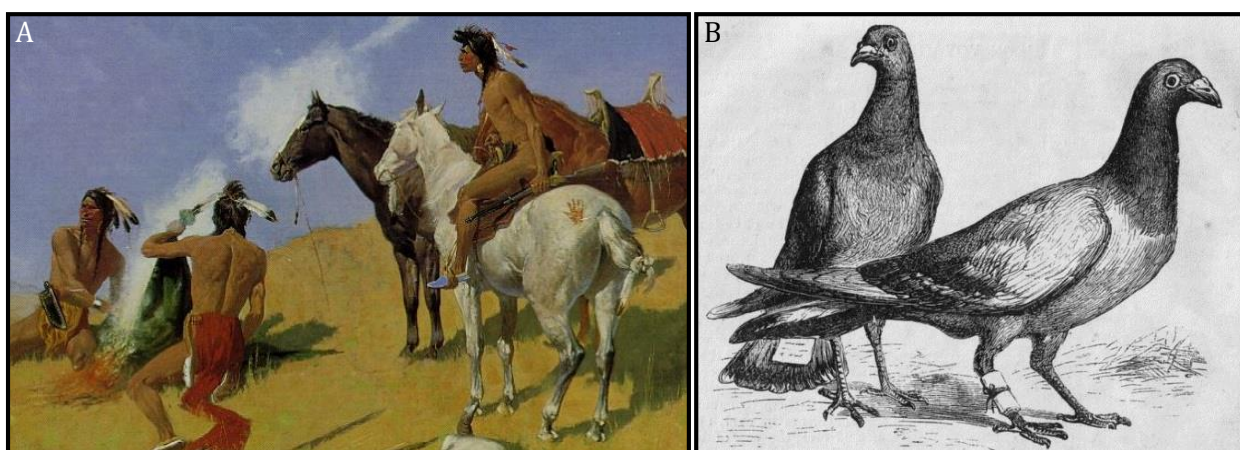


Figure 1.1: Information delivery over long distances in past times. A) Smoke signals generated by Native Americans.^[1] B) Post pigeons with attached message to the leg and the tail.^[2]

A global revolution occurred with the development of the electrical telegraph in its most accepted realization by S. Morse and A. Vail in 1837^[3] allowing the rapid wired communication between two distant points. The wired signal transmission allowed the stationary communication between socially important centers, cities, and countries speeding up the further development of economics, medicine, and industry. However, high costs, stationarity, and complexity in the organization of electrical telegraphy in unfavorable or inaccessible areas promoted further development over the following decades. The dream of communication without limiting mobility of smaller social groups and even single individuals has motivated many famous engineers and scientists to develop a wireless telegraph. Generation of electromagnetic radiation, initially predicted by J. C. Maxwell in 1865, was achieved in 1888 by H. R. Hertz in an electronic circuit demonstrating the feasibility of wireless transmission. The success of the Hertz's demonstration has promoted the realization of the first commercially accepted wireless telegraph developed by G. Marconi in 1894^[4,5] and its fast spreading around the world (Figure 1.2a).

1 Introduction

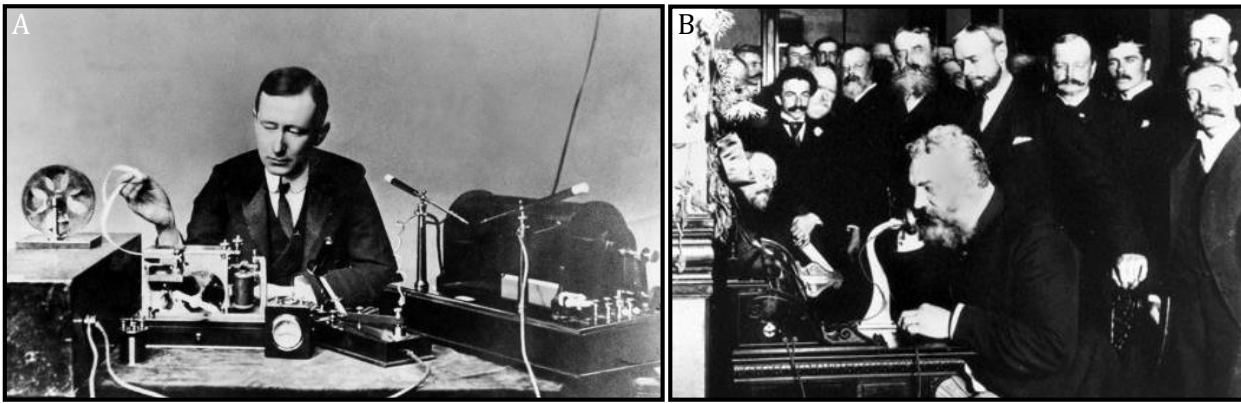


Figure 1.2: Long range communication. A) Guglielmo Marconi and his shortwave long range wireless telegraph transceiver. (Image source: Wikipedia) B) In 1915 A.G. Bell participated in the first transcontinental call from New York to San Francisco. (Image source: Virtual Museum: Telecommunications History Group)

The wireless communication has matured since that time, acquiring all the novel development in the telephone (Figure 1.2b) (invention of the first phone 1876^[6]) and network communication (appearing in 1960^[7]) to the level where we are not able to imagine our life without the variety of wireless networking devices used for broad band communication nowadays. Increasing tempo of the life forces the modern society to exchange information as rapid as possible and to develop new devices to meet those demands. The current progress in electronics development with great human imagination (Figure 1.3a) has provided to us mobile phones, laptops and a variety of smart devices that are combining countless functionalities in one system (Figure 1.3b). The development of the global positioning system (GPS)^[8], flight telemetry, radio frequency identification (RFID) tags^[9], low power Bluetooth[®]^[10], Wi-Fi[™]^[11], mobile, and global wireless networks^[12] follows the current trend of “wirelessification” together with its major benefits, including the simplification of everyday life, higher mobility, and an access to the global information networks.

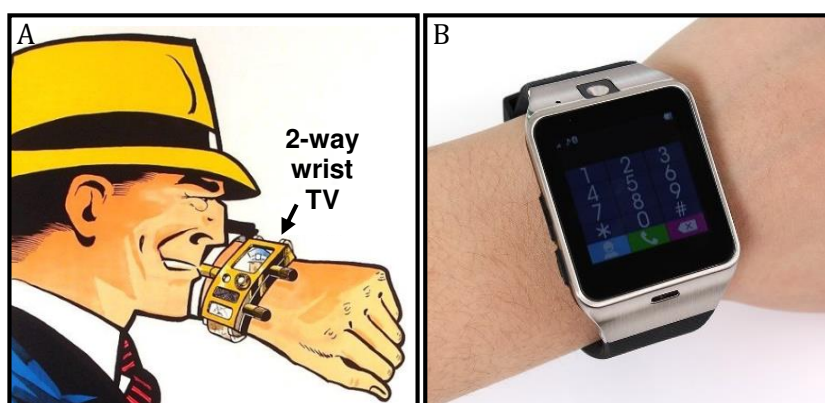


Figure 1.3: From imagination to reality. A) An artistic vision of a communication possibility with another person through a wearable wrist watch. (Image courtesy of Tribune Company Syndicate, Published in the comic strips in 1964) B) State-of-the-art wearable Smart Bluetooth Watch GV18. (Image courtesy of Aplus)

Modern electronic devices are so complex that the number of interconnects responsible for data transaction within a system has exponentially grown over last decades. These devices require wireless solutions for intra- and inter-chip communication as well as between modern electronic

devices e.g. computer and mobile systems.^[13-16] The increased complexity of final devices demands the fabrication of multilayered printed circuit boards (PCB) interconnecting multimedia chips. This aspect became more expensive than the functional components themselves due to the invested time and personnel, suggesting the “wirelessification” of integrated circuits to minimize wired interconnections just to power lines.

Miniaturization of active devices resulted in various diagnostic systems for applications in and on a human body to acquire medical data. When electronics became compact and more power efficient, a variety of novel applications were suggested for medicine i.e. active implants. One such device was developed in 1958 using solid state electronics to become the first cardiac implantable stimulator.^[17] Today's wide variety of these devices are developed to affect physiological parameters^[18-21] and stimulate biological tissue that cannot normally operate^[22-24]. Implants could recognize diseases through detection of biological markers,^[25-28] predict and localize seizures or correct paralysis and epilepsy with magneto encephalography systems.^[29,30] Support and activate the body's natural healing processes, improvement in the lifespan of individuals and their quality of life is performed by regenerative medicine using specially designed implants for regeneration promotion and monitoring of this process.^[31] Monitoring of damaged neuronal tissues during stem cells recreation process is one of the novel breakthroughs in regenerative medicine.^[32]

Electronic implantable devices can nowadays interact with the central and peripheral nervous system.^[33] Here, a set of chips could be implanted into the brain tissue^[34-39] or placed around it^[24,28,29,34,40,41], realizing the so called “brain-computer” interface (BCI)^[39,42-44] communicating with an external environment. The BCI system can decode signals from the brain or peripheral nervous system, adjusting their functionality^[45,46] and bypass areas with malfunctioning neurons^[45] or even imitate damaged parts^[47,48]. These systems play a central role in the development of artificial counterparts for legs, arms^[49,50], ears^[51], eyes^[52,53], speech^[54] and other organs. These systems, equipped with microprocessors and computer chips, can be directly controlled by signals from the central and peripheral nervous systems. The integration of artificial materials with biological tissues has drastically changed the shape and appearance of electronic devices over the past decades making them thinner, lighter, more bendable^[30,55,56], adaptive^[57], and even stretchable^[58,59]. Novel thin polymeric substrates^[55,59] that can withstand large mechanical loads and small bending radii allow confinement of an electronic device on an arbitrarily shaped surface, like the skin^[60-65], for consumer or medical applications. These systems, however, still require solutions for data transmission between the implantable device and an external acquisition or prosthetic system, which is realized today mostly through bulky cables due to the huge amount of transmitted data.^[37-39]

To create a better user experience, these medical applications should include wireless electronics that comply mechanically and electrically with the biological parameters, providing communication to transfer data among internal and external devices enhancing the mobility of patients as well as improving rapid diagnosis and disease prediction.

1.1 Motivation

New concepts of efficient designs for antenna need to be adjusted to novel requirements in implantable and ultrathin devices from conventional free space wireless transmitting systems. The fundamental working principle of any wireless communication system is matching the electromagnetic impedance of a transmission line to the impedance of free space by a functional element in order to efficiently generate electromagnetic radiation. In any wireless system this element is antenna or a set of antennas. Designing a miniature antenna for implantable or wearable medical applications remains an extremely challenging task due to a complex biological environment and fundamental physical limitations. An implantable antenna should satisfy several requirements i.e. small geometry (in mm range), matched impedance in a working frequency range with a low specific absorption ratio (SAR) in an attenuating biological environment, and high gain and maximum power efficiency. Despite severe constraints in the design, aiming on a maximum electrical performance, the antenna must also comply with the design and fabrication technology of final implantable system.

During the design of implantable data transmitting systems, several criteria should be considered, which includes maximum power consumption of the system, biocompatibility (mechanical, chemical and electromagnetic), and total weight and scale of the system. The typical dimension of state-of-the-art implantable and wearable devices is in the centimeter and millimeter range.^[19,26,51,66,67] Further downscaling of such systems requires miniaturization and a rethinking of antenna designs.^[68] However, an antenna miniaturization does not go hand-in-hand with the fundamental physical aspects of the antenna performance that are significantly affected at a certain scale.^[69] On one side, the small size of an antenna is desired due to the miniaturization trend of medical devices to make them minimally invasive. On the other side, the size reduction negatively affects the efficiency of a radio frequency (RF) system, especially operating at low frequencies, which led to the rise of operation frequencies in such systems. However, the upper frequency is limited by the absorption coefficient of the electromagnetic radiation in the biological tissue and the safety regulations.^[70,71] These regulations are simultaneously limiting the maximum applicable transmission power and operational frequency bands accepted by Federal Communication Commission (FCC). This commission has defined radiofrequencies for medical devices in UHF bands called Medical Implant Communication Service (MICS) and Industrial, Scientific and Medical (ISM) bands in the range of 402–405 MHz and 902–928 MHz, 2.4–2.483 GHz, 5.725–5.875 GHz respectively.^[70]

It is important to consider that any antenna operates efficiently together with a transmitter when the input impedance of an antenna is matched to the impedance of an RF transmission line of the transmitter, having one of the commonly applied values i.e. 50Ω as the best tradeoff between power

transfer and attenuation.^[72] These parameters are based on the fact that antennas are usually much smaller than the wavelength they radiate, reducing the radiation impedance of an antenna. An ideal spherical antenna of a size comparable to its radiating wavelength placed in vacuum would have a radiation impedance equivalent to that of the free space, which is defined as a free space ratio between electric and magnetic fields of a propagating wave $Z = \sqrt{\mu_0/\epsilon_0} = 377 \Omega$.^[73] Hence, a smaller antenna will always have a mismatch to the ideal radiation impedance.

A miniature antenna, namely a “small antenna” whose dimensions are much less than the wavelength of the radiation behaves conceptually as a dipole antenna with a coaxial “donut” like radiation pattern.^[74] To achieve a maximum power efficiency, small antennas are usually designed together with reactive matching networks, which are available in various forms.^[75] These networks are tuned for a particular frequency band to cancel the (resonant) reactive part of an antenna leaving only the active resistance of radiation and losses. Matching the antenna impedance to the transmitter’s impedance prevents the supplied energy from returning into the transmission line, which will dissipate in undesired electromagnetic radiation and heat. Together with the matching network, an antenna represents a resonator allowing a gradual radiation of the pumped energy with each oscillation cycle of the resonator. Thus, the design of the resonating antenna should account for the required input impedance and the highest possible quality factor at the required bandwidth to prevent severe power losses, even throughout various environmental conditions and influences of mechanical disturbances.^[74] The stability of the antenna parameters, regardless of geometric variations becomes especially critical in biological conditions. It is known that the soft biological tissue is prone to continuously change shape^[76-78] and the device applied within the biological environment should conform to these variations maintaining or intentionally shifting parameters in an optimal operational window.

Among all established antenna architectures, helical designs are particularly interesting for implantable applications. Due to the distributed impedance network, the antenna itself forms a matching network, hence efficiently utilizing its limited space.^[74,79] An appropriate design of a millimeter scale helical antenna could lead to self-matching with no external components required, providing geometrical stability against mechanical disturbances due to the antenna cylindrical shape. The size of a helical antenna could be 10 times smaller than the corresponding dipole antenna^[79] occupying less space. Meanwhile, efficiency of small antennas is determined by a volume of a sphere which could be fitted around an antenna.^[80-82] In other words, a small antenna in a wireless implant will have the best possible efficiency if it could enclose completely the surface of the implant. Here, helical antennas have a strong advantage, as they could conform to the outer surface of the implant without occupying the inner volume of the device, leaving some space for electronic circuitry, energy supply etc. The regular geometry of a helical antenna could be fitted onto the surface of a cone or a cylinder, naturally complying to most shapes of the developed electronic implants.^[26,29,32,83-86]

1 Introduction

Dimensions of these devices could be small, significantly simplifying its implantation process by e.g. injection using hypodermic needles with diameters from 300 μm up to 1 mm into the target tissue,^[86-90] minimizing discomfort and post-operational recovery time for the patient. The implants should be made of soft and chemically inert materials such as biocompatible polymers in order to reduce damages to organs and tissues and to provide stability over a long period of time.^[91-93]

Another strong advantage of the helical antenna design is its fabrication in an easy manner using just two flat conductors fabricated on a thin flexible substrate that can self-assemble into a tube forming a conducting helical structure.^[94-101] This is especially attractive as it allows for an easy variation of the antenna design and it opens a potential for fabrication of such types of antennas in planar microelectronic processing with a subsequent assembly into a helix. The semiconductor industry, known for its high yield and large-scale fabrication and the development of the technology and processes for helical antenna fabrication could potentially promote cheap and high yield manufacture of electronic devices for medical applications.

1.2 Objectives

This work focuses on the development of a technology that allows the fabrication of integrated self-assembled miniature normal mode helical antennas compatible with a standard process applied in the semiconductor industry. The antenna is to be designed in a way to operate in the ISM bands at 2.4 GHz and 5.8 GHz, as a good compromise between antenna size and acceptable attenuation level in the human body tissues for neuronal application.^[102,103] Antenna design has to be compact in size and have acceptable return loss less than -10 dB, provide a wide bandwidth to cover the ISM radio band.

The self-assembled helical antenna need to be compatible with the implantation process of a medical device using a standard medical syringe, for this task, its length must be less than 10 mm and the diameter is less than 1 mm. In this work the impedance of the antenna will be self-matched to 50 Ohms at desired bands, which is a commonly applied wave impedance of electronic circuits eliminating additional matching elements. Due to restrictions in safety regulations on the maximum transmitting power and the limited power available for implantable device, it is necessary to consider that the antenna should have a sufficient gain suitable for the transmission over at least a meter of distance. The biocompatibility of materials has to be taken into account in this work.

1.3 The thesis structure

Chapter 2 shows the historical evolution and current state of implantable and wireless medical devices for a patient's health care system. Wireless communication systems that are applied in implants are discussed. An overview of diverse antenna designs for wireless implants is given, comparing their performances. At the end of the chapter, an introduction into the technological platform for antenna fabrication is provided.

Chapter 3 describes processes and technological equipment used within this thesis for material deposition and lithographical patterning steps. In the second half of the chapter, characterization techniques are shown, determining material parameters and electrical characteristics of the prepared antennas.

Chapter 4 is devoted to the developed polymeric platform that allows the fabrication of self-assembled helical antennas using standard photolithographic processes. At the end of the chapter, encapsulation processes and materials are described allowing for passivation and frequency tuning of antenna structures.

Chapters 5 includes results of mechanical and electrical simulations of the self-assembly process behavior utilized in the fabrication of helical antennas. Mechanical simulations describe possible problems in the self-assembly process at an initial stage and provide solutions resolving those. A comparison with real structures is provided as well. Electrical simulations for a millimeter scale implantable helical antenna design operating in the ISM radio band reveals impedance matching to 50 Ohm. A technological route provided for the experimental realization of the simulated helical antenna and a comparison of experimental and simulated results are discussed.

2 Background

The chapter provides an overview on the current state of implantable medical devices, which are wireless in most applications. Such systems integrate a complex electronic circuit and antennas that enable data exchange between the device inside a body and a system. In the following subchapters will be given a brief historical background on wireless medical implants, described wireless communications and antenna designs suitable for in-vivo applications. Fabrication technologies will be discussed at the very end of the chapter.

2.1 Wireless medical implantable devices

In the beginning of the 1950's^[104], medicine made a big step towards treatment of heart with the first ever external “mains-powered portable pacemaker” (Figure 1.1a) consisting of implantable wire electrodes placed near a patient's heart. This design could eliminate discomfort and painful chest wall contractions in comparison to the previous version that was based on the on-skin electrodes.^[105,106] The device, however, could not completely avoid infections where the wires went into the body to the heart stimulating electrodes. At the same time, device was bulky, heavy and not really mobile due to the length of the power cord and use of vacuum tube based electronics to produce stimulation pulses for the heart. The invention of the first germanium transistor in Bell Labs by Bardeen and Brattain in the December 1947^[107] (Figure 1.1b) and introduction of the first commercially available silicon transistor by Texas Instruments in the 1954 (Figure 1.1c) opened a new era of compact electronic and microelectronic devices. Small size and a low power consumption of novel electronics resulted in rapid development of the first programmable, battery-operating wearable and portable cardiac pacemakers by Earl Bakken in 1957^[108] (Figure 1.1d). The chest protrusion by electrodes was eliminated in the 1958 by Dr. Ake Senning and Rune Elmqvist in the development of a completely implantable device^[17] (Figure 1.1e) which could operate for only a very short period of time. However, novel advanced power saving electric circuits were implemented in the first long-term implantable pacemaker in the 1960's by Wilson Greatbatch and William Chardack which could prolong the life time of an integrated battery, decreased the invasiveness of the implant and maintained its operation while reducing the risk of infections.

Further development led to the first cardiac pacemaker, which (Figure 1.1f) nowadays allows successful treatment of heart diseases like blockades and arrhythmia. This progress has demonstrated the great importance of devices that can operate within a human body solidifying the field of implantable biomedical devices. Since the 1960s, medicine has significantly progressed in the monitoring and treatment of diseases within the human body leading now to the global market of

2 Background

implantable medical devices, roughly reaching 400 billion dollars in 2015'th.^[109] These advances in medicine give possibility to use novel unconventional solutions in radio communication systems.



Figure 2.1: Evolution of implantable cardiac device. A) External portable pacemaker powered through extension cord.^[104] B) Modern replica of the world's first germanium contact point transistor. (Image courtesy of Alcatel-Lucent USA, Inc., Bells laboratory) C) The first commercially available transistor presented by Texas Instruments in front of the 3 cent postage mark. (Image courtesy of Texas Instruments Inc.) D) Programmable battery-operating wearable and portable cardiac pacemaker.^[110] E) Modern replica of the first completely implantable pacemaker. (Image courtesy of Wikipedia) F) State of the art of the MRI compatible implantable pacemaker. (Image courtesy of Sorin group)

New innovations in wireless implantable technologies attract a lot of world-wide attention in areas of early detection, healing, and prevention of diseases. This offers an improvement in a quality of life and patient safety by avoiding delayed appointments at hospitals or periodic visits to a doctor. At the same time providing an immediate monitoring of physiological parameters and analysing of an abnormal behaviour of biological processes in an organism.

Using such systems, patients could observe their own health using miniature, cost-effective, and smart physiological sensors. These multifunctional devices implanted inside the human body could display the relevant measurements on screen of a user's smartphone (Figure 2.2a) or transmit the data regularly to a point of care system (PoC), from where collected information will be delivered to

a medical center (Figure 2.2b).^[111–114] A receiver placed in the vicinity e.g. inside the patient's home or directly in a personal electronic appliance, like a smartphone or a wrist band, would provide immediate feedback to the user or a healthcare provider. Whether the patients are in the hospital, at home or on the move, they will no longer be restricted to a bed while being monitored and may move around freely. Currently there are several wireless implantable devices operating worldwide which will be described in the following sub chapters.

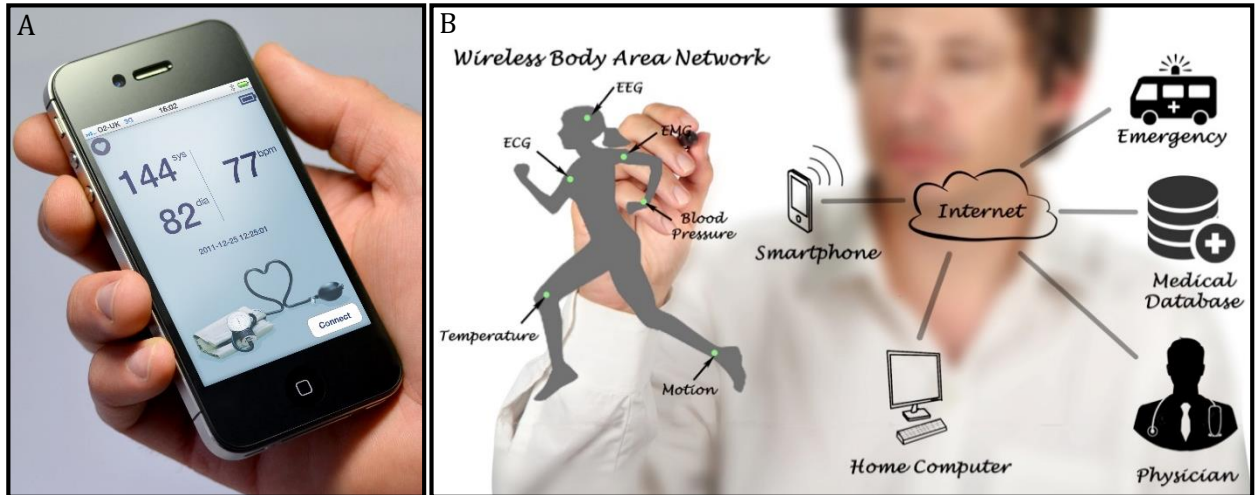


Figure 2.2: Conceptual view on the medical care system. A) Smartphone equipped with biomedical acquisition software collecting different vital signs of the human health. (Cambridge Consultants, Apple mHealth a blood pressure monitor) B) Schematic representation of the wireless medical data acquisition system. (IMATIS MyHealth+)

2.1.1 Telemetry and drug delivery

The wound healing process requires constant monitoring to recognize symptoms of an infection and how they change with time. Important parameters of interest that could be presented in a wound and measured by injectable wireless implants are a value of bacteriological infection (Figure 2.3a),^[25] level of pH and oxygen in the surrounding tissue.^[115] Additionally, measurement of lactate level is required (Figure 2.3b),^[116,117] which works as a signal accompanied to the tissue oxygen starvation associated with an internal bleeding and anaerobic processes.^[118] For instance, due to a strong anoxia, tissue cells die release adenosine triphosphate (ATP) molecules into the surrounding environment. The concentration of these molecules could be measured locally by an implanted inductive wireless biosensor array.^[117] For recording of biological data, these systems usually operate at 5 MHz using a coil as an antenna with transmission distance of up to 17 mm^[117] to a base PoC which uses a transmitter operating in 405 Mhz MICS range^[116]. In some cases measurement of lactate level could not be enough, because its concentration is also associated with the level of an abnormal glucose concentration in the blood stream and surrounding tissue requiring additional sensory capabilities resulting in increased data rates.^[118]

2 Background

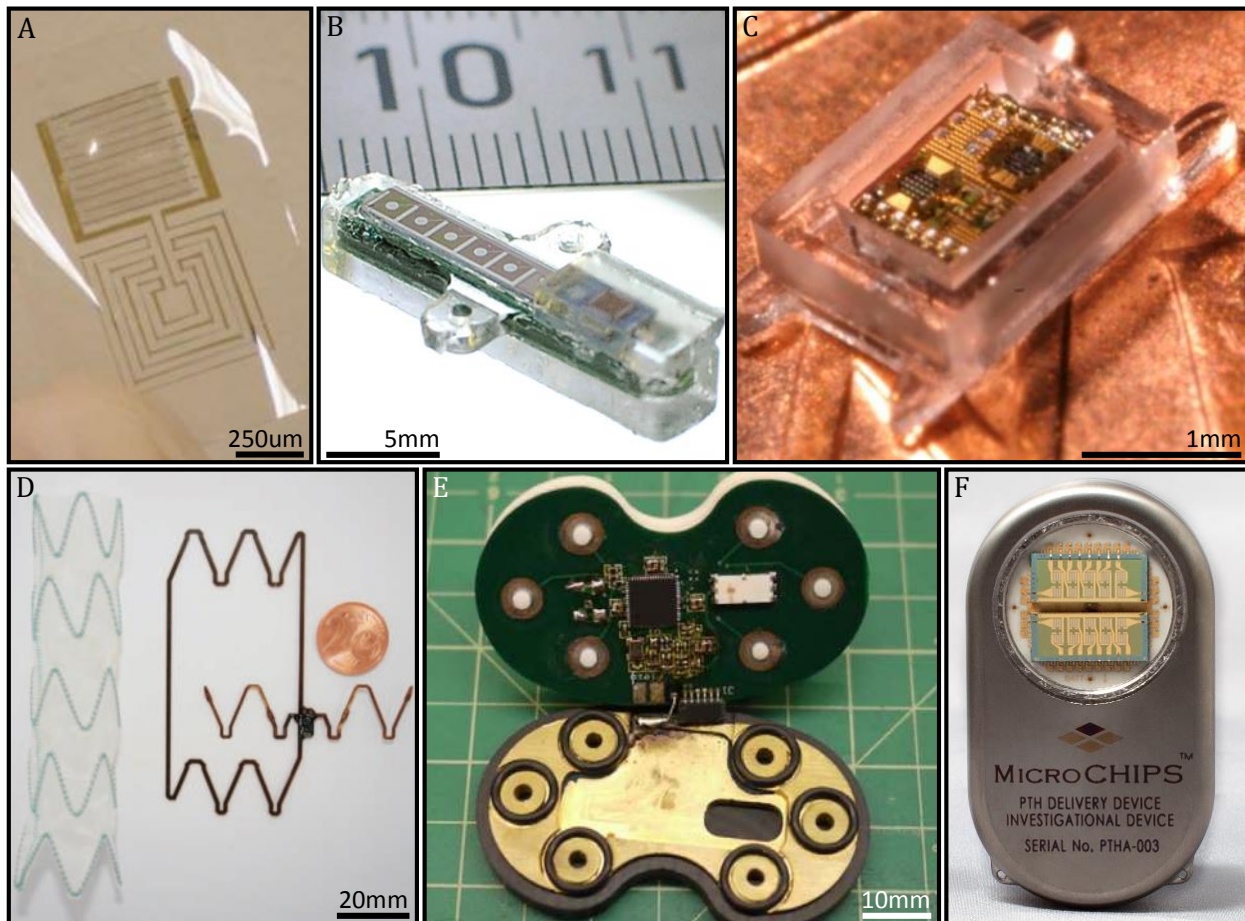


Figure 2.3: Implantable sensors and drug delivery systems. A) Passive wireless bacteriological telemetry system. 250 μm scale.^[25] B) An implantable biosensor array for personalized therapy applications.^[117] C) Intraocular wireless pressure sensor for glaucoma prediction.^[119] D) Endovascular stent (left), the pressure sensing implant (right).^[120] E) Implantable pressure sensor for knee implant.^[121] F) Microchip-based wirelessly controllable drug delivery device. Dimensions of the device are 5 \times 3 \times 1 cm. (Photo courtesy of MicroCHIPS Inc.)

Hyperglycemia and glucose intolerance is observed for more than 600 million people struggling with diabetes type one and two world-wide^[122]. Currently, tracking and treatment of these diseases is one of the major programs in medicine resulted in appearance of a completely implanted wireless enzymatic glucose sensor.^[117] Further development led to a successful integration of a replicable wireless drug delivery and glucose sensor into the tooth implant with its long term application.^[123] In this device, all collected information was sent via a Bluetooth 4.0 interface at 2.4 GHz using a conventional ceramic chip antenna. Different levels of glucose can influence on the dielectric constant of the blood, variation of which could shift resonance peak of a coupled RLC circuit^[68] or an implanted patch antenna.^[124] All enzymatic reactions could fluctuate with variation of environment parameters. To counteract the environmental changes, implants could be equipped with pH^[117] and temperature^[117,125] sensors. When the sensor is no longer required or approaches end-of-the-life it could be biodegraded inside the body, thus avoiding an extraction procedure.^[68]

As an accompanied measurement to chemical parameters, data on aspiration^[126] and heart rate^[58,126] could be acquired wirelessly as well. Some disease associated with an abnormal pressure could be

diagnosed by implantable devices that detects blood pressure,^[125,127] pressure in a brain cavity,^[66,128] pressure in an eye for glaucoma prediction^[119,129,130] (Figure 2.3c) or as a tool for post-surgical evaluation of an aneurysm (Figure 2.3d).^[120,131,132] These implants can communicate with external receivers up to 10 cm away via 133kHz^[125], 13.5 MHz^[66,120,128] and 35 MHz^[132] inductive link or 570 MHz^[119] and 2.4 GHz^[130] radio link. There are a number of recently implanted artificial disks and joints contain telemetry sensors that could be placed in a patient's spine^[133], hip^[134,135] or knee^[121,136-139] (Figure 2.3e) and could be used for non-invasive wireless monitoring of applied forces, pressures, strains, and a local temperature. Regular acquisition of such an information could eliminate unpredictable failures or trauma. In these implants, information is transmitted either via near-field inductive coupling operating at 4 kHz^[134,138] and 13.5 MHz^[137] or via 80 MHz^[140] and 900 MHz^[121,136] radio connection up to several meters. Based on collected physiological data, an implant may deliver a drug (Figure 2.3f),^[19,141-144] monitor the local drug level within a body^[117] and its consumption according to a prescription by a physician.^[145,146] In these implants, transmission is realised through inductive link at 2 MHz^[19], 170 MHz^[141], radio link at 433 MHz^[143,144] and via natural body conductivity with a wearable wireless adapter^[145,146]. A drugless treatment of a tumour could also be performed electrochemically by decomposition of a body fluid into oxygen and hydrogen with ultrasonically powered injectable implantable device.^[21] The same implant could be provided an impedance analysis capability obtaining information about chemical or physical conditions of a tissue^[147] by measuring i.e. rejection of neuronal electrodes^[148-151], response to an external excitation^[152] or damage levels^[27].

2.1.2 Bioelectrical interfaces

In comparison with pharmacotherapy, electrical or neuro-stimulation was found to produce fewer adverse effects^[153]. Additionally, neuronal stimulation by an implant applying low-frequency pulses could block propagation of excessive neurological signals and either partially or completely recover functions of an organ or relieve pain. Neuronal stimulation by implantable devices can treat chronic pain and disorders attributed to spinal cord^[40,154-157], peripheral nerve^[24], or brain^[158], including cluster headache by stimulation of sphenopalatine ganglion with an implantable wireless device^[23,159,160] or a deep brain stimulation to treat Parkinson's disease, tremor, and dystonia.^[22,161] Restoration of an organ's functionality is another important task for implantable devices. Cochlear^[51] and retinal implants^[52,53,162,163] respectively recover hearing and sight that has been lost due to failure in receptor cells. Usually these implants are implanted under the skin due to big size of a controller unit while an electrode connected via a cable is placed near a stimulation area. Communication with the implant is realised via inductive link for periodic maintenance^[22,24,40,154-158,161] or on the constant base together with a power transfer.^[51-53,162,163]

2 Background

Oppositely to stimulation, neuronal recoding^[28,41,126,164,165] works as a “brain-computer” interface^[166] and could be used as a restoration tool for neurofunctional disorders. For this purpose a variety of special implants developed to treat damaged areas, working as artificial neurological circuits^[48] or bridging elements^[45]. Several of such neuronal recording systems were commercialized up to now including “BrainGate interface”^[37,167,168], “Plexon Multichannel Acquisition Processor”^[169–175], “Hermes”^[176–178], and “BioBolt”^[179,180]. These setups consist of two main blocks: recording elements and transmitting system. Recording side can be based on a variety of electrodes e.g. needle type electrodes inserted directly into the cortex of a brain (Figure 2.4a),^[28,34–36,181] one^[40,46,159,182,183] or two^[24,88,180,184,185] dimensional electrodes placed near a recording area (Figure 2.4b) or cuff type^[26,32,83–85,93,186–188] that are wrapped around a nerve(Figure 2.4c).

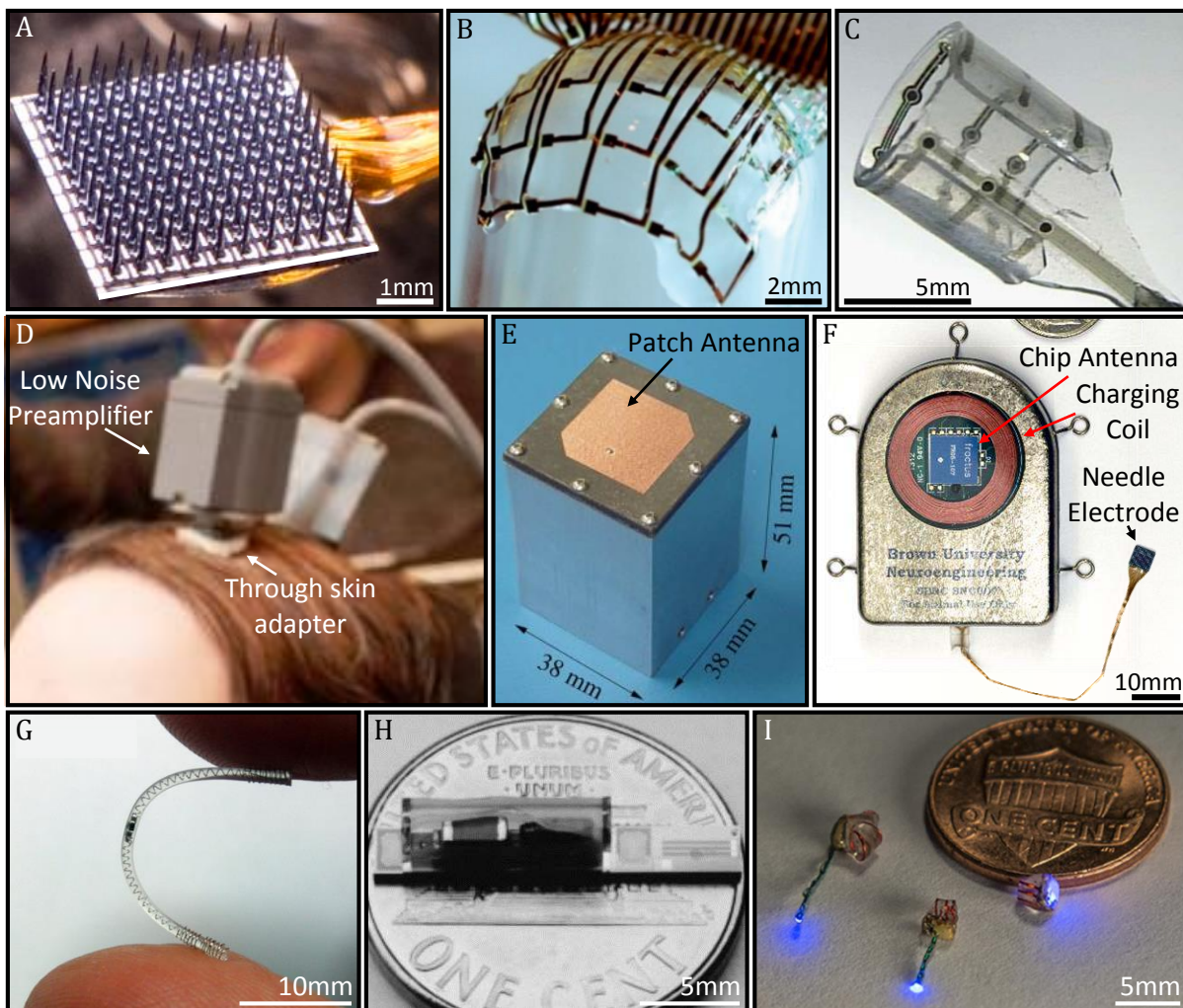


Figure 2.4: Different types of neurological devices. A) Needle type electrode array. (Image courtesy of Brown University) B) Ultra-thin conformal ECoG electrode array.^[185] C) Cylindrical cuff type electrode array.^[187] D) A wired interface for the interaction with a mind controlled robotic arm.^[37] E) HermesD a wireless system for recording neurological signals.^[176] F) Chronic wireless implantable device for neuro-sensing applications.^[165] G) Injectable micro stimulator based on charge-balanced rectification currents applied to epidermis.^[183] H) Single channel injectable wireless neuromuscular device.^[189] I) Wirelessly powered injectable optogenetic stimulating device.^[190]

Signals, accepted via electrodes, are carried out through cables to a skull or a skin adapter (Figure 2.4d). Most of current neuronal data acquisition systems use a through-skin percutaneous connector due to its simplicity, but it is harmful and have high risk of infection. Usually in modern systems, the adapter is also equipped with a low noise preamplifier and includes an external (Figure 2.4e) or fully implantable (Figure 2.4f) radio transmitter for communication with a processing unit.^[165,168,176,180,191-193] To restore lost functions, neuronal data could be acquired and processed, after that wirelessly applied to a distant implant for stimulation required nerve^[67] or directly to a peripheral organ^[194,195]. Also, this method include possibility to apply processed signal to a syringe-injected wireless muscular implant for stimulation limb motion^[86-90,183,196,197]. If some functions were lost completely, the collected signal could be processed and converted in to a signal to be sent to a motorized chair^[198,199], a telepresence robot^[43], a mechanical prosthesis^[42,200,201], or even to a speech synthesis system^[54]. For powering and signal transmission tasks are mainly used inductive coupling due to size limitation of these type of implants and non-availability of compact energy sources.^[89,90,197] For powering implanted device with some limitation could be used conductive properties of the body^[183], ultrasonic waves^[84] and radio waves^[196]. Today, a major part of implantable devices for research purposes use wired connections due to simplicity, but this solution limits the mobility of the subject.^[37] Even state-of-the-art long range wireless systems, which came to replace wires and overcome associated restrictions, are still too bulky (Figure 2.4e, f) and require complex surgical procedure for an implantation process. In this case, implantation through injection via hypodermic needle (Figure 2.4g-i) looks like a promising operation that minimizes injury to surrounding tissue and minimizes post operation recovering time.^[86,89,90]

A successful and widespread application of bioelectric interfaces will be promoted by small, implantable devices that use minimally invasive implantation methods to eliminate long-term protrusions through skin. The scale of wireless implantable devices is defined to a large extent by a battery and an antenna. The size of batteries could be still minimised by the development of new energy sources and efficient low power electronics, while dimensions of antennas are determined by fundamental physical constrains, which have to be considered in novel designs of implantable devices to reduce an overall scale. For instance a straight forward way would be to increase a working frequency of the system operating in medical bands at moderate power levels complying with electromagnetic requirements for low SAR.^[202,203] Ideally the output power of the transmitter should be as small as possible due to a strict limitations on available on-board energy storage thus requiring an efficient antenna design. The critical parameter in the antenna is impedance, which should comply to standard impedances of radio transmission lines.^[72] And size of the radio system could dramatically increase when matching is performed with electric components assembled around the antenna.^[130] Advantages and limitations of various wireless communication system and state-of-the-art antenna designs applied in implantable devices will be described in the following section.

2.2 Implantable wireless communication systems

The development of radiofrequency equipment and wireless technologies has recently made a breakthrough in implantable systems reducing its invasiveness and eliminating through skin and through skull adapters. Despite this progress, communication between compact implanted devices and existing healthcare monitoring systems using wireless interfaces to transfer information over several meters is a strong challenge for researchers and engineers nowadays. In this chapter, an overview of different types of wireless communication systems will be given with a focus on current challenges associate with an introduction of wireless technologies in a human body and state-of-the-art solutions for antenna designs applied within implantable systems.

2.2.1 *Types of communicating systems*

In the beginning of the implant wireless communication era, an inductive link was utilized due to its simplicity, low power consumption, and small attenuation of magnetic field in a biological media.^[204] For an inductive link a couple of mutually inductive coils are used as an antenna on both sides of an implanted and external transceiver device. Magnetic coupling is required between two coils for proper operation and due to a fast decay in magnitude of the magnetic field with a distance between two coils, the transmitter and the receiver are located at a short distance from each other. Communication distance could be determined from dimensions of coils and usually is proportional to their sizes.^[205] The dimension of an implanted coil is determined from an implant scale considerations which is usually ranging from cm's to mm's, thus limiting the communication distance. Usually the transmitter coil is placed as close as possible even in a direct contact with the patient's body for proper operation of the inductive link. From the other side, due to standardized carrier frequency and its location around 128 kHz,^[70,206] this communication limits data transfer to very slow rates requiring a prolonged transmission time. Due to mistakes in the transferred data or misalignment of coils, the data transfer process must be repeated this is could be unsuitable for medical devices. To overcome this issue, higher working frequencies (2 MHz^[19], 5 MHz^[117], 13 MHz^[66,120,128,137,147], 88 MHz^[140] and 170 MHz^[141]) were applied allowing addressing of multiple implantable devices and moderate data transfer rates. Alternatively, other types of communication systems were developed using optical^[181,207] and ultrasonic^[84] channels as well as utilizing conductive properties of a human body to perform an electrical connection to an implant^[145,146,208]. Despite the low power consumption and high data rates, such systems require precise alignment of an implant and an external transmission device, frequently keeping last one in contact with a human body.

At the end of 20th century, the FCC and Institute of Electrical and Electronics Engineers (IEEE) has introduced a MICS and an ISM radio bands allowing a license free distant operation of medical devices

and implants.^[70,206] This event opened doors for engineers developing new RF microelectronic technologies for medical devices. Operation at UHF frequencies simultaneously reduce both power consumption and scale while improving sensitivity of radio receivers. In comparison to inductive coupling, communication over far-field electromagnetic waves have several distinct advantages including longer distance between implant and transceiver, higher data rates resulted in lesser energy consumption, and no needs in precise alignment between units.

The FCC has selected the MICS radio frequency band due to low attenuation coefficient of RF signal in a human body. However, a complex biological environment generates novel challenges for RF antenna designers rendered in a non-uniform distribution of dielectric constant and conductivity of different tissues and cavities, and non-even geometries strongly affecting antenna performance. Usually, wavelength is much larger than applied antenna designs; therefore, electrically “small antennas” have substantially reduced power transmission efficiency. Together with restrictions on transmitting power applied in MICS band,^[206] this reduces maximum communication range to ~2m.^[209] Additionally, due to a low bandwidth per channel of 100 kHz to 300 kHz allocated by the standard, the communication system permits only low data rates. MICS radio band was not standardized world-wide and is suitable mainly for receiving small amount of telemetry data from implanted or connected to the body sensors,^[209] while neurological applications as BMI systems require a wireless transmission of a huge amount of data in real-time.^[176,193] Thus, researchers world-wide started to pay attention at the ISM radio band as a vantage point in the developments of implantable neural devices, where operation at higher working carrier frequencies at the allocated radio band could provide a wider bandwidth,^[210] as a result enhancing bit rates of the system.^[211]

The ISM band has higher-frequency ranges allocated around 915 MHz, 2.45 GHz and 5.8 GHz, has higher bandwidth, provides data rates more than 10 Mbit/s, lowers power consumption due to small duty cycle of an operating time, and, finally, is a worldwide standard. This radio band can be used without limits on the range and strict regulations only limiting radiation power to the maximum level of 10 dBm while not exceeding maximum SAR level in surrounding biological tissues.^[70,212] At the same time, higher frequencies are beneficial for small antennas as the wavelength approaches the size of the antenna. This allows much lower power consumption due to the higher efficiency.

There are however, a drawback of open RF band. Operation of many electronics such as household devices like microwave ovens and network communication systems were considered as a potential risk of electromagnetic interference (EMI) that could disturb operation of medical devices. It was demonstrated that only a very close proximity between the implant and RF source operating at the same channel may cause malfunction of the transmission link. However, system could operate with 100% of success by changing the working channel.^[113] Development of medical implants operating in these frequency bands is highly supported by the fast rise of mobile devices in the last decade, providing cheap and high quality RF components that are applied within implantable systems. The

2 Background

future of implantable devices lie in high frequency MICS/ISM and ultra-wide bands, where the current development towards fully wireless medical electronics is expecting to fulfill the niche in the next decade.^[213] The starting point for this development is a new efficient antenna design operating at defined distances between transmitter and receiver in a defined location of a biological environment at required frequency range, while using available bandwidth and power.

2.2.2 Electromagnetic radiation in a biological environment

In comparison to the free space, electromagnetic waves propagating in biological environment affected by a material with a high dielectric constant and conductivity dependent on wavelength of radio waves. Any biological body, such as a human or an animal, represents such an environment with a complex non evenly distributed dielectric constant, which strongly influences resonant conditions of a small antenna and level of absorption in the radio channel it uses.^[102,214] These conditions depend to a large extent on both the position and orientation of the implanted antenna within the body, and the dielectric parameters of the biological environment. Wave propagation in the dielectric environment can be characterized by parameters such as attenuation constant - α , phase constant - β and wavelength in the media - λ . These relations of the wave and medium parameters are given as:^[215]

$$\alpha = \frac{\omega}{c} \sqrt{\frac{\epsilon'}{2}} \sqrt{\sqrt{1 + \tan^2 \delta} - 1} (Np/m)$$

$$\beta = \frac{\omega}{c} \sqrt{\frac{\epsilon'}{2}} \sqrt{\sqrt{1 + \tan^2 \delta} + 1} (rad/m)$$

$$\lambda = \frac{\lambda_0}{\sqrt{\epsilon'/2} \sqrt{\sqrt{1 + \tan^2 \delta} + 1}} (m)$$

where $\tan \delta = (\omega\epsilon'' + \sigma) / \omega\epsilon'$ is the loss tangent of the material, $\omega = 2\pi f$ - angular frequency, ϵ' and ϵ'' are real and imaginary parts of relative permittivity of the material, σ is the conductivity (S/m) of the media and c is speed of light in vacuum.

It is known, that human body consist of almost 60% of water and 0.9 % w/w of dissolved salts, which are responsible for the distribution in dielectric constants and conductivity within the body due to concentration variation in different tissues. According to international regulation of FCC and IEEE for wireless medical applications, 402-405 MHz MICS, 902-928 MHz, 2400-2483.5 MHz and 5725-5850 MHz ISM frequency band ranges could be used for wireless implant applications.^[206] As it could be seen from the Figure 2.5, the dielectric constant of a pure saline solution has a relatively small distribution at the given bands and at human body temperature ($\sim 36.6^\circ C$) dropping from 74 to 68 with increase in frequency, but in a real biological tissue like muscles it has smaller value

ranging from 57.1 to 48.5.^[216,217] However, the dielectric losses in the media has stronger effect at lower frequencies due to ionic conductivity,^[218–220] which vanishes when frequency of the electromagnetic radiation became higher than oscillating relaxation time of ions.^[219,221] In those conditions, higher frequencies are preferred over lower frequencies to reduce dielectric losses in the material.^[218] Attenuation constant is used to derive an important parameter, namely penetration depth of the wave in a lossy media. At the penetration depth, the wave amplitude reduces to 1/e or 37% of its initial value.

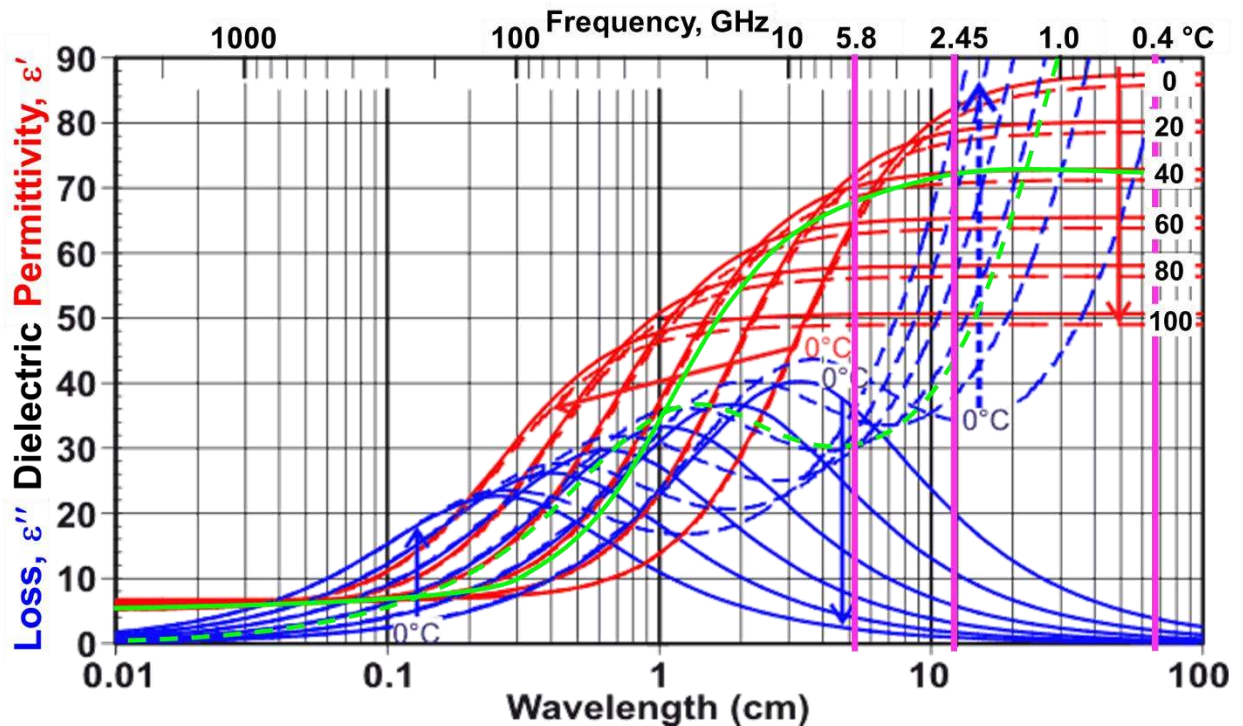


Figure 2.5: Dielectric constant and losses of water as a function of frequency. Red and blue solid lines represent parameters for clean water, dashed lines show the behavior of salt water. Green lines mark parameters of water at human temperature, where solid and dashed lines represent relative permittivity and losses, respectively. The data is indicative only. Violet mark frequencies are used in medical applications (ISM and MICS radio bands). (Image adopted from M. Chaplin, "Water and Microwaves". Water Structure and Science)

It is important to consider that for the standard frequencies of 402 MHz, 915 MHz, 2.45 GHz and 5.8 GHz, the wavelength in muscle tissue has value of 95 mm, 43 mm, 17 mm, and 7 mm with a penetration depth of 53 mm, 42 mm, 22 mm, and 7.5 mm respectively.^[216] In fatty tissue, the penetration depth for particularly 2.45 GHz could be as high as 100 mm. In comparison to 402 MHz MICS band and 915 MHz ISM band, the 2.45 GHz and 5.8 GHz ISM bands has a relatively small penetration depth. However, for an application in neuronal implants, with an average nerve dislocation depth in a human body between 5 mm and 80 mm for wrist and hip respectively, with an averaged value of 20 mm or less at joint positions or at spine area,^[103,222–225] it is realistic to consider 2.45 GHz and 5.8 GHz bands as good candidates for this direction in the medicine. Additionally, neuronal recording requires high data rates, which would benefit from higher operating frequencies.

2 Background

Using for instance the 2.45 GHz band, a successful application of a wirelessly powered stent implant operating deeply in a human body was already reported.^[226]

However, dielectric losses in biological and medical applications of wireless devices requires a strict control of dissipating power in the tissue, which can heat up the environment and could harm or damage the tissue if critical temperatures are exceeded.^[70] As a result, the dissipating power of communicating systems is strictly regulated for ISM and MICS bands and defined as a maximum specific absorption ratio (SAR). The SAR for general public exposure is defined by the standards for given frequency ranges.^[70,71] For instance, for frequencies between 100 kHz and 3 GHz, the SAR is limited to 0.08 W/kg for the whole-body, while for arms and legs distal from elbows and knees should not exceed 4 W/kg and for other tissues in a human body is limited to 2 W/kg. It should be also taken into account that at lower frequencies i.e. 402 MHz and 915 MHz, quarter of the wavelength could coincide with dimensions of body tissues, resulting in wave resonances and as a consequence enhancement of SAR.^[71]

Higher operating frequencies result in a smaller antenna with a lower occupied volume, which has benefits for small-scale implants attached to i.e. nerve. Moreover, a small antenna that operates at higher frequencies has better radiation efficiency in comparison to an antenna having similar scale and operating at lower frequencies, due to the ratio between antenna dimensions and the wavelength.^[227] From this considerations, it could be expected that even a half-wave-length antenna designed for operation within a human body at 402 MHz MICS band will have a large scale (47.5 mm's). If an antenna designed for 402 MHz band would have dimensions of the same type antenna operating at 2.4 GHz or 5.8 GHz ISM bands, it would have a much higher SAR level in the biological tissues due to its lower power radiation efficiency.^[203,228-230] Basically, for a fixed operating frequency, SAR will increase for smaller antennas.^[231]

Almost all antennas used in within implantable devices belong to the category of ESA due to their small size in comparison to the wavelength.^[79] An antenna is assumed to be ESA when it satisfies ratio $ka \leq 0.5$, where $k = 2\pi/\lambda$ - the free space wavenumber and a - the radius of a sphere enclosing the occupied volume by the antenna.^[232] The ESA description is usually applied for free space antennas and may not be used for an implanted antenna surrounded by a biological tissue that strongly influences the wavelength. If the antenna is implanted deeper than its near field - the region close to an antenna where electric and magnetic fields are still not perpendicular to each other and still don't propagate in a phase, it will interact with free space over a human body representing a bulk and non-uniform dielectric media. In such an environment the antenna can be physically small but electrically comparable to the wavelength.^[216]

Due to the strong influence of the surrounding environment, the antenna scale usually also includes a surrounding ground plane and interacting objects within their geometries.^[74] In many cases, regular

antennas operating normally outside the organism cannot operate within the body or acquire a significant shift in their resonant frequency due to this additional environmental parameters, which are not presented otherwise (Figure 2.6a).^[233,234] It was demonstrated that resonance shift experiences fast saturation with increase in dielectric permittivity (Figure 2.6b).^[235] As well, different antenna locations, complexity, and shape of a phantom used for simulations could strongly affect the performance of an antenna communicating with an external device.^[102] To obtain an appropriate design of an implantable antenna and to calculate the operating parameters, it is necessary to use complex models which take into account all necessary body parts that may potentially work as components of a distributed electromagnetic circuit operating as a so-called dielectric resonator antenna (DRA), possible dielectric lens configurations, or scattering sites.^[102,214,236] An important parameter, which is considered for such a situation, is the total antenna gain outside the body, which is applied for calculation of path losses for EM waves and helps in estimation of wireless system limits.^[203]

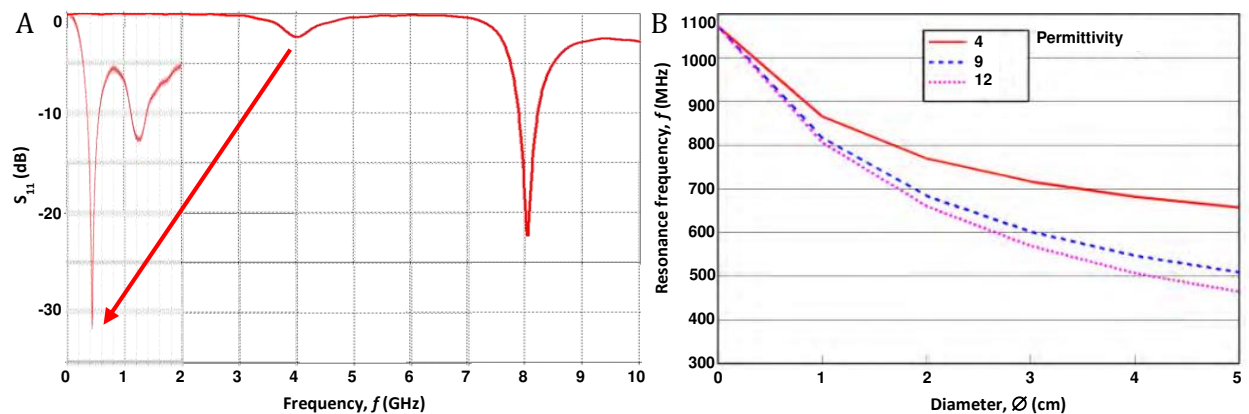


Figure 2.6: Resonance shift in a dielectric material. A) Shift of the resonance frequency in the human body. (Image is adopted from [233]) B) Dependence of operating frequency on dielectric permittivity. (Image is adopted from [235])

Despite the scale reduction of an antenna due to a human body dielectric properties, the antenna size can be further miniaturized by applying general rules developed by Wheeler, Chu, Harrington, Best, Fante, and others for small antennas.^[232] These rules tell us that below a specific scale, the radiation resistance of an antenna drops while reactance increases. At this point one should always keep in mind that the radiation impedance of a space is purely active (resistive) and defined as the ratio between electric and magnetic field propagating in the space (for free space is equivalent to $\sim 377 \Omega$). If antenna cannot match free space impedance (basically cannot transfer energy to the radiation load in one period of oscillation usually due to its small scale), the energy supplied by a transmitter will be reflected from the antenna-space interface and will be either returned to the transmitter or stored in a near field of the antenna with a gradual radiation over many oscillations through the small ($< 377 \Omega$) radiation load. This ratio between stored and radiated energy represents the radiation quality factor of the antenna and for smaller radiation resistances this value increases.^[237] However, matching of the active wave-impedance of an antenna to the space impedance is one side of the challenge, the small antenna should also transform the free space impedance to transmitter line,

2 Background

which usually requires external matching elements or additional design considerations for the antenna itself.^[74,79,238]

The last condition can be promoted in a resonance circuit, where energy is stored in a reactive, distributed LC network and near field of an antenna. As the efficiency of a small antenna highly relies on how many oscillation cycles should be performed through the active radiation resistance before the stored energy could be fully emitted, the antenna with higher Q factor resonance circuit would have a higher efficiency. However increase in Q factor of an antenna itself also means a strong interaction of the stored energy in the near field with an environment of the antenna which leads to an increase in dielectric losses associated with the material like biological tissue surrounding the antenna and higher SAR level.^[203] The bottle neck of small antennas is their bandwidth which is inversely proportional to quality factor of the resonant antenna. There are, however, several strategies to increase bandwidth of an antenna by applying higher working frequencies or introducing matching elements or very complex multi-resonance designs of the antenna shape. However, applying matching elements is usually joined with an increase in scale of the systems and additional losses, which could be significant in comparison to radiation losses of the antenna itself making it less efficient.

The main conclusion is that the most efficient broadband small antenna design should utilize available volume within implanted device applying less number of external matching elements. This has resulted in a broad variety of different antenna designs for implantable devices that utilize various strategies for miniaturization of antennas.

2.2.3 *Designs of implantable antennas*

Different types of small implantable antennas were developed for MICS, ISM, and UWB radio bands utilizing a standard dipole or patch type antenna structures. Due to their mechanical flexibility, planar and low-profile antenna designs are very abundant in literature (Table 1). Practically, these are dipole^[239-241], loop^[242,243], slot^[244,245], micro strip antennas (MSA)^[246-252] and patch antennas^[253-256]. Usually, implantable patch antennas are used with a shortening pin to the ground plane^[203,214,228,251,257-264] and calls as a planar inverted-F antenna (PIFA), these antennas are also heavily utilized in mobile communication nowadays. Popularity of the PIFA type antennas could be understood by application of a short pin, which defines the antenna input impedance reducing the number of matching elements and associated with them losses. Top path element of the PIFA could have different shapes: loop^[233,262,265], meander line^[203,229,258,261,266-268], spiral^[248,249,251,265,267,269-273] (Figure 2.7a) or with stacked elements^[251,261,274] if multi-band applications are required (Figure 2.7b). Other so called self-matched antenna types include 3D spiral antennas (Figure 2.7c)^[270,271,273,275,276]. These consist of serially connected monopoles and loops representing a simplified shape of 3D helix.

By balancing these inductances and capacitances, one can reach a pure resistive behaviour which is achieved at the resonance frequency. The shape of such a helix is close to the most efficient 3D folded single arm helical antenna (Figure 2.7d) made by Wheeler which occupy maximum possible volume of a sphere surrounding it.^[79] All implantable antennas are usually protected by dielectric material isolating metal parts from the conducting biological environment and preventing their corrosion, as well as for biocompatibility purposes.^[129,277–279] Additionally, antennas with a strong power density in the near field are surrounded by a dielectric material in order to decouple fields from the biological environment thus minimizing SAR level and reducing non-radiative losses; however, the size of the antenna will increase.^[243,251,279] In general, a power saving strategy plays a crucial role for implantable systems. In a normal state, the implant is kept in “sleep mode” and the “wake up” procedure for the implanted device is made with an externally transmitted signal at another frequency band requiring antennas operating in at least two bands.^[228,259,260,271]

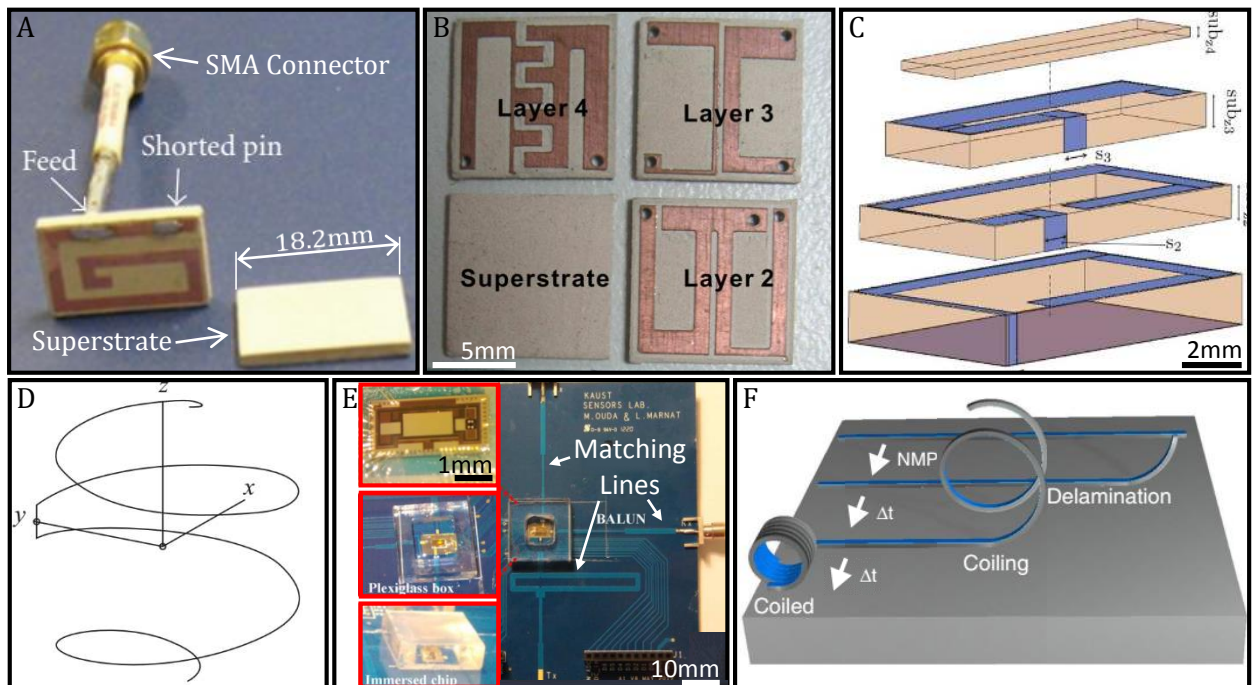


Figure 2.7: Realization of physically and electrically small antennas. *A) Spiral PIFA antenna for the 402 MHz frequency range.^[272] B) Triple band stacked PIFA antenna for MICS and ISM implantable devices.^[274] C) Stacked 3D spiral antenna for MICS and ISM radio bands.^[271] D) One-arm folded spherical dipole helical antenna.^[79] E) Impedance matching PCB board. The insets present on chip implantable loop antennas for 2.4 GHz and 5.2 GHz frequency bands.^[280] F) Schematic representation of a self-assembling planar stripe into a 3D magnetic micro helix.^[281]*

Negative index meta materials (NMM) has also been used as an impedance matching shell surrounding an antenna.^[282–284] These materials are working basically as a phase compensating elements in the near field pushing this region closer to the optimal radiation sphere outside the antenna volume thus effectively utilizing the given volume. However, due to resonance nature of the NMM, fabricated antennas will experience a poor efficiency in the lossy biological media.^[285–287] Some of those antennas are developed in a micro-stripe design.^[247,262]

2 Background

Despite the big dielectric constant of a biological environment, implantable antennas designed for 402 MHz MICS or 915 MHz ISM radio bands are still too large. Making even smaller antennas operating in these frequency bands increases level of SAR and lowers transmitting power as it could be seen from Kiorti's works.^[261,288] In this respect antennas operating at higher frequencies have distinct advantages, even if volume of such an antenna will be kept constant.^[227] The data presented in Table 2 lists antennas that operate at single ISM 2.45 GHz radio band, where it could be noted that high frequency antennas has smaller dimensions compared to MICS antennas in general. Furthermore, wire-type antennas occupy less volume than other types, at the same time have high gain. Comparing antennas for MICS and ISM antennas (Table 1 and Table 2), it could be seen that the smallest antenna can be designed using wire-type groundless designs with a wire folded in a loop^[280,289] or presented as dipole antennas in different shapes like spirals^[240,290] or helixes^[291-296]. Groundless antennas could have very small volumes e.g. self-assembled micro cubic^[297,298] or on chip loop^[280] antennas, but only in the case when transmitter impedance is not necessarily a standard 50 Ω . Otherwise they have very high own resonance frequencies^[298] or require matching circuits that are significantly larger than the antenna disregarding thus advantages of the very small form factor (Figure 2.7e).^[280]

Wired designs could play an important role in a strict volume defined conditions, where antennas could be displaced on the surface of an implantable device leaving a useful internal volume. This volume can be explored by electronics or energy source inside an implantable device or left empty, thus making complete system as compact as possible. As a trend nowadays, conformal shapes of such antennas attracting more attention.^[233,252,299,300] Here we need to take into account that it is common for many tissues within a human body to have a cylindrical shape such as blood vesicles, nerves, lymphatic system, or tendons. The round cross sections of these structures are actively exploited in cuff type implantable devices.^[26,83-85,186] Most designs of antennas initially made for free space and then dimensions scaled down for applications in implantable devices compensating shift in resonance frequency. Usually this downscaling approaches half wavelength in a human body leaving still a room for further miniaturisation.^[295] However, the small physical dimensions of antennas would require very complex fabrication procedures limiting their applications. In this respect, a dipolar normal mode helical antenna is the best trade-off among others wired antennas^[74,79] including size, wire length, performance at 50 Ω , and shape conformation to cylindrically shaped implants i.e. cuff and injectable implants. The helical type antenna by its nature made by winding of the conductor onto a cylinder or tube. This, three dimensionally complex process could be, however, performed with a high precision and high yield applying strain engineered rolled-up technology. In this respect a two dimensional planar structure could easily form a helix with a conductor on its shape (Figure 2.7f).^[96-98,101,281,301-305]

2.2 Implantable wireless communication systems

Table 1. Various antennas reported in the literature for MICS, ISM and WiBAN applications. Note: Volume is defined as a maximum extension of antenna functional parts e.g. dielectric case or metal parts. Frequency band is defined at a main resonance with a return loss (S11) better than -10 dB. Transmitting power is defined as an amount per mass (symbol 1 gram and 10 gram) satisfying maximum SAR level in a tissue. Symbol “n/a” means that this information was not provided in the literature.

Ref.	Antenna Shape	Volume [mm ³]	Frequency Band [MHz]	Implantation Tissue	Implantation Depth [mm]	Transmission Distance [m]	Transmitting Power [mW]	Gain [dBi]
[165]	UWB Chip	10x10x1 100	3.5G (600)	Under skin	n/a	1 (50 mW)	n/a	n/a
[228]	PIFA differential	$\pi \times 5^2 \times 25.2$ 1978.2	403(211) 2.45G(590)	Under skin	3	0.3	23.4 ¹⁰ 25.7 ¹⁰	-30.5 -22.2
[233]	U-Loop	$\pi \times 5^2 \times 15$ 1177.5	404.5(200 k)	Muscle	60	2	3.2 ¹	-28.9
[236]	Microstrip monopole	12x12x0.8 115.2	3-10.6 G	Head	0.5-30	10 mm	4.5 ¹	-15,-30
[239]	Water Monopole	$\pi \times 8^2 \times 30.5$ 6129.28	3.2G(2.62G)	Ingestible	n/a	n/a	6.5 ¹	-33.3 -43.6
[240]	Folded Dipole	27x5 h=10 um	825	Brain Surface	n/a	10 cm	n/a	-20.5
[242]	Coil	0.22 mm ²	433 915	Aqueous Humor	0.5	10 cm (47 mW)	n/a	n/a
[243]	Coupled Loop	7x7x5 245	403.5(8)	Muscle	20	n/a	10 ¹	-14.7
[244]	T-slot	10x10x1.6 160	6G(1.8G)	Canola Oil	5	1	n/a	-31.6
[251]	PIFA Stacked	13x12x4.06 630.24	403.5(5)	Vitreous Humor	n/a	6	44.4 ¹⁰	-40.3
[252]	Meander Conformed	$\pi \times 5^2 \times 18$ 1413	402(40)	Small Intestine	n/a	n/a	3.83 ¹ 23.35 ¹⁰	-29.6
[253]	Classic PIFA	39x30x3 3510	403.5(5)	Muscle	15	6 (0.55 nW)	n/a	-35
[254]	Patch	5.68x6x0.254 8.66	31.5G	Fat	8	1 (16 mW)	16 ¹⁰	-46.5
[256]	Patch	25x30x1.5 1125	7G(10G)	Human arm	2.4	n/a	n/a	-7.095
[259]	Split ring Slot PIFA	14x14x1.28 250.88	403.5(5) 2.44G (42)	Skin	~2.5-5	-	n/a	-40 -22
[260]	Microstrip	26x8x1.25 260	403.5(47) 2.41G (120)	Muscle	15	n/a	n/a	n/a n/a
[261]	PIFA stacked	$\pi \times 6^2 \times 1.9$ 214.78	402(43)	Under Rat skin	5	n/a	4.927 ¹ 30.73 ¹⁰	-30
[271]	Spiral stacked	$\frac{\pi}{2} \times 5.2^2 \times 24.7$ 1048.58	403.5(5) 2.45G(100)	Under skin	5	14 5	5.5 ¹ n/a	-28.8 -18.5
[276]	3D-spiral	14x14x15 2940	405(225.2)	Muscle	31	n/a	7.4 ¹	-28.5
[288]	PIFA stacked	$\pi \times 3.6^2 \times 0.7$ 28.48	412(50)	Inside Skin	0.25	15 cm	2.164 ¹ 25.9 ¹⁰	-50.98
[290]	Spiral dipole	5.2x5.2x1.5 40.56	1.41G(20)	Intraocular	n/a	25 mm	n/a	n/a
[241]	Dipole Folded	20.3x0.8x0.8 12.992	953(260)	Under Skin	2	10(25 uW)	n/a	-34
[294]	Dipole Helical	$\pi \times 0.7^2 \times 25$ 38.465	924(13)	Under skin	2	10(25 uW)	0.5 W ¹ 0.5 W ¹⁰	-35
[295]	Helical	$\pi \times 1.5^2 \times 3$ 23.31	886.5(7)	Ingestible	n/a	5 cm	11 ¹ 36 ¹⁰	-27
[296]	Dipole Helical	$\pi \times 0.8^2 \times 36$ 72.34	924(225)	Under skin	2	10	n/a	-20

2 Background

Table 2. Various antennas reported in the literature for ISM 2.45 GHz radio band.

Ref.	Antenna Shape	Volume [mm ³]	Frequency Band [GHz]	Implantation Tissue	Implantation Depth [mm]	Transmission Distance [m]	Transmitting Power [mW]	Gain [dBi]
[245]	Cavity Slot	1.6x2.8x4 17.92	2.45(85M)	Under Skin	4	4(12.5 uW)	2.5 ¹	-22.3
[255]	Patch	10x10x1.27 127	2.45(190M)	Under Skin	4	10	7.51 ¹ 75.2 ¹⁰	-20.4
[263]	PIFA	π 5 ² x1.18 92.63	2.45(142M)	Under Skin	n/a	10	4 ¹	-24.8
[264]	PIFA	10x10x1.27 127	2.49(350M)	Muscle	5	n/a	6.28 ¹	-22.33
[289]	Loop	3x4x1.6 19.2	2.32(500M)	Under Skin&Fat	2&3	1(10 uW)	n/a	-17.5
[280]	On chip Loop	2.88x1.07 1.4mm ²	2.4 5.2	Aqueous Humor	5mm	10cm	n/a	-29 -14.5
[292]	Dipole Helical	π 0.5 ² x14.7 11.53	2.45(51M)	Under Skin	2	10(25 uW)	n/a	-22.3
[293]	Dipole Helical	π 0.5 ² x17.7 13.89	2.45(77M)	Under Skin	2	20(25 uW)	n/a	-14

2.3 Rolled-up self-assembling technology

Bimetallic stripe bending behavior, when heat is applied, has been known since 1759. John Harrison introduced such a stripe in the marine chronometer to compensate thermal misbalance of the chronometer spring.^[306] Bending of the bimetallic stripe occurs due to the difference in thermal expansion of two joint films with an associated stress in the stripe. In the similar way, a planar thin-film structures with the introduced stress could create a 3D geometry during the stress relaxation process. For instance, the stress may occur at the interface between two epitaxially grown thin-films because of the lattice mismatch.^[301,307] Significant forces at the interface or in the volume of films can be induced if the right combination of materials and processes are used giving desired curvature of the film. Depending on the relaxation patch, various 3D geometries could be created, including wrinkles^[95], spirals^[308] and tubes^[95,96]. The mechanical assembly of planar structures into 3D shaped geometries has been extended over time from mono-crystalline epitaxially grown semiconductor layers^[301,307] up to a variety of polycrystalline semiconductor^[94–96,301,302,307], metal^[308–311] and amorphous oxide layers^[303,312–314]. The mechanical behavior can be calculated using known physical parameters of materials and their processing conditions.^[95,315]

Figure 2.8a presents a simplified schematic of the rolled-up technology. At first, a functional bilayer (FL) deposited on top of a sacrificial layer (SL) under an incidence angle of 60° between the substrate plane and evaporation direction achieving thin films in the range of ~50 nm. The purpose of such a deposition is to form a shadow by one edge of a photoresist structure (Figure 2.8a) giving an entrance opening for a solvent or an etchant. This is a starting point for the self-assembly process. The opposite side of the structure is anchored to the substrate. Left and right (in case of a rectangular pattern of SL) edges are also coated by the very thin bilayer stack partially preventing access of the solvent and assembly in a wrong direction. Then the SL is selectively destroyed during the process leaving the top layer unaffected. The process of the SL etching releases the FL from the surface allowing the stressed bilayer to be reshaped due to the stress relaxation. Conventionally, etching process performed in a liquid solution e.g. solvents or acids, which has several implications on the subsequent processes. To dry 3D structures assembled from nanometer thick layers and prevent their collapse due to the liquid surface tension, it is necessary to remove the liquid solvent by converting it into a gas without crossing the liquid gas phase. This can be achieved by i.e. replacing the solvent with liquid CO₂ and evaporating it at a critical thermodynamic point at high pressure and elevated temperature.

Despite the challenging fabrication process, arrays of small-scale structures (Ø20 µm) fabricated on small substrates (1x1 cm²) demonstrate a high fabrication yield (Figure 2.8b), which is important for mass production of micro scale devices e.g. self-propelling motors^[316], capacitors^[317,318] and batteries^[319,320] for energy storages, magnetic sensors^[29,311], optical cavity resonators for information

2 Background

processing^[321], for biological investigations such as cancer cell growth^[322–325] or neural stem cell differentiation^[321]. However, many efforts were devoted into development of fabrication processes that allow larger geometries in millimeter scale that are characteristic for 2.4 GHz antennas. Unfortunately, no successful rout was found using thin-film oxide layers for large-scale structures, where rolling process appeared mostly in random directions (Figure 2.8c).

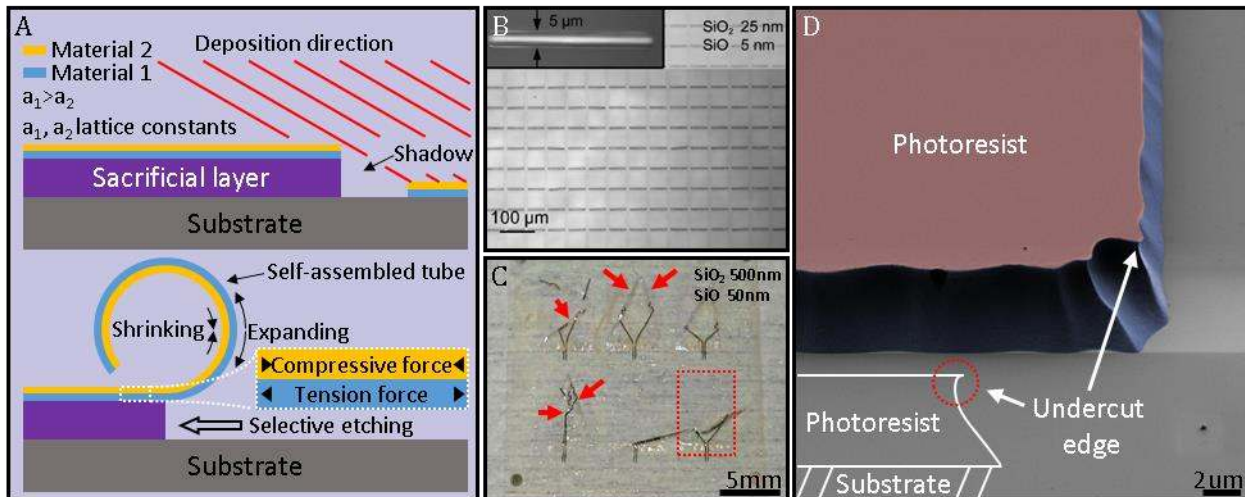


Figure 2.8: Rolled-up technology. *A) Schematic representation of strain engineering for production of self-assembled tubular structures.^[301] B) Array of uniformly self-assembled oxide micro tubes.^[303] C) Defective rolling of macro tubular structures. Dashed rectangle presents the initial area of the planar structure. Arrows indicate defective rolling directions. D) Scanning electron microscope (SEM) image of the photoresist layer containing undercut edge.*

Strong variations and failures in the assembly process could be understood in a close look on the edge of a regularly patterned photoresist structure (Figure 2.8d). As it could be seen from the Figure 2.8d, the imperfections of the photoresist edge has a scale comparable to the film thickness; additionally, the formed notch on the surface of the photoresist forms another stress point in thin-films. The characteristic shape of the photoresist edge is suitable for small-scale structures,^[94] but however could not be used for larger structures (5x8 mm). The stress on the edge became even more noticeable with the larger film thickness promoting formation of cracks and brittleness of an entire structure, which leads to a low yield of assemblies and integrity failures. Considering that the fabrication of the bilayer stack and an assembly of tubular structures is not the last step in the device fabrication requiring further lithographic steps, the technology should be altered to give an almost 100% yield and reproducibility of large-scale structures.

It is known that polymers and their composites with inorganic materials could provide a much better control over mechanical performance such as stability and conformation. For instance metal-polymer^[281,326], oxide-polymer^[101] or polymer-polymer^[97–99,304,305] bilayers are capable for self-assembling into a variety of 3D geometries including rolled-up tubes^[100,327,328], micro grippers^[329,330], cubes^[298], soft^[97,99,305] and rigid^[331–333] origami structures meanwhile being robust and stable. In comparison with oxide tubes, dimensions of self-assembled hybrid polymeric structures

could easily span the range from micrometers up to centimeters (Figure 2.9a-c). Unfortunately, we need to exclude technologies involving metal layers due to their screening effect for antenna applications and brittle oxide layers, which could reduce yield of working devices.

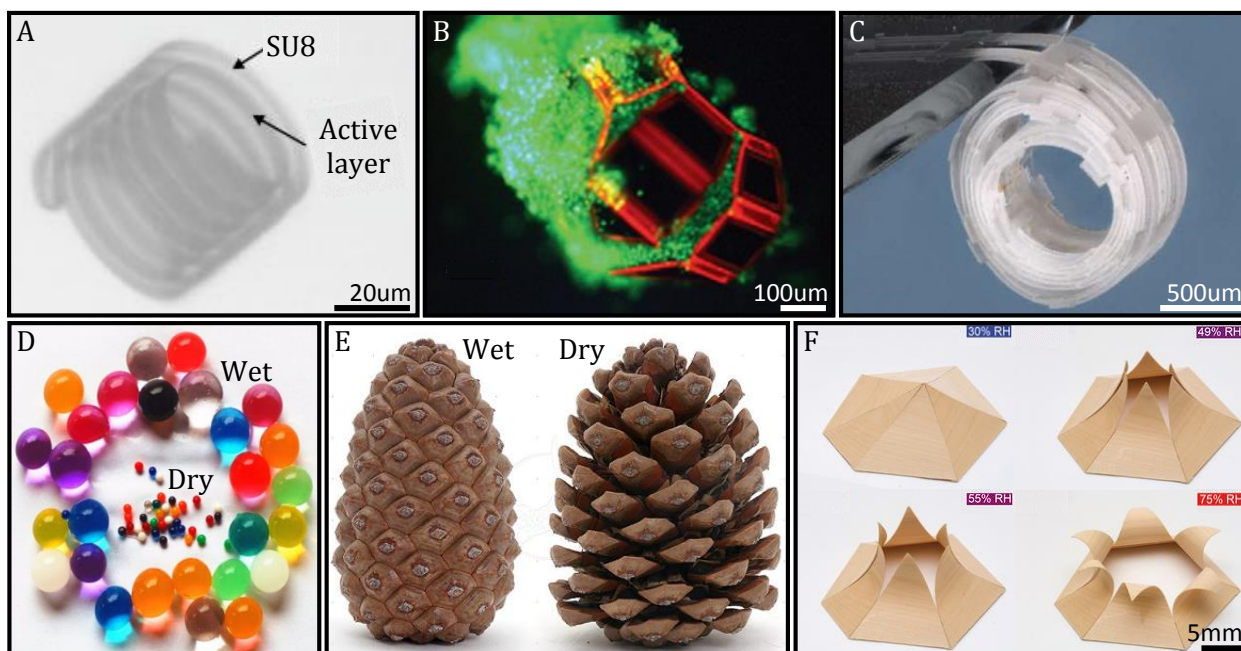


Figure 2.9: Stimuli responsive structures. *A) Optical image of a hybrid coil with SU8/magnetic layers.^[281] B) Fluorescent cells captured by a polymeric micro gripper.^[330] C) A 3.5-cm long-multilayer microfluidic device containing a single channel.^[334] D) Hydrogel balls before and after water uptake. (Image source <http://Selfedge.pk>) E) Pinecone in the wet and dry state. (Image source <http://biology.stackexchange.com>) F) Application of the pinecone effect in bio-inspired actuators. (Image courtesy of A. Menges, HygroSkin – Meteorosensitive Pavilion. FRAC Centre Orleans, France)*

Application of polymeric composites has a distinct advantage defined by a freedom in chemical modification of polymers, which can deterministically affect their mechanical, physical and chemical properties. An important mechanical parameter that can be affected in polymeric composites is stress. Several strategies could be used to induce stress in polymeric composite e.g. temperature variation^[57,305,335,336], pH response^[98,336,337] or swelling in solvents^[101,327,334]. For instance it is known that hydrogel can swell in water changing their volume more than 100% (Figure 2.9d).^[338] Induced volumetric expansion may produce an enormous mechanical force on the microscale that can be used in combination with a reinforcing layer to alter a shape of initial structure.^[32,339] This effect is heavily utilized in nature^[340,341] (Figure 2.9e) and was applied already in artificial systems (Figure 2.9f).^[98,305,336,337,342] However, applied materials are not suitable for harsh photolithographic processes that should be applied on top of these structures.

During research on available polymeric platforms all their advantages and disadvantages were considered to fulfill main requirements. One of the most important is a multi-lithographic processing with high yield of assembled structures. For this work, several polymeric materials were synthesized providing required performance. Polyimide (PI) and poly(ethylene-alt-maleic anhydride) (PEAMA) were selected as the functional inert material and pH responsive hydrogel (HG) respectively. PEAMA

2 Background

comes in already polymerized form with anhydride groups on back bones, which are chemically active and could be easily modified using alcohol monomers equipped with different functional groups.^[343] PI is one of the well-known polymers that is successfully utilized in electronic industry due to its stability especially in harsh environment applications.^[343] Application of polyimide could solve many issues associated with stability (chemical, thermal and physical), photo-patternability and protection of bottom layers. Unfortunately, compositions of all commercially available spincoatable and photopatternable polyimides are closed and confidential information of those companies, therefore, polyimides for this work were specially synthesized and modified for better adhesion among layers.

SL should have a good adhesion to the substrate and to top lying layers otherwise exfoliation will occur randomly. Meanwhile SL should be destructible at the assembly point not affecting top lying layers and be photopatternable. In industrial and scientific applications, a variety of sacrificial material for self-assembling and micromachining process have been introduced including semiconductors^[94,302,332,344], metals^[334,345], photoresists^[308,311], water soluble polymers^[346] or their metal ion crosslinked forms^[347,348]. In some cases, FL's could be physically bonded to the substrate,^[97,98,304,327,337] but this introduce problems during multi lithographic process steps decreasing yield of the working structures. However, among listened sacrificial layers there are no ideal one, which would satisfy all the requirements. The closest concept to the ideal SL was suggested by V. Linder applying a crosslinking mechanism of a water-soluble polymer with metallic ions.^[347] In this report, the most stable and robust layer was formed by the crosslinking of polyacrylic acid (PAA) with ions of Ca²⁺. Application of a chelating agent as ethylene diamine tetra acetic acid (EDTA) can remove Ca ions at pH 8 and uncrosslink SL to water soluble state. At the same time, at these pH values, SL behaves as a regular hydrogel such as polyacrylic acid or polyacrylamide and swells to a large extent requiring better stability at these pH values to perform self-assembly process. Replacement of calcium with lanthanum ions having higher coordination number improves stability of the SL with respect to pH levels^[349] and allow a direct photolithographic structuring of these layers. For crosslinking of SL, HG and PI layers acrylic functional monomers were selected. Acrylic groups are known for their non-complicated processability^[350]. They can be polymerized under h- and i-line UV light and provide covalent bonding between layers. In the following chapters, more detailed materials syntheses and technological steps for preparation of polymers and structures will be provided.

3 Fabrication and characterization methods

This chapter provides description of the technology and processes involved in the thesis that applied for fabrication of micro-scale helical antennas. Sample preparation includes a chemical synthesis of polymeric materials, their photolithographic definition on rigid supports using optical methods combined with a thin-film technology to introduce electrically conductive patches of antennas. The fabrication finalizes in a precise self-assembly step forming three-dimensional antenna structures, which followed by a characterization using high frequency probing methods.

3.1 Thin film technology

Sample preparation involves a variety of photolithographic processes, different types of coating methods, chemical processes that were mainly used for fabrication and application of polymers, vacuum deposition techniques that involves sputtering or electron beam evaporation of materials. These techniques were chosen as they represent the global standard microelectronics fabrication technology compatible with integrated circuit fabrication methods. This should allow a potential up scaling and high yield manufacturing. Development of samples, technological processes and characterization were carried out at the facilities of the Institute for Integrative Nanosciences (IFW Dresden, Germany).

3.1.1 Photolithography

Photolithography is one of the main and most complex processes involved in the manufacturing of state of the art micro- and nano-integrated electric circuits applied on an industrial scale, which could reach as high as 30% of time in overall production. Here, a common sequence of processing steps used in photolithography will be shortly described, which includes preparation of substrates, application and patterning of photopolymers or photoresists with a subsequent post processing.

Sample preparation starts with a cleaning step. This step involves a chemo-mechanical cleaning process of substrates that eliminates dust and organic contaminations. As the result, uniformity and adhesion of applicable materials could be substantially improved in comparison to untreated samples. Additionally, the surface of the substrate could be modified with special adhesion promoting agents to adjust the interface between the substrate and applicable materials (i.e. photoresist), simultaneously protecting the surface from contamination and absorption of water.

Usually photoresists and other polymeric materials could be applied on the surface using different methods including deep coating, doctor blade system, spin coating or dried polymeric film lamination

3 Fabrication and characterization methods

processes. However, the strict requirements on quality, thickness control and reproducibility of parameters applied in integrated circuit fabrication technologies has acquired spin coating as a main technique among others for application of polymers and was the method used within the thesis. Usually, coating finishes with a pre-dried polymer on the surface of a substrate requiring an additional soft-baking process that removes the rest of the solvent from the layer. This could be achieved either in a convection oven or on a hot plate. Baking on a hot plate used in the work as it is rapid (~1 min), in comparison to convection ovens (~30 min).

Soft-baking process is followed by an exposure step in a special mask aligning system (in this work mask aligners SUSS MA45 and SUSS MJB-4 were used) that collimates UV light, from high pressure discharge lamp projecting an image of a chromium mask mechanically aligned with the sample surface according to markers on both the substrate and the mask. Exposure could be done in several modes: in a contact mode providing high resolution, in a proximity mode that extends the mask lifetime, however significantly lowering the resolution, or in a projection mode. The last mode is used in direct writing systems i.e. HIMT uPG 501 Direct Write Pattern Generator (Heidelberg Instruments Mikrotechnik GmbH, Germany). In such a system, exposure performed without the mask forming the image by a digital micro mirror electro-mechanical matrix. Application of micro mirror matrixes gives a possibility to vary the layout immediately without mask fabrication process, which particularly important during optimization steps.

The exposure process of commonly available photoresists involves a UV light sources that could have wavelengths ranging from 450 nm to 365 nm; shorter wavelengths are applied for higher resolution and usually require special transparent for in deep UV light masks. During exposure of photoresists (light sensitive polymers) a set of photo initiators produces radicals or strong acids that alter physical and chemical properties of polymer e.g. solubility in organic or water based developers. Depending on the composition of the photoresist, they could be divided into positive or negative tone types. Regular positive tone photoresists initially has a low solubility in an alkali water based developers, however areas exposed to UV light became soluble. The negative tone photoresist works in an opposite way, exposed to UV light areas losing their solvability and remaining on the surface after the development process. Photoresist development process utilizes water diluted solutions of alkali metal bases or metal free organic bases such as tetramethyl ammonium hydroxide (TMAH). Depending on a kind of patterning, either etching or lift-off process, an appropriate combination of baking, exposure, and development processes should be applied to define structures with an appropriate edge profile. Because, the subsequent deposition step is usually very sensitive to the photoresist edge of produced structures causing severe problems, which requires a precise control over the overall photolithography process.

Achieved patterns have various edge profiles, which could be positive, negative or sharp depending on the photoresist type and development method. To achieve different slopes for lift-off or etching processes, different types of photoresists are available. Those photoresists could generate positive as well as negative and vertical edges during fabrication process or can be used in a combination achieving bi-layer systems of photoresists (Figure 3.1). As an example, the photoresist AZ 5214E (Microchemicals GmbH, Germany) with an image reversal property could be applied to achieve high positive or negative slopes. The image reversal behavior with a high negative slope is very useful for lift-off patterning of for instance e-beam or sputter deposited thin films, but patterning of thick films could relate to some difficulties due to the strong deposition on edges of the resist. In this case, the bi-layer photolithographic process could be applied. Here two layers of polymeric material are applied. The first layer is usually not sensitive to UV light while the second one is an appropriate type of photoresist. During the development process, the top photoresist layer form structures and a lower polymeric layer defines an under etch during the development process. Achieved layers function as a mask for deposited thin film. After the deposition, the sample is usually submerged into the solution of organic solvents to swell and dissolve polymeric layers though removing upper lying layers of thin films.

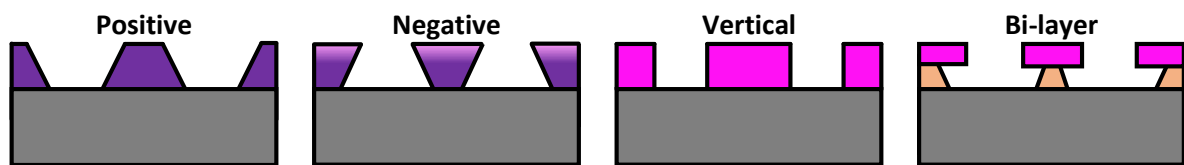


Figure 3.1: Profile of slopes for conventional photoresists. Violet photoresist includes the photoactive component, while bright-violet areas additionally include chemical amplifying components. Orange material is photo inert, but sensitive to the photoresist developer.

3.1.2 E-beam deposition

Electron-beam deposition systems are widely used for thin film technologies, providing a way to prepare metallic, semiconductor and dielectric layers. This technology uses a focused electron beam that can transfer energy from a power supply onto a small area of an ingot material heating it up, to achieve a sufficient vapor pressure. In this way, different materials could be evaporated at various rates depending on the applied power.

Generally, the electron beam evaporator (Figure 3.2a) consists of an electron gun, deflection system and a water-cooled crucible with a single or several target positions. An electron beam evaporator located in a vacuum chamber where the initial vacuum before the deposition is maintained at 10^{-6} mbar level. This is required to minimize the effect of residual gases onto the growth of the film and its chemical composition. In some cases, reactive gasses could be injected into the vacuum chamber i.e. oxygen, to prevent for instance the stoichiometry of oxide materials, perform reactive depositions or introduce deterministic defects into the film structure.

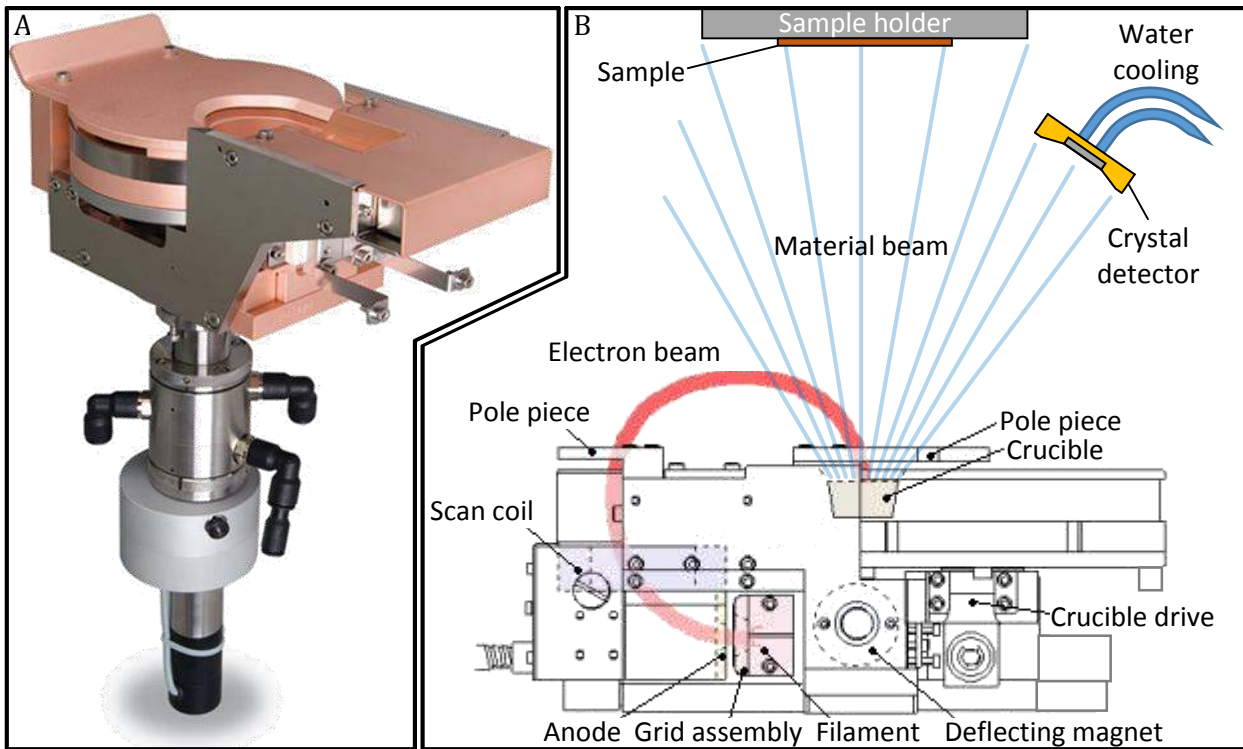


Figure 3.2: Construction of the electron beam evaporation device. A) Photograph of a commercially available electron beam evaporation cell with multiport rotating table to hold different materials at the same time. B) Transverse section of the electron beam evaporator. Electron beam (red line), emitted and accelerated between the filament and anode system, deflected by a permanent magnet towards the material, finally reaching a water-cooled crucible. At the same time to improve evaporation uniformity and material consumption, the electron beam can be additionally deflected by a scanning coil. Vaporized material propagates towards substrate and quartz microbalance to control the deposition rate. (Images are adopted from the JEOL Ltd.)

Electron gun produces a beam of electrons (Figure 3.2b), which are generated by a tungsten filament or a thermionic cathode, accelerated to the energy of 5 KeV and then collimated in an electron beam focusing system. To prevent the electron gun from being contaminated by the depositing material, the electron beam is usually deflected in the magnetic field of a permanent or an electromagnet up to 270° while the electron gun itself is placed below the ingot crucible. The ingot became hot and even melts due to the bombardment of its surface with the electron beam, converting kinetic energy of electrons into a heat at the upper surface of the ingot. Material could be deposited when a sufficient vapor pressure is achieved producing a constant rate towards the sample surface. The rate is controlled by a quartz microbalance introduced inside the vacuum chamber close to the working surface.

Within this thesis, electron beam (e-beam) evaporation was used for deposition of thin gold metal films that are patterned into conductive stripes of an antenna and contacts. The advantage of the e-beam deposition is that the angle of an incoming material beam at the substrate level close to 90°. The lift-off process can be easily applied using an image reversal photoresist AZ 5214E that gives a large negative edge slope of final patterns. Deposition on top of such structures using an e-beam

deposition gives a strong shadow under the slope providing a free access of the solvent to the photoresist layer at the lift-off stage.

3.1.3 Sputter deposition

Sputter deposition is another method, which allows formation of thin films on the surface of a sample. This method can be used for high rate deposition of almost all materials that are solid at normal conditions and materials with a complex composition such as alloys or oxides preventing variation of their stoichiometry between the sample surface and the target. Conventional design of the simplified sputtering device is presented on the Figure 3.3.

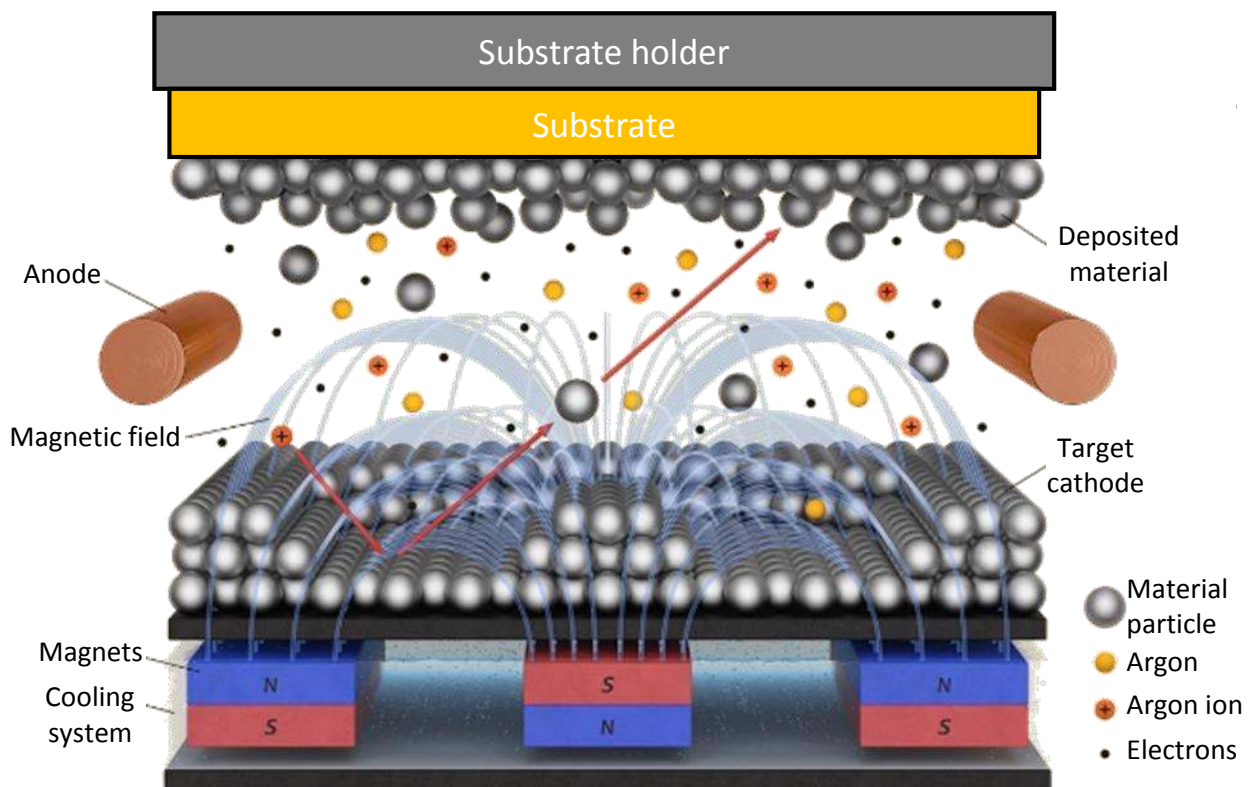


Figure 3.3: Simplified representation of the magnetron sputtering system. Image is adopted from the Farotex Limited.

For the deposition, in a vacuum chamber with a base pressure of 10^{-6} mbar filled argon (Ar) gas to the level of 10^{-3} mbar. Argon is used because it is not reactive and has a large atomic mass, which is important for a good material ejection from the target surface during sputtering process. At this pressure, a plasma ignites between the cathode and anode discharging ionized Ar gas. In this configuration, Ar ions accelerates towards the target material and during the bombardment of the target kicks-off target atoms in direction towards the sample surface at the same time secondary electrons are generated. In order to stabilize and increase density of the plasma in the vicinity of the target surface the discharge is formed in heterogeneous crossed electric and magnetic field configuration.^[351] Due to movement in the perpendicular magnetic field electrons affected by the

3 Fabrication and characterization methods

Lorentz force as a result, electrons moves along complex cycloidal trajectories near the cathode surface getting into a magnetic trap. This prevents electrons from reaching the sample surface and heating it up, and cycloidal movement significantly increases probability of argon ionisation maximizing the density of the plasma near the target surface. This results in higher intensity of ion bombardment of target surface and significant improvement in the sputtering speed. At the same time, material sputters extensively from the area with high density of magnetic field. This generates so-called racetrack, which limits target utilization (for planar magnetron could be between 20 - 50%). The magnetic field generated by a permanent magnet displaced bellow the actively cooled target. In this work, for deposition of thick metallic layers (nearly 2 μm) an industrial vacuum chamber (HZM4P) with planar 6" round DC magnetrons was used. The high deposition pressure and the large (comparable to the sample) size of the target provides a good step coverage in comparison to e-beam deposition. This property could cause however some problems with the edge coating if lift-off process is applied.

3.1.4 Chemical deposition

Nowadays, it is difficult to imagine production of state of the art devices without adhesion promoting and coupling agents. To this class of materials belong organo-silane coupling agents. Due to their chemical structure, they could be used to bond virtually any kind of surfaces providing possibility to link organic and inorganic materials (Figure 3.4a). The chemical structure of organo-silane coupling agents contain silanol reactive groups that enable chemical bonding to inorganic surfaces on one side and organo-functional group that bonds an organic material on another side. Depending on an application, several different reactive groups and structures could be chosen such as 3 - (Trimethoxysilyl) propyl methacrylate, which was used within the thesis work to promote bonding of polymeric materials to the glass surface. Usually organo-silanes are supplied in a non-reactive form promoting their stability and a storage time. For this purpose, the silanol functional group is protected with methoxy, ethoxy, or other stabilizing chemical groups that can be easily hydrolysed in a presence of water molecules to form a silanol function group. To hydrolyse methoxysilyl functional group for instance, such as presented in 3-(Trimethoxysilyl) propyl methacrylate, water should be presented near the molecule (Figure 3.4b). This could be achieved in several ways, either water is introduced in a solution of solvents and an organo-silane, or water could be absorbed from the surface of the material, where it could form about 4 monolayers in a humid environment (1% – 60%).^[352,353] After hydrolyzation, silanol groups orient towards the surface due to the hydrogen bonding (Figure 3.4c), where they react directly with hydroxyl group on the surface of almost any organic or inorganic materials. After heat treatment these bonds dehydrate forming stable covalent bonding between silane and the surface (Figure 3.4d, e).^[354]

Despite the high productivity yield of the water based silane solutions that are applied on an industrial scale, application of these solutions on a small laboratory scale is not feasible, mainly due to the ephemeral shelf-life nature of these solutions. Therefore, in this work, coating was made from anhydrous toluene solutions of 3-(Trimethoxysilyl) propyl methacrylate, which have long shelf life because the solution does not contain water. Hydrolyzation of the 3-(Trimethoxysilyl) propyl methacrylate monomers happens on the surface due to adsorbed water. Depending on amount of water on the surface one or more monolayers of the coupling agent can be formed. This results in a high surface density of the coupling agent at the interface, thus promoting adhesion of the further applied polymeric layer.

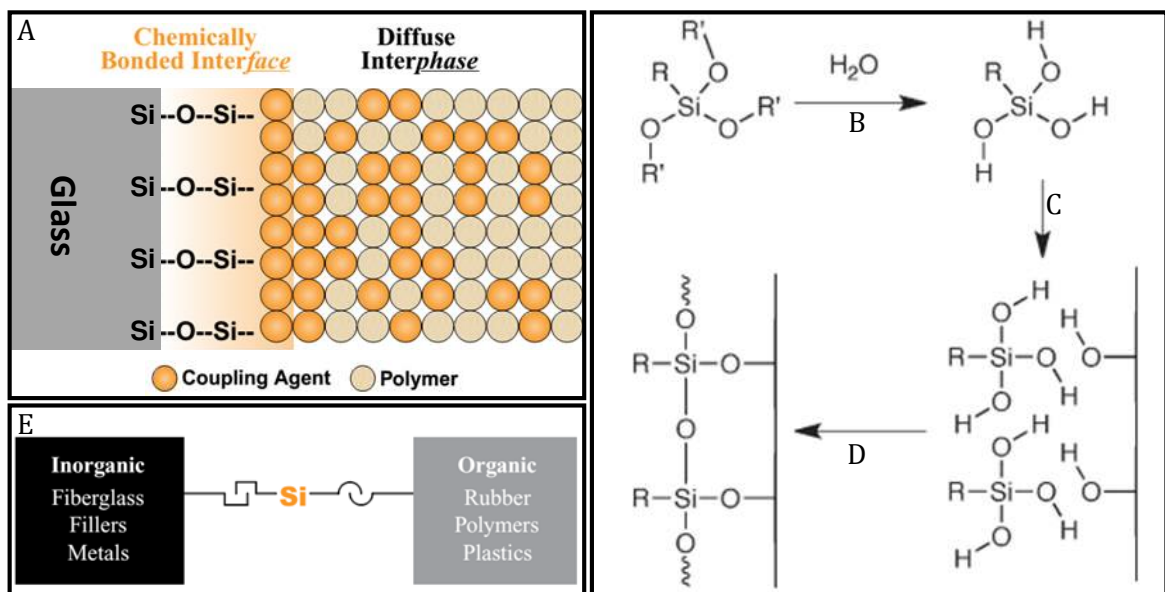


Figure 3.4: Chemical layer deposition. A) Adhesion improvement of the surface by introducing silane as coupling agent which has two types of functional groups, like the groups in the opposing materials B) Silane monomer is hydrolyzed by adsorbed water on the material surface or by addition water into the solution. C) Hydrolyzed silane is bonded to the surface through Hydrogen bonding interaction. D) During annealing, water is evaporated and silane monomers covalently bond to each other and to the surface producing a polymeric layer with functional groups on the other side. E) Virtually any type of materials could be bonded to each other if appropriate coupling agents are selected. Note: Images are adopted from [354,355].

3.2 Characterization methods

Fabrication of antenna structures requires a strong compliance of geometrical and electrical parameters acquired from electromagnetic simulations to achieve a comparable result. Thus, it is necessary to characterize structures at every experimental step using different methods. In this work, thickness and profile of polymeric layers as well as deposited materials were characterized using profilometry and scanning electron microscopy. High frequency characterization of the self-assembled structures was performed on a probe station equipped with a Vector Network Analyzer. The work was done on the equipment of the Institute for Integrative Nanosciences (IFW Dresden, Germany).

3.2.1 Profilometry

Polymeric self-assembly process that has been employed during the work for fabrication of antenna structures requires high reproducibility and a process control. To achieve this, slight variations in thickness of a newly synthesized materials should be avoided between batches. The easiest and most precise method for calibration of a new set of materials employed in the process is a mechanical thickness profilometry. In the work, a mechanical Dektak XT profilometer was used to calibrate the spin coating speed with respect to the achieved thickness (Figure 3.5a). The profilometer equipped with a diamond tip at the end of the stylus, which is touching the sample surface with a predefined force during a characterization process.

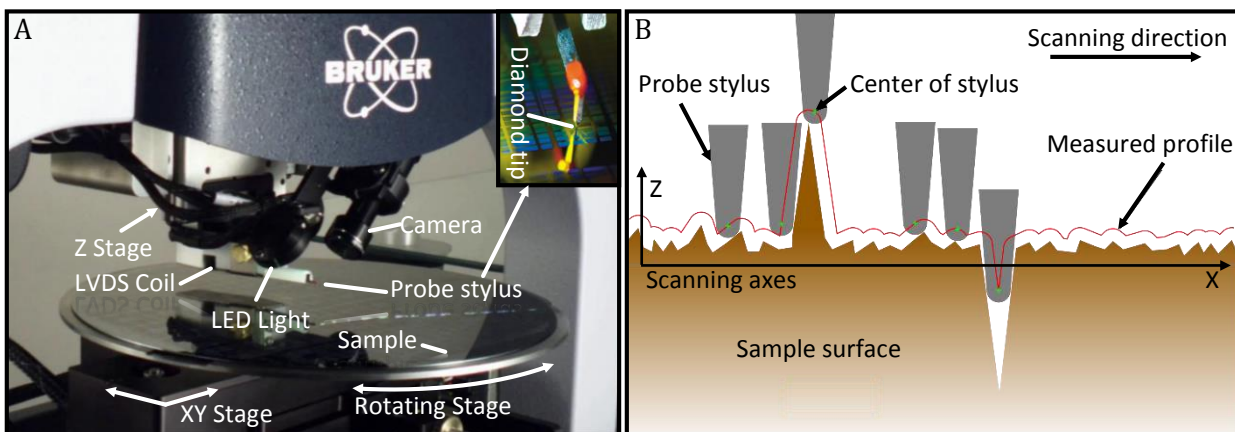


Figure 3.5: Stylus profilometry. *A) Photo of the Dektak XT stylus profilometer. The inset shows a close view of the probe stylus in contact with the sample surface (Image is adopted from Bruker). B) Schematic representation of the scanning process. Maximum resolution of the device is limited to the finite dimensions of the probe tip (Image is adopted from DoITPoMS, University of Cambridge).*

Scanning process is done along a line defined by a user with an optimal speed of a sample holder (Figure 3.5b). This prevents the stylus from jumping at the sample non-uniformities. It is important to take into account the tip geometry and dimensions determining minimum feature

resolution. During the scanning process, the surface profile is mechanically transferred through the stylus to a magnetic core of a linearly variable differential transformer (LVDT). Small variations in the magnetic core position produces an analog signal that is converted into a voltage or a current. A controlling computer can then record the signal after digitization by an analog-to-digital converter.

3.2.2 Vector network analyzer

Development of antennas is always joined with a highest possible power transmission efficiency, this is especially important nowadays when mobile and portable devices cannot effort a large energy loss due to inefficient radio transmitting systems that are mainly relying on well-designed antennas. In order to gain information about efficiency of antennas it is common to use vector network analysis.

The basic schematic of a vector network analyzer is presented on the Figure 3.6. It consist of a continuous wave generator that has a possibility to sweep frequency and a power level, and radio receivers. It allows also variation of a signal direction through one of two ports to which device under the test (DUT) is connected. The network analyzer sweeps the frequency of the wave generator. Then the signal analyses as an amplitude ratio and a phase shift of a reflected and transmitted signals through the DUT with respect to the incident test signal providing a complex impedance value relative to the reference impedance. These values are given as reflection and transmission coefficients i.e. S_{11} , S_{12} which commonly represented in logarithmic unit-less scales.

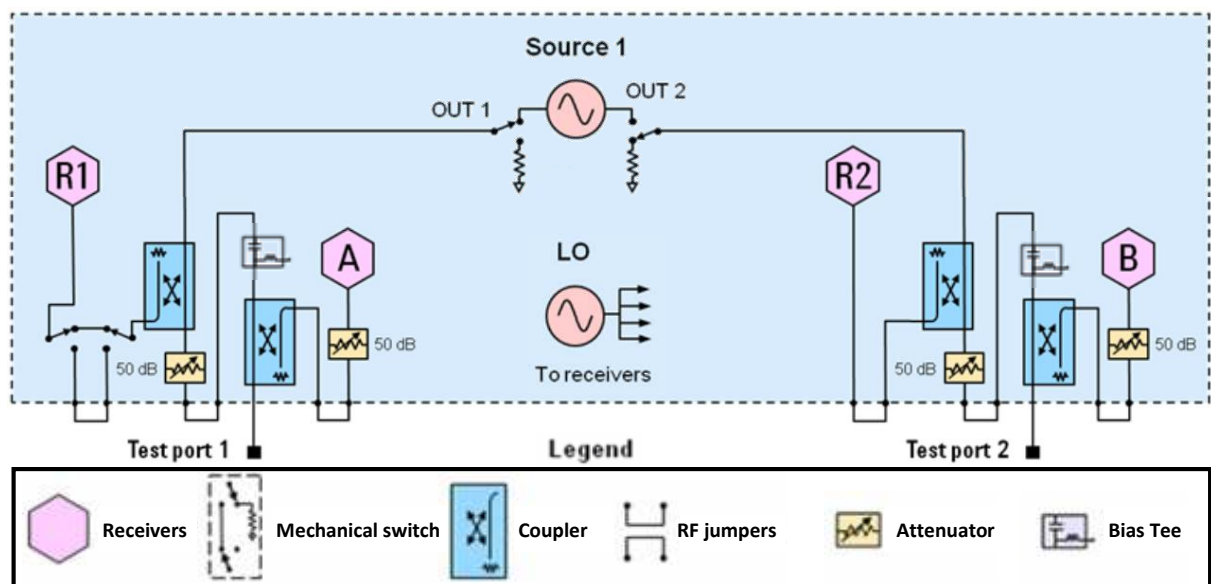


Figure 3.6: Schematic representation of a network analyzer. (Image adopted from Keysight Technologies)

In this work, S_{11} and S_{12} are main parameters that characterizes the rolled-up helical antenna. For probing of antenna parameters a CASCADE PM-8 probe station and Agilent E5071 vector network analyzer were used. This configuration allows characterization in the frequency range from 300 kHz up to 20 GHz. Electrical connection to antennas was realized via a GSG CASCADE Z-micro-probes. To

3 Fabrication and characterization methods

eliminate the coupling effect of the reactive near field of the antenna and the metallic parts of the probe station, all experiments are done on a 20 mm thick PTFE block.

3.2.3 Scanning electron microscopy and focused ion beam milling

An SEM is an essentially powerful tool for investigation of a micro object structure at sub micrometer scales down to several nanometers. SEM (Figure 3.7) uses electrons accelerated to high-energies and focused on the sample surface by electrostatic and electromagnetic lenses. High energy of electrons required for a small de Broglie wavelength of electrons in SEM systems to overcome diffraction limit that usually affects resolution of a standard optical microscopy. The electrostatic deflection system allows scanning of the focused electron beam over the surface of an object with a very high precision. After approaching the surface, energetic beam of electrons generate photons and a variety of back scattered electrons. Electrons could be scattered at the surface in an elastic and an inelastic way.^[356] Inelastically scattered electrons dissipate their energy in the sample surface, some sample electrons could get enough dissipated energy to leave the sample as a secondary electrons (SE). Elastically scattered electrons change their propagation trajectory without a significant loss of energy, during their interaction with atoms of the surface, they could be reflected back generating so-called back scattered electrons (BSE). Intensity and amount of BSE depends on density of the material and weight of atoms enabling a chemical sensitivity. When BSE scatters before leaving the surface, they generate the so-called SE2 electrons. For the surface imaging, SE and BSE electrons commonly used. SE provides information about morphology and topography of the surface, whereas BSE has better contrast for multi-layered hetero-structures.

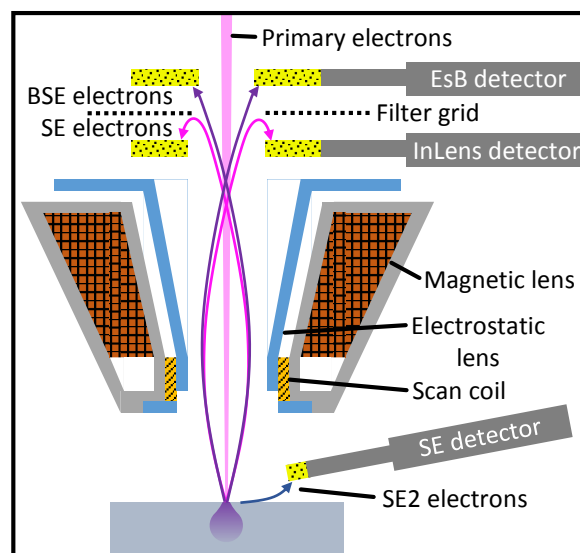


Figure 3.7: Construction of a scanning electron microscope. (Image adopted from W. Kuo^[357])

Imaging is done by focusing of an incident electron beam into a small (several nm`s) spot onto the sample surface and acquisition of scattered electrons or generated photons. Depending on the required magnification, electromagnetic coils or electrostatic system could deflect electrons to a

different defined angle performing horizontal and vertical scanning across the bigger or smaller area of interest. Each such exposure of the surface to the electron beam and acquisitions sequence represents a pixel of visualized information on a monitor. The sequential acquisition of the information from different positions on the surface gives a two dimensional image of the surface. If surface is not conductive it could charge and affect the image quality, to prevent this and make surface conducting, a thin layer of material with low electric resistivity can be applied on the sample.

Sometimes, it is important to access the morphology of hidden under the surface structures. This is achieved with a help of the focused ion beam (FIB) milling process. FIB milling employs gallium ions due to the Ga low temperature melting point (around 30° Celsius) and its vapor pressure. Ga ions accelerated and focused in an ion gun system towards the surface of the sample milling and removing away atoms from the surface. Then an SEM is used for imaging of the processes region. This method was used for imaging samples with double layer lithographic stack after deposition of thick metal layers.

4 Platform for self-assembled structures

This chapter describes development of novel polymeric materials that allow self-assembly of planar structures into three-dimensional geometries. The materials are optimized for use in regular semiconductor photolithographic processes such as spin coating, drying, exposure and development. During optimization, a special attention was paid towards adhesion between polymeric layers as well as adhesion to underlying support. During the work three different polymers were synthesized namely the sacrificial layer, the hydrogel layer and the rigid polyimide layer. The polyimide as a material was chosen for its outstanding performance enabling its widespread application in electronics and microelectronics. All of the developed materials could be applied on the area as high as 100x100 mm² allowing fabrication of three-dimensional self-assembled structures in an array configuration, with a high yield of almost 100% and a great reproducibility. A direct photopatternability of the materials allow rapid optimization of device geometries due to skipping additional photoresist based steps. Following data is adapted from the earlier published works.^[29,32,59,358-362]

4.1 The sacrificial layer

Several requirements were settled during the development of the sacrificial layer e.g. simple processing using conventional thin-film and photolithography techniques, patternability using standard 365–405 nm exposure sources, stability against high temperatures, inertness in common organic nonpolar, polar protic and aprotic solvents, as well as moderate bases and acids. These requirements was possible to achieve in a metal-organic framework based on an acrylic acid (AA) as a ligand coordinated to lanthanum (La) ions.

Acrylic acid and hydrated LaCl₃ were obtained from Alfa Aesar UK and used without further purification. Firstly, 10 g of AA was converted to an alkali metal salt using sodium hydroxide (NaOH) (Sigma-Aldrich Co. LLC., Germany). For this 10 M/l of NaOH were dissolved in DI water and added to the AA until the solution reaches pH of 5.5. At this value more than 60% of the acid is presented in the ionized form (Figure 4.1a). The corresponding pH value (with an accuracy of ±0.01 pH) of the solution was measured using a pH meter CyberScan PC510 (Eutech Instruments Pte Ltd., Singapore). To this solution was added a predissolved LaCl₃·7H₂O in a proportion of COOH:La = 7:1 to acid group presented in the solution (Figure 4.1b) resulting in an amount of 7.36 g. The lanthanum was dissolved in 10 ml of DI water and pH was adjusted to 5.5 by NaOH, at which it presents mainly in ionic form.^[349] Mixing of both solutions decreases pH from 5.5 to 5.0 indicating that ionized AA as well as not ionized AA participate in coordination with La³⁺ ions producing protons.^[349,363] The solution was stirred for 30 min using a magnetic stirrer. During this time pH was slowly increased to 10 by adding

4 Platform for self-assembled structures

NaOH (Figure 4.1c), where additional precaution was taken in the pH range from 9.5 to 10 due to the delayed reaction of the system,^[349] it was found, that 5 min delay between droplets is sufficient to get system into equilibrium. At this pH lanthanum complex form a white precipitate, which was collected using a filter paper and a vacuum exicator.

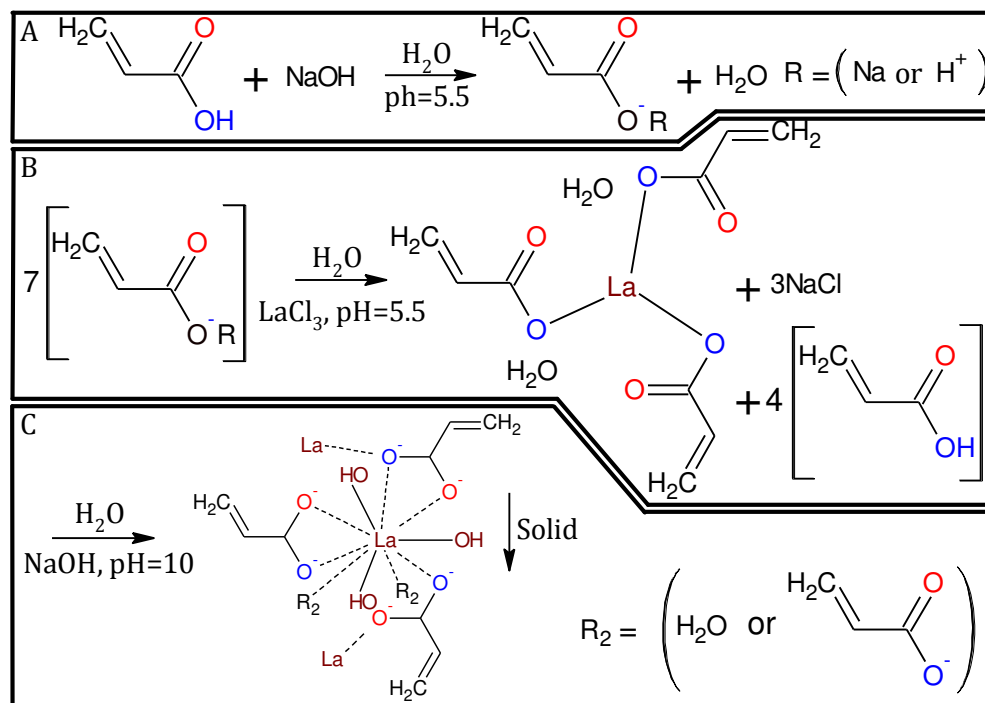


Figure 4.1: Synthesis steps for the sacrificial polymer material. A) Addition of NaOH solution to the acrylic acid up to pH 5.5, the main part of the acid becomes ionized and is present in a salt form of Na^+AA^- . B) Solution is mixed with LaCl_3 , where the La complex with AA was formed. C) The La complex is precipitated from the solution at elevated pH levels.

Then, the precipitate was washed with 500 ml of DI water adjusted with NaOH to pH 10 and finally washed with 200 ml of regular DI water. Acidity of the obtained slurry was tested using litmus test paper (DuoTest, Macherey-Nagel GmbH & Co. KG, Germany) and was around 6.8 demonstrating that there all non-reacted components were washed away. The collected material was dried on a hot plate at 35 °C for 12 h under nitrogen conditions with a final weight of 4.68 g. Further, the dried material was dissolved in AA at the concentration of 33% (wt/wt). At the end of preparation, the solution was photosensitized using 2% (wt/wt) of 2-Benzyl-2-(dimethylamino)-4-morpholinobutyrophenone and 4% (wt/wt) methyl diethanolamine (MDEA) (Sigma-Aldrich Co. LLC., Germany).

4.2 The hydrogel layer

The hydrogel polymeric layer was applied in the platform with a goal to generate mechanical strain and change the geometry of top lying layers. The hydrogel layer is reinforced by a rigid layer and thus should have a good adhesion to top and bottom layers made of polymers. Patterning of the layer could be made in a way as a regular photoresist by means of photolithography techniques. For the

preparation of the hydrogel layer was used poly(ethylene-alt-maleic anhydride) (PEMA) and N-(2-hydroxyethyl)methacrylate (HEMA) (Sigma-Aldrich Co. LLC., Germany). After hydrolysis of anhydride groups and their further esterification reaction of the PEMA and hydroxyl groups of the HEMA. Resulted grafted polymeric chain could swell in an alkali aqueous media due to carboxylic groups, which are responsive to a pH level of an environment. When the hydrogel polymer is reinforced with another rigid polymer swelling will result in a differential strain and change in the geometry of the layer stack.^[364-368]

The hydrogel layer was prepared as follows, at first, 6 g of PEMA has been dissolved in the 50 ml of N,N-Dimethylacetamide (DMAc) (Sigma-Aldrich Co. LLC., Germany) at 70 °C for 10 min. After cooling down, to the solution was added 5.66 g of HEMA and then everything was mixed thoroughly for 24 h at room temperature by magnetic stirrer to finish reaction with PEMA (Figure 4.2a). At the end the solution was photosensitized with 2% (wt/wt) of 2-Benzyl-2-(dimethylamino)-4-morpholinobutyrophenone and additionally diluted in proportion 2 to 1 with DMAc. To remove undissolved material and contamination, solution was filtered through a 1 μm glass fiber syringe filter, applied on the surface of samples using a spin-coating equipment and placed on a hot plate for drying at 50 °C.

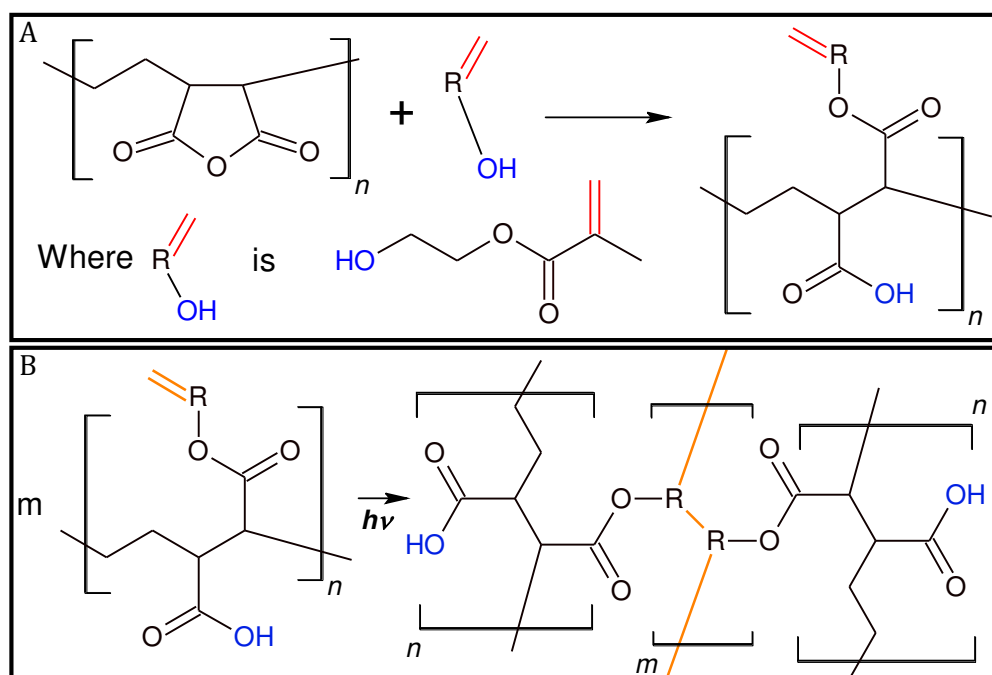


Figure 4.2: Synthesis steps for stimuli responsive polymer material. *A) Hydrolyzation of the anhydride group in the PEMA and esterification, resulting in the addition of methacrylic group to the polymer chain. B) By applying UV radiation in the presence of a photoinitiator a free-radical chain polymerization of the polymer is initiated. R group represents a HEMA monomer.*

After the drying, samples were exposed to a broadband UV source through a glass mask using a commercial mask aligning system. UV radiation generate radicals braking photoinitiator molecules and initiating free radical chain polymerization of acrylic groups in HEMA (Figure 4.2b).

4 Platform for self-assembled structures

Development is done in the diethylene glycol monoethyl ether (DEGMEE) (Sigma-Aldrich Co. LLC., Germany) by dissolution of non-exposed areas without affecting exposed (cross-linked) parts. Thickness of layers could be in the range from 1500 nm to 500 nm, when spin coated at speed from 1000 rpm to 5000 rpm for 35 s, respectively. An annealing step is required at temperatures of more than 150 °C to significantly improve stability of the layers at further photolithographic steps. At these temperatures polymer undergoes a dehydration process with formation of anhydride functional groups further crosslinking and passivizing the polymer.^[369]

4.3 The polyimide layer

Reinforcing rigid layer was specially synthesized to meet requirements including thermal, chemical and mechanical stability, good adhesion to the hydrogel layer and a direct UV patternability. A UV patternable polyimide system was chosen as it could satisfy all the requirements and could be applied from its polyamic acid precursor solution (Figure 4.3). The polymer was prepared by reaction of two monomers, containing amine and anhydride reactive groups, 4,4'-Methylenedianiline (MDA) (Sigma-Aldrich Co. LLC., Germany) and 3,3',4,4'-Benzophenonetetracarboxylic dianhydride (BPDA) (Sigma-Aldrich Co. LLC., Germany) respectively dissolved in DMAc. UV sensitivity and insolubility of exposed areas during developing process (Figure 4.3b) was achieved by modification of the polymer with photo-initiator 2-Benzyl-2-(dimethylamino)-4-morpholinobutyrophenone (Sigma-Aldrich Co. LLC., Germany) added in a concentration of 4% (wt/wt) and a crosslinking agent Dimethylaminoethyl methacrylate (DMAEMA) (Sigma-Aldrich Co. LLC., Germany) added in a 1:1 ratio with number of carboxylic groups in the polyamic acid respectively. The polymerization of polyamic acid achieved as follows by mixing 12 g of BPDA in 6 ml of DMAc. Next, 19.65 g of the diamine MDA was dissolved in 6 ml of DMAc at 60 °C and added to the first suspension initially cooled down to 15 °C. Reaction of both components resulted in a viscous solution of polyamic acid. The solution was left in the mixer for 4 h under cooling conditions to complete the reaction. Achieved solution was additionally diluted with 300 ml of DMAc to achieve a desired viscosity and photo activated with 18.86 g of DMAEMA. DMAEMA forms an ionic bond between its tertiary amine group and a carboxylic acid in the polyamic acid solution (Figure 4.3b) taking approximately 6 h at room temperature until it uniformly distributed and completely reacted. Finally, 0.75 g of photoinitiator was added into the solution.

The photosensitive polyamic acid solution was filtered through 1 um glass fibre filter to remove undissolved particles and then drop casted on the surface of glass substrates for a subsequent spin-coating with a speed in the range from 2000 to 5000 rpm for 35 s, producing at the end structures with a thickness of 2000 nm to 800 nm respectively. Then, predried at 50 °C, polymeric film was exposed to a broadband UV light through a chromium glass mask. Acrylic groups of DMAEMA undergo a free radical chain polymerization forming two linear chains of polyamic acid and

polymerized DMAEMA that are crosslinked through ionic bonds (Figure 4.3c). As a result, exposed areas are more stable during development in organic solvents. However, the exposed areas are still slowly dissolving in the developing solution and an appropriate justification of development timing is essential.

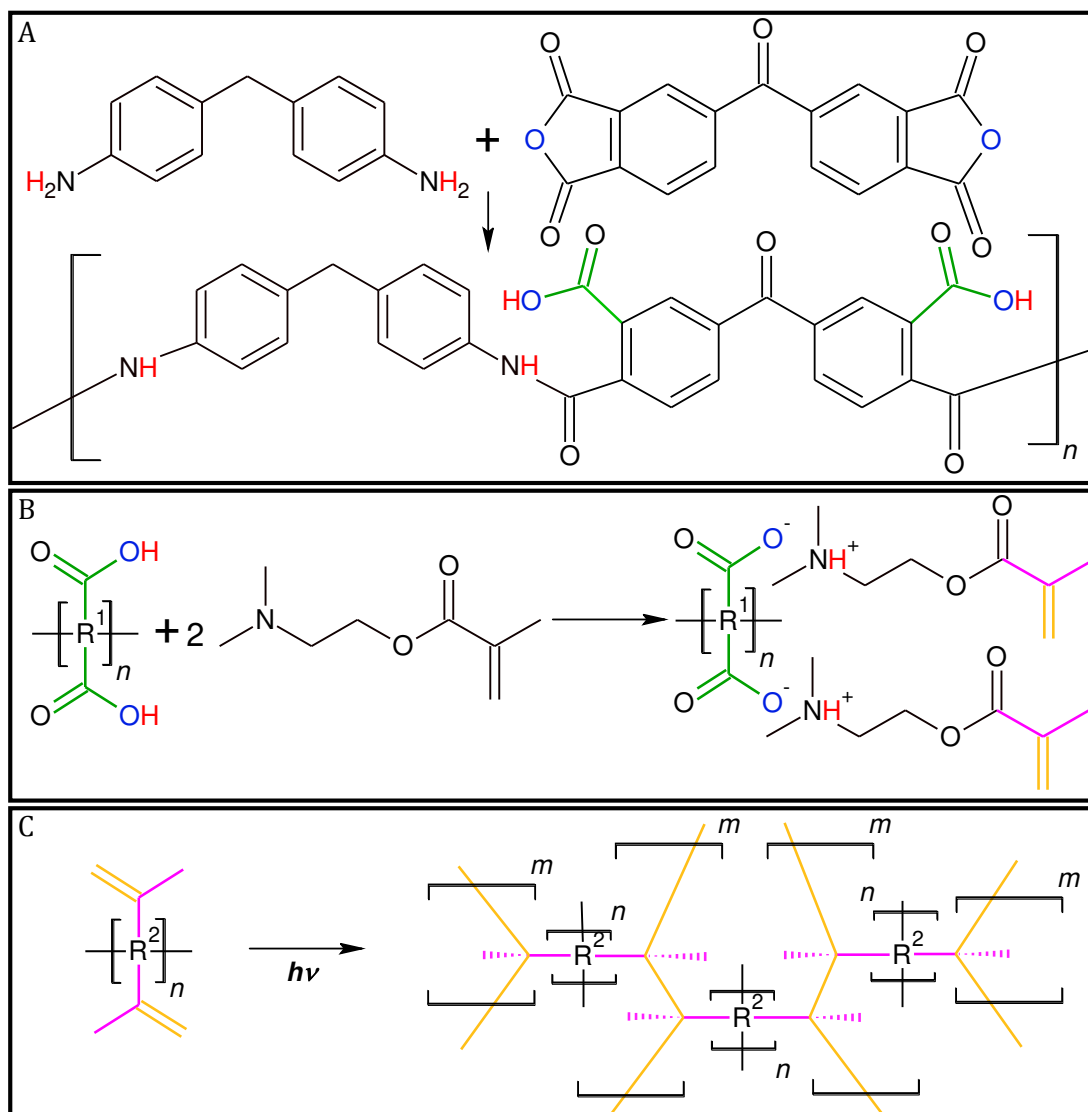


Figure 4.3: Synthesis steps for the polyimide material. A) Reaction condensation between MDA and BPTDA monomers to form a polyamic acid. B) Polyamic acid in a simplified form with functional carboxylic acid groups and its modification with DMAEMA, as photoactive component. C) UV exposure of a photosensitive polyamide material and its cross-linked form after the free radical chain polymerization.

Additionally, PI requires an additional attention due to its structure. Polymer contain a benzophenone (BP) derivative, which is also sensitive to UV radiation depending on groups connected to it.^[370–372] Because in this work no UV filters was used, BP could also crosslink the polymer. BP, absorbing a photon, activates to its diradical state BP*. At this state BP* can abstract aliphatic hydrogen from the nearest group in its vicinity or recombine to the ground state. If hydrogen abstraction happens, two radicals are generated in the aliphatic group and BP. This reaction of BP is presented in the Figure 4.4a. Formed radicals can initiate a free radical chain

4 Platform for self-assembled structures

polymerization of acrylic groups or could be recombined with each other creating a covalent bond. As it was mentioned previously, this reaction can begin deep inside the polyimide material and on the interface with the hydrogel layer leading to the covalent attachment of this chain to the hydrogel layer.

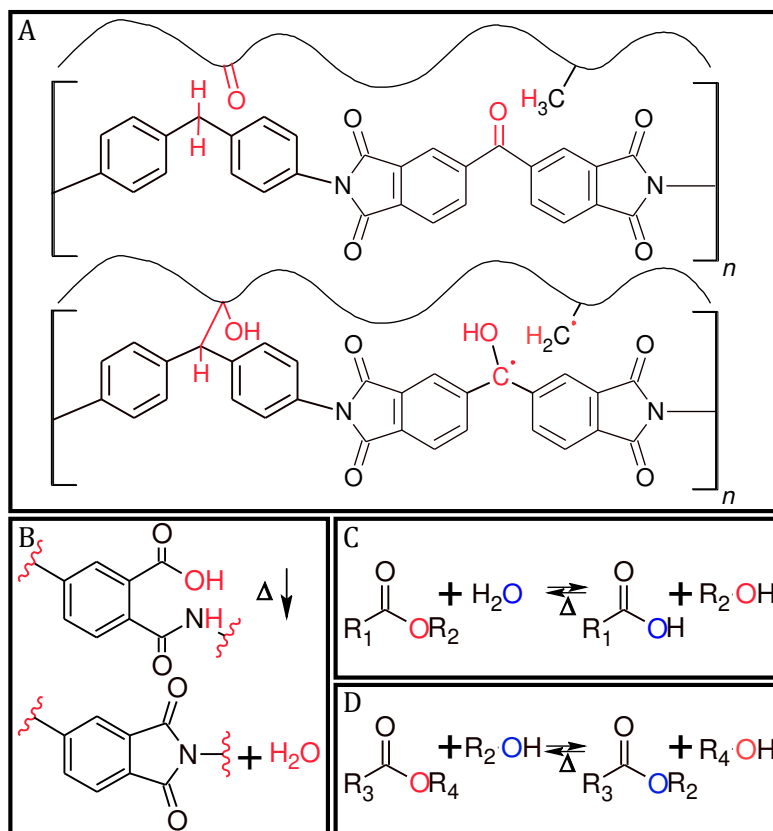


Figure 4.4: Different attachment mechanisms of the PI layer to the HG layer. A) Photo-induced radical reaction between benzophenone part of the polyamic acid and aliphatic groups. B) Imidisation of the polyamic acid. C) In presence of water after imidisation process, ester groups in DMAEMA and HEMA undergo a hydrolysis reaction with production of carboxylic acid and alcohol components. D) Transesterification reaction.

Also, during imidisation process of the polyamic acid at high temperatures water is generated (Figure 4.4b). During evaporation process, water could react with esters on the interface of two polymeric layers, in the DMAEMA and stimuli responsive material. In the water presence and high temperatures esters hydrolysis (Figure 4.4c) producing carboxylic acid and alcohol, this reaction is reversible until water presents in the material.^[373,374] On the interface of two layers at elevated temperatures could appear transesterification reaction^[373] (Figure 4.4d) and as result will be introduced interpenetrating poly(metha acrylate) chains into both material, introducing additional bonding of one layer to another.

Patterns of the polyamic acid layer was made with an overlap of the hydrogel layer to protect it from the polyamic acid developer. Developer for the polyamic acid was adjusted to achieve a high contrast of exposed areas to unexposed ones. Unexposed parts dissolve in the developer while exposed does not. The developer solution was composed of several solvents as follows: 4 part (v/v) 1-Ethyl-2-pyrrolidone (NEP), 2 parts (v/v) of DEGME and 1 part (v/v) of ethyl alcohol. All of the solvents were

mixed together and the exposed sample was immersed in there for 1 min with a subsequent rinsing in propylene glycol monomethyl ether acetate (PGMEA)(Sigma-Aldrich Co. LLC., Germany). So achieved polyamic acid structures were imidized using initially a post bake at 90° C for 1 minute, removing excess of solvents in the film preventing formation of bubbles in the volume of the film at a hardback step. The imidization process is made on a hotplate under a nitrogen condition at 220 °C. for 10 min.

4.4 The polyimide for bi-layer lift-off process

A polyamic acid solution (Figure 4.5) composed of MDA and 3,3',4,4'-Pyromellitic dianhydride (PMDA) (Sigma-Aldrich Co. LLC., Germany), which are contain amine and anhydride reactive groups respectively, was reacted together to achieve a polymer for bottom layer in a bi-layer lift-off process. Synthesis is done as follows 1.09 g of PMDA was dispersed in 5 ml of DMAc. This dispersion was reacted with a 1 g solution of MDA in 5 ml of DMAc. The amine solution was rapidly poured into the PMDA dispersion and reacted for 6 h at 15°C in a mixer. The obtained solution was diluted with 5 ml of DMAc and 3 ml of NMP. Finally, the solution was filtered through 1 um filter. The achieved polymer has a good coatability and can be dissolved in an alkali-based developers. In a combination with a regular photoresist on top of this polymer a substantial undercut could be achieved, which is of a big advantage for a lift off process.

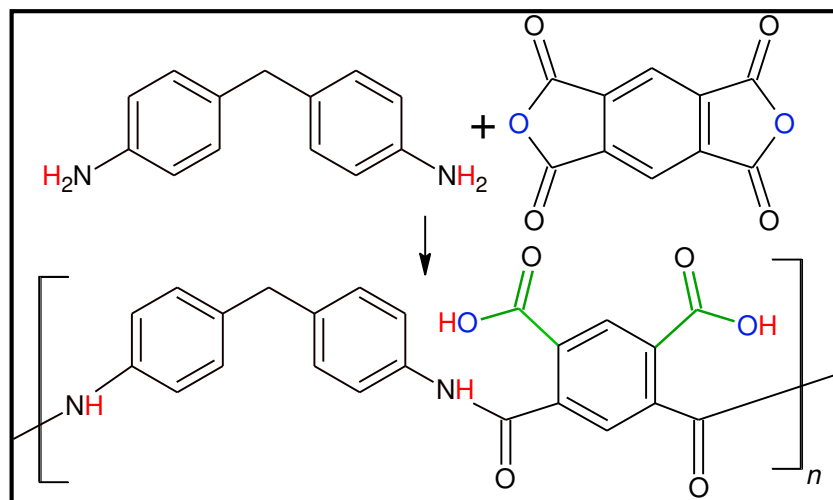


Figure 4.5: Synthesis steps of bottom resist for the bi-layer photolithographic process. Reaction condensation between MDA and PMDA monomers with polyamic acid, as their product.

4.5 The frame solution

The so called “frame solution” was used as a part of an encapsulation process and based on a photosensitive material that can be temporally applied on the surface of a sample via a direct laser exposure to form a frame around the device that should be encapsulated. Then, in the surrounded volume was applied an encapsulation solution, which is then cross-linked. Finally the frame solution

4 Platform for self-assembled structures

can be hydrolyzed and dissolved in an alkali solution leaving a well-defined encapsulated device. To prepare the frame solution, acrylic acid, triethylamine (TEA) (Sigma-Aldrich Co. LLC.) and poly acrylic acid (PAA) (Sigma-Aldrich Co. LLC.) with molecular weight of 450000 were used. First, 0.1 g of PAA was dissolved in 10 g of AA. Then solution was modified with the equivalent molecular amount of TEA (14.04 g to AA), which was added drop-wise during the stirring process under a water cooling condition until the product stops fuming. This process, in a presence of common tertiary amine, links acrylic acid to PAA through hydrogen bonding of two carboxylic acids in AA and PAA resulting in a moderately stabilized dimer of carboxylic acid salt (Figure 4.6).^[375] Because reaction occurs in the excess of AA dimers are also formed between acid monomers, as a result a highly viscous solution was obtained.

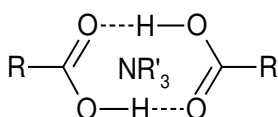


Figure 4.6: Dimer of carboxylic acids in the presence of tertiary amine. Where R is AA or PAA and NR₃ is TEA. (Image was adopted from ^[375])

Then, this pre-polymer was diluted to a desired value with 30 g of AA and photosensitized by 5% (wt/wt) of 1-Hydroxycyclohexyl phenyl ketone (Alfa Aesar). This solution is sensitive to the laser with the wavelength of 365 nm (Coherent Inc., USA) and is liquid before exposure. In a liquid state the solution is applied on the surface of the sample reaching a sufficient thickness of the layer. The material was exposed in defined places with a help of computer controlled X-Y motorized stage and the laser system. Then the surface of the sample was cleaned with acetone to remove liquid “frame solution” from the surface.

4.6 The encapsulation solution

Encapsulation of the antenna is the vital step in the fabrication process, which serves as a boundary between antenna and biological environment, and as a dielectric media, that affects the performance of the antenna itself. As a result, it must fulfil many requirements. For bio-applications, material needs to be nontoxic, non-irritating to tissues, being inert to biological fluids and do not decompose in highly aggressive environment for a long period of time. At the same time, antenna applications require usage of high dielectric constant materials to reduce an overall antenna size.

In the encapsulation process UV-curable monomers and polymers in a liquid form were used containing diacrylate functional groups. Liquid form of the material is required to reduce the load on antenna during the encapsulation process. These materials are also known for their bio-compatible properties, has small volumetric shrinkage during polymerization, good mechanical characteristics and low water absorption: 1,6-hexandiol diacrylate (HDODA)^[376-378], bisphenol A-glycerolate (1

glycerol/phenol) diacrylate (bis-GA)^[379-381] and poly(ethylene glycol) diacrylate (PEGDA) MW=250 and 700^[376,378] and AA, were purchased from Sigma-Aldrich LLC and used without further purification.

Due to the high viscosity of bis-GA 9 g of the monomer was mixed in the following proportion with 6 g of HDODA, 9 g of PEGDA (MW=250), 4.5 g of PEGDA (MW=700) to decrease its viscosity and improve flow-ability in order to fill internal volume of antenna with a help of capillary forces. For a better adhesion of the encapsulation material to the glass, 2 g of AA and 0.5 g 3-(trimethoxysilyl) propyl methacrylate (Polysciences Europe GmbH, Eppelheim, Germany) were added to the solution. Then the solution was photo activated with 2% (wt/wt) 2-benzyl-2-(dimethylamino)-4-morpholinobutyrophenone. All components were thoroughly mixed until a complete dissolution. To increase dielectric constant of the polymer, 0.5 g of Barium Titanate (BaTiO_3) (Sigma-Aldrich LLC) was added into 2 g of the prepared solution.

Before mixing with the solution, BaTiO_3 powder was silanated to enhance the bonding strength between the inorganic filler and organic binder, and as result also improving mechanical properties of the structure. BaTiO_3 powder was sonicated with 1% (wt/wt) 3-(trimethoxysilyl) propyl methacrylate in acetone for 1 h achieving a layer of the silane on the surface of particles. The dispersion was washed with acetone and left in a Petri dish for 30 min under nitrogen conditions to evaporate the remaining acetone. The process was followed by dehydration at 120 °C on a hot plate, to accomplish silanation and form covalent bonding of the silane and an oxide material. Then both powder and the solution were homogeneously mixed. After that, internal area of the frame was filled with the suspension and the sample was exposed with a lamp having a 450 nm wavelength.

5 Results and Discussions

Development of complex systems that integrate various interdisciplinary parts often associated with difficulties of bridging among single components. Similarly, development of a novel platform that allows a high yield and efficient fabrication of self-assembled micro scale antennas for in vivo implant applications embrace high frequency electro dynamical, chemical, thin-film mechanical, electromagnetic safety and biocompatibility aspects. In the thesis, the bridging among different sides of the platform was performed experimentally, strongly involving finite element methods (FEM) of a universal platform from ANSYS Inc. to model mechanical behaviour. Results of FEM electromagnetic and mechanical modelling for novel antenna design and its mechanical self-assembly processes were compared with experimentally fabricated structures. Mechanical behaviour of polymeric rolled-up platform presented in the subchapter 5.1 while the simulated and measured electrical characteristics of antennas are shown in subchapters 5.2 – 5.3 with respective comparison. Behaviour of achieved helical antenna in vicinity and inside a human body model was also simulated and safety conditions were defined to comply with the accepted international recommendations. The discussion and figures in this chapter are adopted from publication NPG Asia Materials 2015 (DOI: 10.1038/am.2015.53), titled “Compact helical antenna for smart implant applications”.^[359]

5.1 Modelling of the compact helical antenna

Simulation and fabrication of high frequency antennas, especially compact size antennas, can be effectively managed if a correct model is proposed. An adequate modelling of radio frequency components is required and was done with help of an FEM software packet. A precise understanding of electromagnetic behaviour of components, the possible distribution of electromagnetic fields in the near environment (so called near field) and conditions that lead to the long-range emission of the electromagnetic energy should be recognised and implemented in the model. Thereby, a correct comparison between real radiofrequency measurements and a model can be done only when a surrounding environment is considered, which became especially critical when operation frequencies approaching values of wavelength with a characteristic scale comparable to surrounding objects. Particularly, details of a characterization environment i.e. a probe station should be considered. However, the components itself, especially a self-assembled structure may have a distribution in its geometrical parameters such as diameter, length, offset due to the miss assembly, variation in thicknesses of layers from process to process etc. These details should be analysed to understand the overall electromagnetic performance and stability of antennas as well as an efficiency of the fabrication process. These details addressed in the following discussions.

5 Results and Discussions

5.1.1 Definition of parameters and 3D geometry of an electromagnetic environment

To minimise geometrical mismatch between experiment and simulation, a 3D environment was reproduced in the model closely replicating the real environment (Figure 5.1a) and the exact geometry of components was considered in the experimental setup. Critical parameters include dimensions of antennas, their separations, polytetrafluoroethylene (PTFE) blocks located on metal chuck of a probe station, parts of microwave probe manipulators with probes itself reproducing geometry of “|Z|-probes” and EPS200RF measurement station based on the PM-8 probe system (Cascade and Microtech, Inc., Thindorf, Germany) as well as the front lens of microscope and a light source (Figure 5.1b). To improve speed of S11 parameter simulation during parametric sweeps the model then gradually simplified to the level where it could still satisfy geometrical compatibility. Considering possible resonances around 2.45 GHz all objects at the distance of 125 mm from antennas were left in the model as it is shown on Figure 5.1b. Excitation in the model was performed through a lumped port with an impedance of 50 Ohm corresponding to real situation using the |Z|-probe.

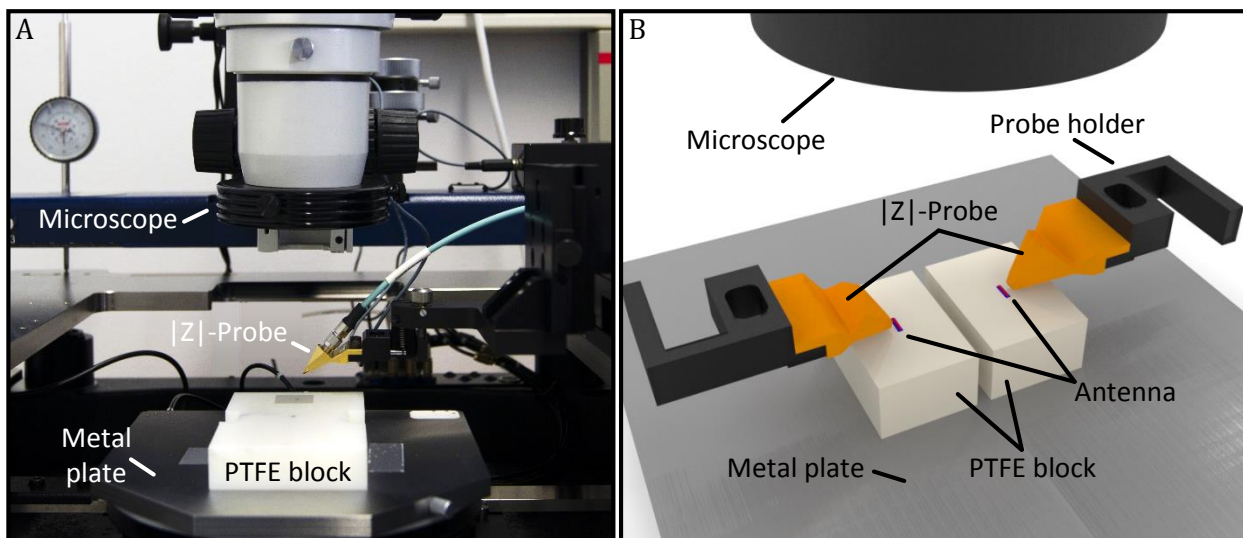


Figure 5.1: Model for high frequency simulation. A) Experimental setup dedicated to electrical characterization of self-assembled helical antennas. B) Model of the experimental setup for simulation of S12 parameters.

5.1.2 Helical antenna layout and optimization of geometrical parameters

To build up a helical antenna using the rolled-up technology a planar layout was considered (Figure 5.2a). This layout is technologically simple requiring only one photolithographic step forming metallic conductors on top of an initially planar polymeric stack (Figure 5.2b). When antenna assembled, diagonal conductors form a helical structure between windings of the rolled structure (Figure 5.2c), providing a starting point for optimization of electromagnetic characteristics with respect to geometric parameters. The final step of the process is an encapsulation of antenna

handling two functions (Figure 5.2d), adjusting the dielectric constant of the antenna environment to effectively reduce resonance frequency and protection from mechanical impacts. As it was discussed in the chapter 2, a biological surrounding will reduce the effective resonance frequency to almost half of its initial value (Figure 2.6 in Chapter 2). Therefore, an antenna initially operating at 5.8 GHz in air should have desired 2.4 GHz resonance frequency in a biological environment that works as an additional dielectric environment. Keeping in mind this important detail the development of the compact helical antenna is focused on the final 5.8 GHz resonance frequency. Still higher frequencies (up to approximately 8 GHz) are allowed for the not encapsulated helical antenna as the resonance could be adjusted towards lower frequencies using high-k dielectric materials^[235] e.g. BaStTiO₃^[382], TiO₂^[383].

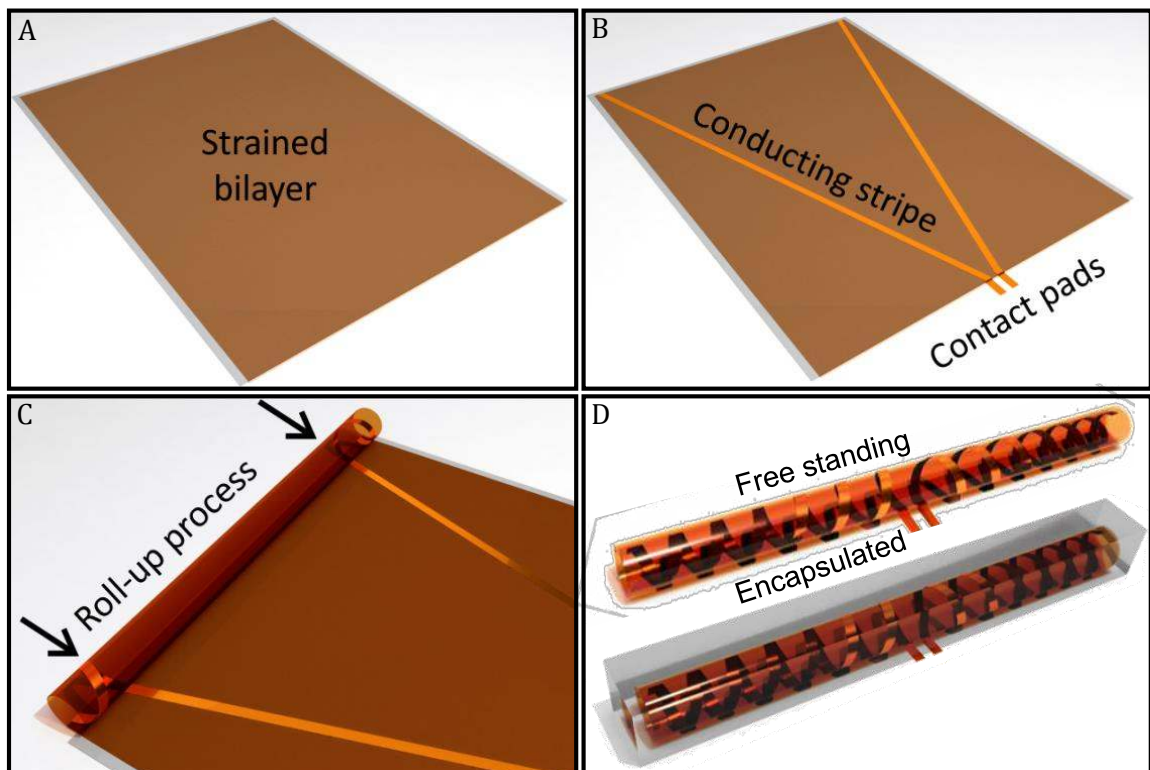


Figure 5.2: Fabrication process of self-assembled helical antennas. *A) Functional polymeric layers are applied and patterned on the substrate. B) The desired conductor pattern after the lift-off process. C) Self-assembling process of the antenna during selective etching of the SL. D) Free standing rolled-up helical antenna and an encapsulated version.*

The 2D layout shown in Figure 5.3a was considered and transformed into a Swiss roll-shaped tubular architecture (Figure 5.3b). An initial layout of the antenna consists of a 2 μm thick and 100 μm wide conducting wires. Vertical separation between windings is fixed to 2 μm , which is the typical thickness of the polymeric layers. The structure is prepared on a 1 mm thick glass substrate. All the geometrical parameters in the simulation are identical to those achieved in experiments except the thickness of the wire, which was defined as 100 nm for experiments and 2 μm for simulations to reduce load on the processing unit of FEM during meshing of geometries.

5 Results and Discussions

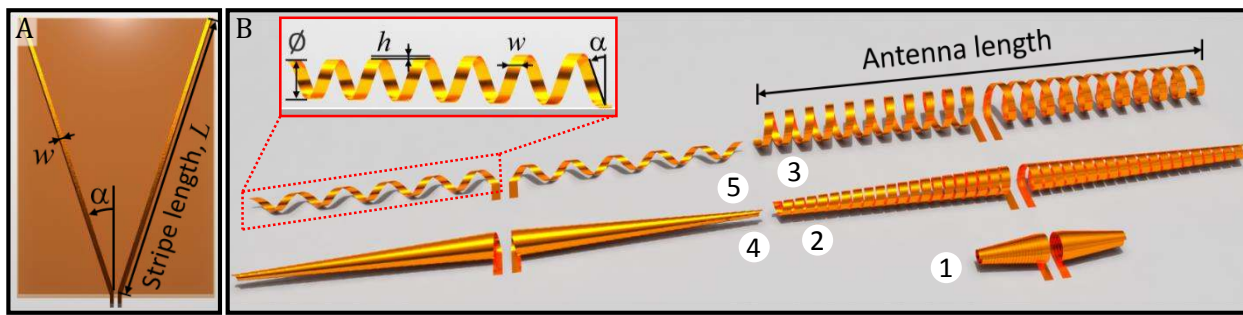


Figure 5.3: Model of the compact helical antenna. By tuning geometric parameters of the two-dimensional layout (a), helical antennas of different geometries can be achieved (b). (Image is adopted from [359])

To account for the difference in thicknesses, the conductivity of the simulated 2- μm thick metal layer was scaled down matching the conductivity of the experimental 100-nm thick Cu wire. With this adjustment, the total conductance of the antenna wire remains the same (Figure 5.4a), though, this approach is artificial, but allows the complete physical picture of the transmission properties of the antenna to be correctly captured without differences for the investigated frequency and only very small variation near 20 GHz could be observed (Figure 5.4b).

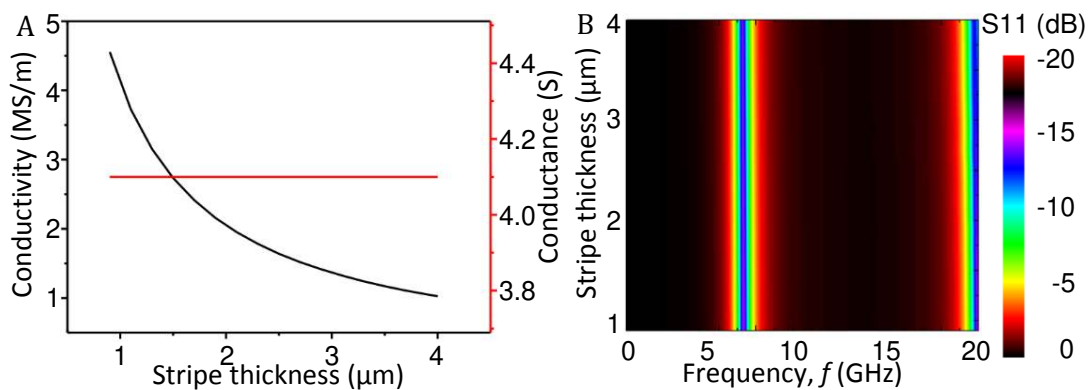


Figure 5.4: Resonance frequency as a function of the wire thickness respect to its conductivity. The conductivity is taken to be inversely proportional to the stripe thickness (A, black curve) to assure that the conductance corresponds to the 100 nm thick Cu wire. As the conductance is not changed with this adjustment, the resonance frequency remains unchanged (B). (Image is adopted from [359])

Impact of geometric parameters (Figure 5.3a), namely the inner diameter ϕ , the angle α and the stripe length L on the return loss of the antenna (S_{11} parameter) was investigated. The latter determines the efficiency of an antenna and is typically expressed in dB ($10 \log [P_{\text{incident}}/P_{\text{reflected}}]$). In this respect, antennas with $S_{11} < -10$ dB are classified as well transmitting antennas.

When the operation frequency f , and the inner diameter ϕ , of the antenna are fixed (as if only planar layout would be adjusted) the final length of the antenna could be determined through a parametric optimization of the angle α and the stripe length L using the S_{11} parameter (Figure 5.5a). The shaded region in the figure indicates the parameter space, where the length of helical antennas is smaller than 5.5 mm (the length of the smallest encapsulated ceramic antenna operating at 2.4 GHz). The optimization procedure considered successful whenever antennas in this region achieve S_{11} better than

-10 dB. The optimal antenna layout and length then could be determined from the dashed curve in the parametric space (L, α). For example, a set of antennas without an encapsulation, $\phi=160 \mu\text{m}$ and resonant frequency of $f=7.2 \text{ GHz}$ was simulated, and the result for (L, α) parameter space is illustrated on the Figure 5.5a. The resonance frequency of 7.2 GHz in free space is chosen for purpose that after an encapsulation of the antenna into a polymeric composite matrix with an appropriate permittivity, its resonance frequency should be reduced to $\sim 5.8 \text{ GHz}$. It could be seen from the figure that the region of interest is located between $15 \text{ mm} < L < 16 \text{ mm}$ and $8^\circ < \alpha < 11^\circ$ and satisfies the resonance condition ($S_{11} < -10 \text{ dB}$). From this simulation it could be concluded that the stripe length of $L=15.5 \text{ mm}$ should have an optimal value and is used for further investigations.

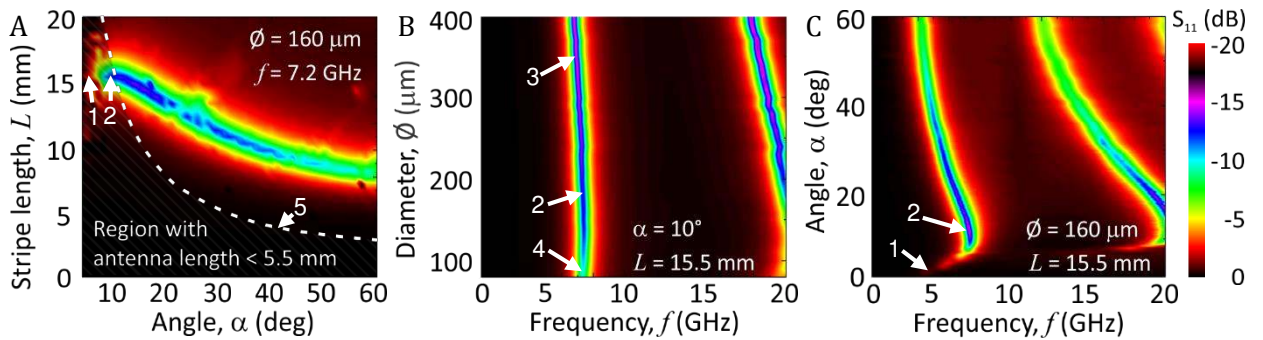


Figure 5.5: Parametric simulation of compact helical antenna characteristics. *Optimization of the antenna performance was performed by monitoring the effect of the relevant geometrical parameters, i.e., the stripe length (i), diameter (j) and opening angle (k), on the return loss of the antenna -the S_{11} parameter. (Image is adopted from [359])*

Interestingly, changes in inner diameter, ϕ , only moderately affects the performance of the helical antenna (Figure 5.5b). The antenna has two resonant peaks in frequency range up to 20 GHz, while the main peak of the interest is positioned at $\sim 7 \text{ GHz}$, and the second peak is observed at higher frequencies. Both resonant peaks reveal shifts toward larger frequencies when the diameter decreases. The shift of the main peak is rather small, which can be understood as follows: antennas of smaller diameter exhibit lower inductance. However, as the simulations are performed for the constant stripe length L , lowering of the diameter is accompanied by an increase in the number of windings in the structure. For instance, for the 5.5-mm long antenna with $L=15.5 \text{ mm}$ and intra winding spacing of $2 \mu\text{m}$ the number of windings in the helix may vary from 45 to 11 when the diameter is adjusted from 20 to $400 \mu\text{m}$ respectively (Figure 5.6a). If consider the helical antenna as a solenoid, these two effects lead to increase in inductance 80 times for bigger diameters of the structure. However, magnetic fluxes in two arms of helical antenna propagate in opposite directions, which is reflected in only a slight change of the resonant peak position (Figure 5.5b). Furthermore, we observe reduction in efficiency of the antenna with smaller diameter, which is mainly happening due to the onset of electromagnetic interaction among wires in neighboring windings when the period of the helix became comparable to the width of the wire. As will be discussed further, in this case, the strength of the emanated magnetic field outside the antenna is lowered, resulting in a reduced emission of the signal.

5 Results and Discussions

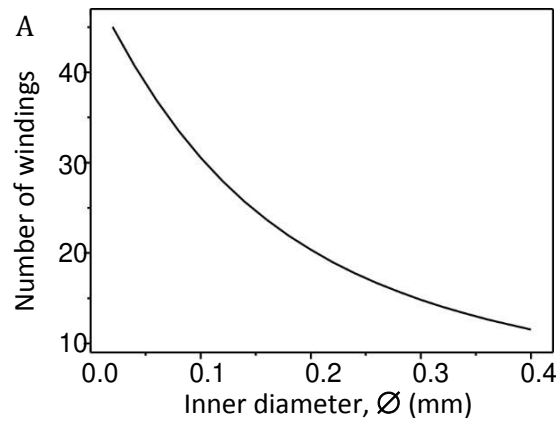


Figure 5.6: Number of windings versus tube diameter. When the stripe length L , spacing between windings and the final length of the helical antenna are fixed, the number of windings of the helix depends only on the inner diameter of the tube. For this calculation, were chosen $L = 15.5$ mm and inter-winding spacing of $2 \mu\text{m}$. (Image is adopted from [359])

Figure 5.5c summarizes return loss of helical antennas as a function of frequency f and angle α . The other two geometrical parameters are kept constant at $L=15.5$ mm and $\varnothing=160 \mu\text{m}$. For $\alpha > 8^\circ$, the antenna exhibits two resonant peaks. Positions of the two peaks depend on the angle α with a tendency to shift towards the lower frequency range with an increasing angle. Remarkably, a return loss of the antenna of up to -15 dB is achieved for $10^\circ < \alpha < 30^\circ$, indicating that the helical antenna can efficiently emit the signal. Interestingly, for $\alpha < 2.5^\circ$, there are no resonant peaks observed (Figure 5.5c). At small angles, the self-assembly process results in the formation of rather short antennas with laterally overlapping wires between neighboring windings (the pitch of the helix is smaller than the wire width). For the limiting case, $\alpha=0$, two coils are formed instead of helices (Figure 5.7a).

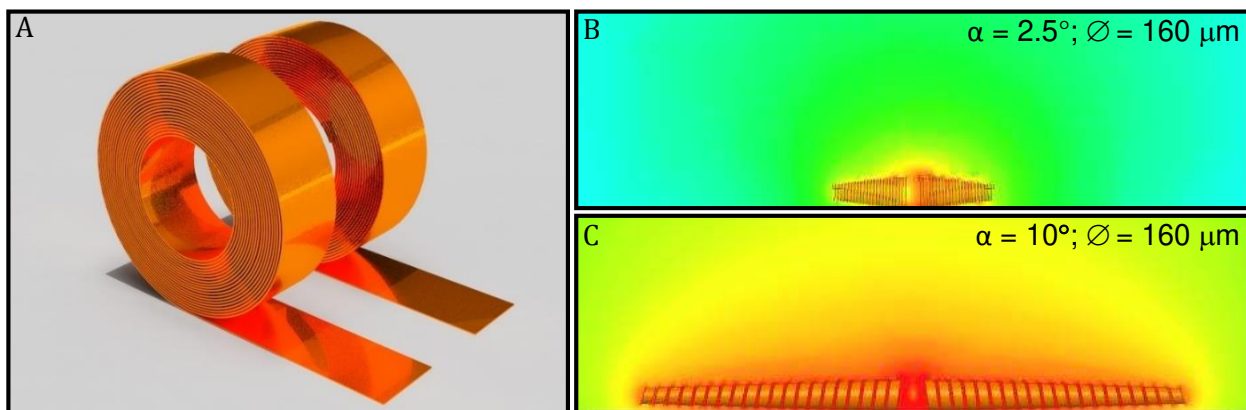


Figure 5.7: Distribution of the intensity of the magnetic field. A) When the opening angle is $\alpha = 0^\circ$, two coils are realized, instead of helices as shown in the Figure 5.3 of the main text. Such coils are not beneficial to enhance the performance of the rolled-up helical antenna and operate as a capacitor. The spatial distribution of the intensity of the emanated magnetic field outside the antenna is presented for the case of (B) a small and (C) larger opening angle α . (Image is adopted from [359])

Accounting for the opposite direction of propagating currents in both helices, the emanating magnetic fields will compensate each other. In this case, the mutual inductance cancels the self-inductance, and the antenna acts as a capacitor without transmitting the signal. The strength of the magnetic field outside the antenna is shown in Figure 5.7b and h for $\alpha=2.5^\circ$ and 10° , respectively.

The comparison reveals that a strong magnetic field (Figure 5.7c) and a good antenna performance (Figure 5.5c) can be achieved when the period of the helix is larger than the wire width. The performed simulations indicate that the optimal performance with $S_{11} \sim -15$ dB is expected for a normal mode helical antenna with a total length of 5.5 mm when the 2D layout is formed with $\alpha=10^\circ$ and $L=15.5$ mm. The realized helical antenna with an inner diameter of ~ 160 μm possesses a resonant frequency of ~ 7.2 GHz in free space (Figure 5.3b antenna #2).

The mechanical and electrical performance of helical antennas can be improved by an encapsulation in a polymeric matrix with a defined dielectric constant. The simulated return loss, the S_{11} parameter, for the chosen set of geometrical parameters of encapsulated antennas is shown on Figure 5.8 as a function of the frequency and permittivity, ϵ , of an encapsulation material. Here, the polymeric matrix effectively reduces antenna dimensions in comparison to the case of a free-space operating antenna at the resonance of 7.2 GHz. The encapsulation results in the monotonous decrease of the resonant frequency with a clear trend toward saturation at 5.6 GHz, which is already achieved for $\epsilon=10$. A further increase in permittivity of the encapsulating material does not affect too much location of the main resonant peak. From simulation it could be seen that the main resonance at 5.8 GHz could be achieved with dielectric constant around 4. Results from the simulation were used as input parameters for an experimental realization of the optimal antenna design.

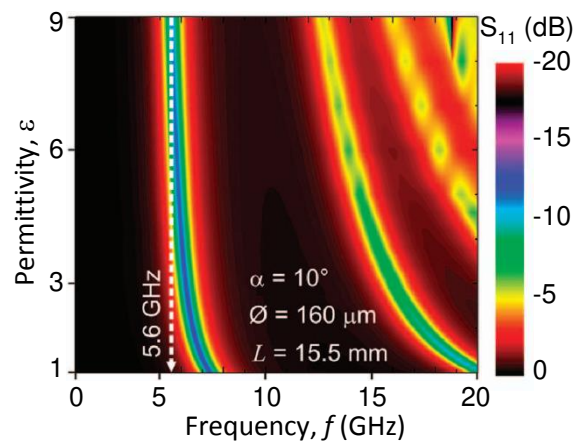


Figure 5.8: Influence of dielectric material on the resonance frequency. The simulated return loss of the antenna as a function of the frequency and the permittivity, ϵ , of the encapsulating material. For the simulation dielectric constants approximated from experimental results were used in the paragraph 5.2.8. (Image is adopted from ^[359])

5.1.3 Targeting in-vivo implant applications

Interesting directions in implantology are tooth and skin implant due to their simple integration possibilities and not deep location in the body. These applications require antenna to be in a human body surrounded by the tooth, bone and other tissues exhibiting complex losses. The lossy media affects characteristics of antenna compared to those operating in air. This important aspect was addressed in current section.

5 Results and Discussions

Extensive simulations of helical antenna characteristics were performed for the relevant cases. For these simulations, a simplified model of a human head was constructed with average dimensions of an adult person $19 \times 11 \times 24 \text{ cm}^3$ (Figure 5.9a) including teeth, bones, tongue, brain, and skin having relevant physical parameters assigned to each component of the model (Table 3). The model included a normal mode helical antenna with an inner diameter of $350 \text{ }\mu\text{m}$ encapsulated in a polymeric matrix resonating at frequency of 5.8 GHz in free space (Figure 5.9b). Embedded into a tooth, this antenna experiences a resonant frequency shift down to 2.45 GHz (Figure 5.9b). The strong resonance shift could be attributed to a bulky dielectric media surrounding the antenna, which consists of lossy biological tissues having high permittivity constants. The local environment around the antenna strongly affects its radiation characteristics, to show this, a series of simulations with the antenna implant was performed that was located under the skin and between the skin and a skull. Here, the standard three-layer model of a head was used. The discussion above remains qualitatively valid; however, there are quantitative differences observed, including a shift of the working frequency of the antenna even further to $\sim 2.2 \text{ GHz}$, which happens due to the higher permittivity of the skin and is also accompanied by an improvement of the S_{11} parameter (Figure 5.9b).

Table 3. Dielectric parameters for the human head model

Tissue	Permittivity	Conductivity (S/m)	Loss tangent	Density (kg/m^3)
Bulk skin	31	1.000	0.211	1080
Skull	14	0.465	0.26	1180
Muscle	53	1.760	0.25	1080
Brain	49	1.773	0.271	1000
Cerebellum	45	2.069	0.345	1000

This lowering of the operating frequency of the antenna to 2.45 GHz conveys strong advantages, namely (i) the 2.45 GHz frequency also belongs to the ISM radio band and hence appropriate for implant applications, and (ii) the absorption of electromagnetic waves in a human body is substantially reduced at 2.45 GHz compared with 5.8 GHz ; thus, a lower transmitter power can be potentially used. Furthermore, when targeting the operation frequency of 5.8 GHz and under skin application in the human body, the length of the normal mode helical antenna can be reduced even further from 5.5 mm to $\sim 2.5 \text{ mm}$.

The spatial distribution of electric field of the antenna is shown in Figure 5.9c. These data can be replotted as a radiation pattern (Figure 5.9d), indicating that the antenna radiates efficiently outside the body in the direction of the receiver with a gain of -46 dBi from the implantation depth of 33 mm . Using material parameters from the Table 3 and the equation for the attenuation constant from the paragraph 2.2.2 will be possible to find absorption loss of the material $L_{A(dB)} = 20 \log_{10} e^{\alpha d}$ equivalent to 8.6 dB . This gives approximated gain of the implanted helical antenna in the bulk skin as -37.4 dBi . Interestingly, the gain of the antenna in the direction towards the body is -65 dBi only, indicating strong attenuation of the signal, most likely due to absorption while the electromagnetic wave is travelling in the inhomogeneous lossy biological media of bones, skin and so on.

5.1 Modelling of the compact helical antenna

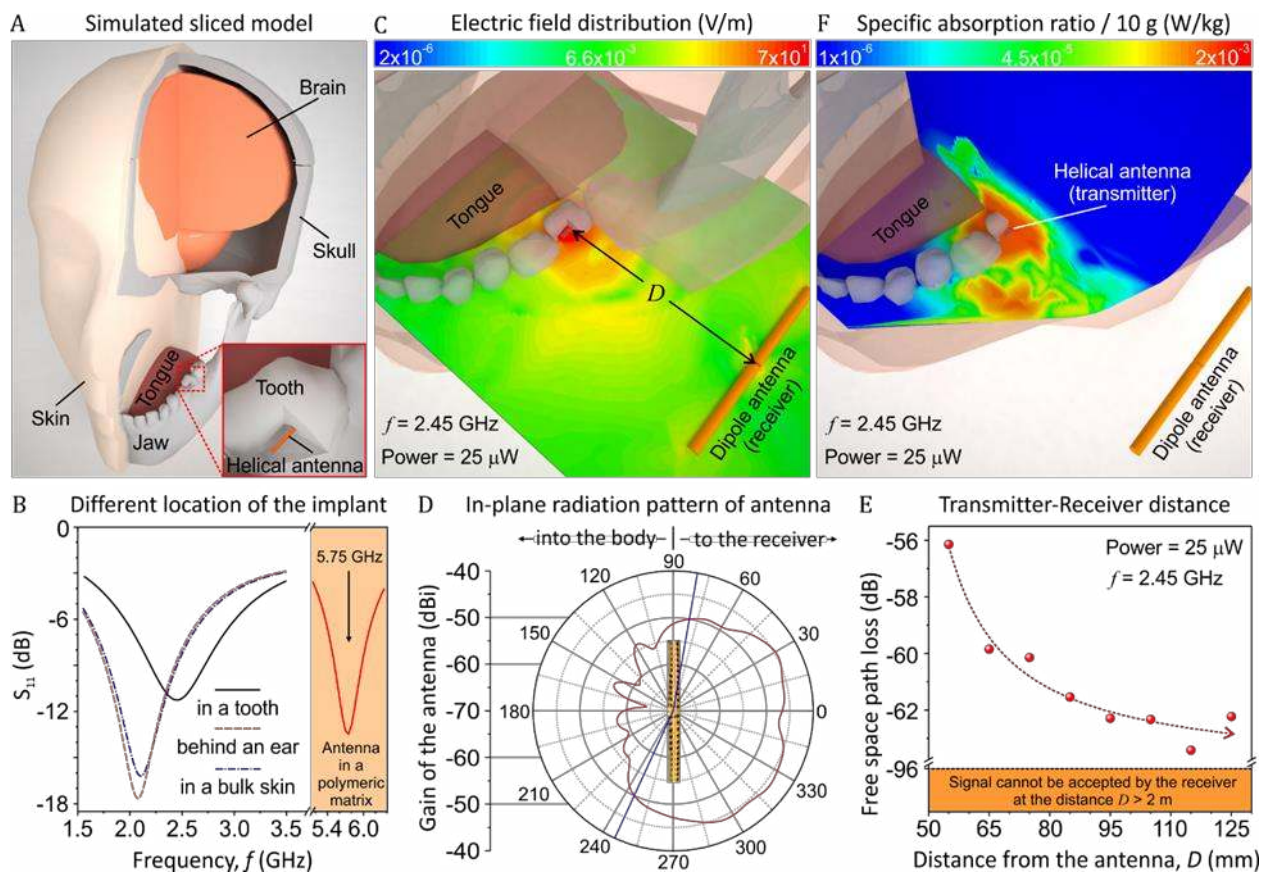


Figure 5.9: Targeting in vivo applications. *A) The human head model used for the simulations. The inset shows a close view of the helical antenna embedded into a tooth. Part of the model was removed for the good view. B) The frequency dependence of the S_{11} parameter for the helical antenna (diameter: $350\ \mu\text{m}$; encapsulated in a polymeric matrix) used as a tooth implant or implanted under the skin. The resonant frequency is shifted down to $2.45\ \text{GHz}$ for the tooth implant. C) The spatial distribution of the electric field of the antenna. D) The radiation pattern of the antenna (gain of the implanted antenna is plotted). The calculation was performed at $2.45\ \text{GHz}$. View from of the head. The blue line marks the minimum acceptable gain outside the human body. E) Simulated free space path loss of the signal transmitted by the antenna to the receiver as a function of the distance between transmitter and receiver. A dipole antenna is used as a receiver. F) Orthogonal cuts through the center of the helical antenna, revealing the spatial distribution of the specific absorption ratio calculated with respect to $10\ \text{g}$ of body tissue. The transmitting power of the helical antenna is $25\ \mu\text{W}$. The calculation was performed at $2.45\ \text{GHz}$. (Image is adopted from [359])*

The general trend of the signal attenuation for the near field with the increase of the distance between the helical antenna (transmitter) and dipolar antenna (receiver) is presented on the Figure 5.9e. The minimum gain of the antenna - G_{rx} can be derived from the Friis transmission equation: $P_{rx(\text{dB})} = P_{tx} + G_{tx} + G_{rx} + 20\log_{10}(\lambda/4\pi D)$. Relying on the gain - $G_{rx} = 2.15\ \text{dBi}$ of an external dipole antenna, the implanted transmitter power - $P_{tx} = -16\ \text{dBm}$ and accounting for a standard receiver minimum detectable power - $P_{rx} = -110\ \text{dBm}$ typical for mobile applications and desired transmission distance - $D = 2\ \text{m}$. A minimal gain - G_{tx} of the implanted antenna could be considered as $-50\ \text{dBi}$ (Figure 5.9d, marked as the blue line). At the same time this gives a very wide angle near 195° at which signal could be successfully transmitted, which mean maximum possible coverage for any possible daily movement of a person. The simulated normal mode helical antenna with a volume of $<5.5 \times 0.5 \times 0.5\ \text{mm}^3$ could be considered as suitable for a short-range communication, as needed for

5 Results and Discussions

smart implant applications, for example, communication with a smartphone, nowadays available near a user for a complete day. The achieved short-range operation represents the classical trade-off between the miniaturization of the antenna and its transmitting potential. For instance, a folded antenna with a ten times larger volume of $17.7 \times \varnothing 1.0 \text{ mm}^3$ can be used for communication at a distance of up to 20 m^[293]. As the helical antenna is designed for wireless implantable systems, it is imperative to consider the SAR for electromagnetic waves propagating in lossy biological tissues. SAR studies are performed for the antenna used as a tooth implant (Figure 5.9f). For these simulations, was assumed a transmitter power of $25 \mu\text{W}$ ^[293]. The simulations show that the SAR calculated with respect to 10 g of body tissue does not exceed 2 mW kg^{-1} , which is well within the limits of 2 W kg^{-1} imposed by the IEEE standard for safety levels with respect to human exposure to radio frequency electromagnetic Fields.^[70]

The realized normal mode helical antenna is designed to be impedance matched to 50Ω without relying on any external active or passive components. Therefore, the total footprint of the antenna of less than $5.5 \times 0.5 \text{ mm}^2$ corresponds to the size of the complete antenna element. With these geometrical parameters, this device is the smallest reported antenna that works at 5.8 GHz in air and is impedance matched to 50Ω , which is the most common impedance for microelectronic devices. To address the issue of compatibility with higher ohmic devices, additional simulation for the antenna performance were made when port impedance matched to 50, 75, 90 and 125 Ω (Figure 5.10).

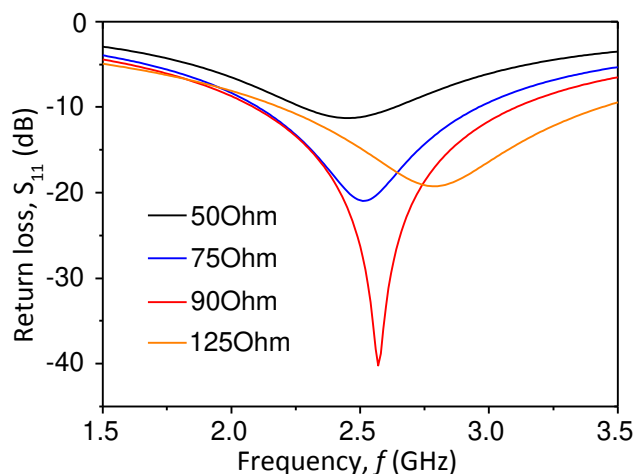


Figure 5.10: The S_{11} parameter of the helical antenna for different impedances. Data for the encapsulated helical antenna with the inner diameter of $350 \mu\text{m}$ embedded in a tooth of the complete model of a human head. The port impedances were set to accepted standard values of 50, 75, 90 and 125 Ohm. (Image is adopted from ^[359])

As it could be seen on the Figure 5.10, without changes of dimensions or geometry, the antenna appears to be matched to all these standard impedances, as it exhibits an S_{11} parameter better than -10 dB at resonant frequency. This possibility of being matched to these most standard impedances is of great advantage, as the same antenna can be used with different electronics without adjustments.

5.1.4 Self-assembly of helical antennas from the planar state

Self-assembly of a planar thin-film into a helical 3D geometry is a complex mechanical process that requires a precise control of the initial mechanical parameters and layouts of planar films. To determine the behavior of thin-films under various conditions having different layouts, a mechanical model of a multilayer thin-film structure was realized in the ANSYS Mechanics FEM software package (Figure 5.11) closely replicating a real experimental sample (Figure 2.8c).

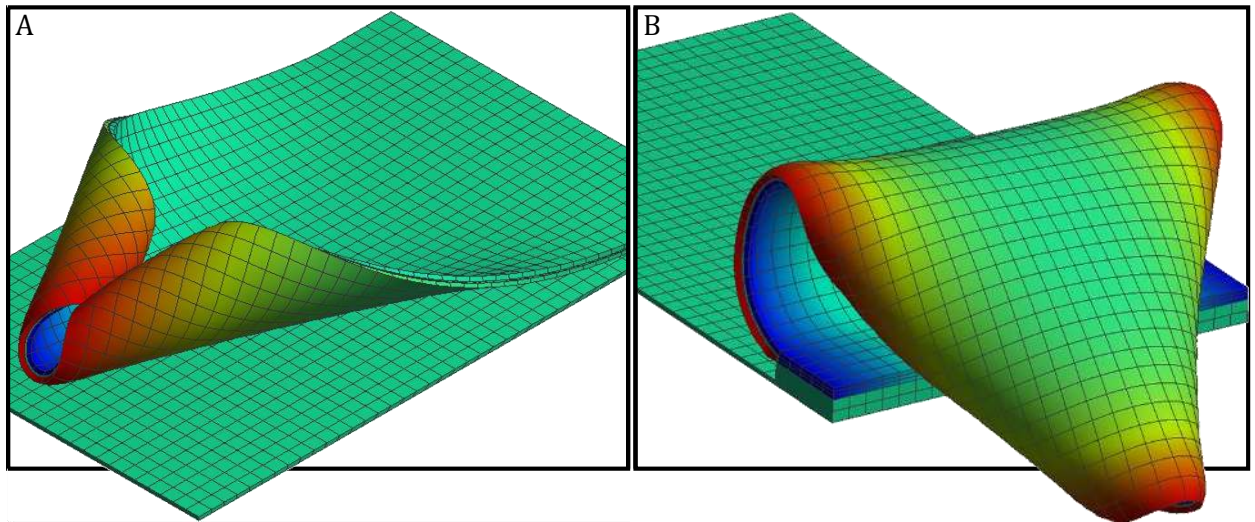


Figure 5.11: Typical failure modes in the self-assembly process for structures having big aspect ratios. Here etching edge propagates from one (A) and three sides (B).

Volumetric changes and the associated mechanical stress were simulated in the software package by thermal excitation of a suspended trilayer structure providing an appropriate stress configuration and the possibility to easily control different deformation scenarios occurring in real experimental structures. The coefficient of thermal expansion for both layers was defined as $10 \cdot 10^{-3} K^{-1}$ and the initial temperature was set to $0^\circ C$, where the layers system is present without stress. The top layer was cooled to $-20^\circ C$ in the model, to account for the residual stress equivalent to 45 MPa that occurs after the PI imidization process generating lateral contractive forces in this layer.^[384] Another thin layer with zero thermal conductivity was introduced between PI and HG layers to thermally isolate them. The other physical parameters of this isolation layer were taken as for PI. Etching of the SL was simulated by a front of heat propagating along one or several directions leading to an actuation of the planar layout. Two examples of such actuations, simulating an etching process from one and three sides are shown in Figure 5.11a,b, respectively. In both cases $30^\circ C$ and $-20^\circ C$ were applied at HG and polyimide layers, respectively, resulting in an assembly from edges and subsequent collapse of the structure. For the same aspect ratio, another simulation was done with additional structural modifications. The PI layer temperature was kept constant, while the HG layer was heated-up. A stabilization of rolling process was achieved with a block element introduced in the model at the front side and frictionless supports on left and right sides of the structure (Figure 5.12a). With one axis of

5 Results and Discussions

freedom in such a configuration, the solution results in a successfully assembled tubular 3D geometry. Figure 5.12b demonstrates geometries achieved by different thermal excitations applied at the HG layer, which could be realized in the real experiment by swelling of the HG in different solutions having various pH levels. In real experiments, such a stabilizing element needs to be introduced in the design of the planar structure.

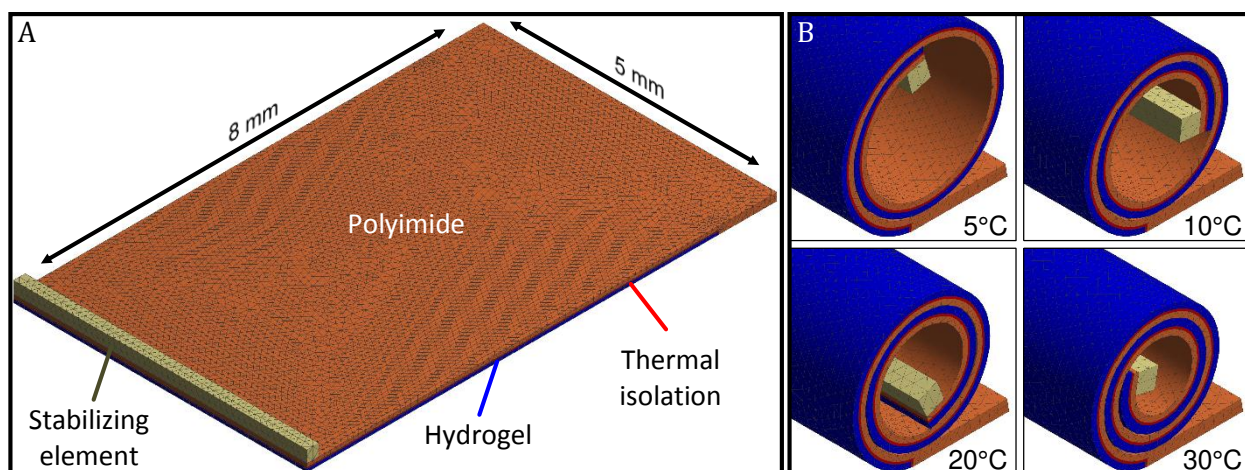


Figure 5.12: FEM model for the investigation of the self-assembling behaviour. A) Simplified model with an additional stabilizing element, which provides a stabilized way of a tubular structure assembly. B) Self-assembled tubular structures with applied different excitations to the HG layer.

Stoychev in his work experimentally investigated the rolling behaviour from the planar state into tubular structures depending on the aspect ratio between Length (L) and Width (W) of the planar structure, in relation to the final Circumference (C) of the rolled-up nanomembrane.^[385] In his work conclusions were made that rolling would occur only in that direction where the rolling length is bigger than C. Additionally, if $(L \approx W) \gg C$ rolling will appear from all directions, if $(L \text{ or } W) \ll C$ rolling will appear on the longest side and in the case when $(L \gg W)$ and $(W \leq C)$ rolling will dominate along the shortest side. In that work, tubular assemblies were obtained with a good yield in the range of aspect ratios of 4 and higher, keeping $W \leq 50 \mu\text{m}$. In the given case, the assembly was done along the shortest side with an aspect ratio of 3:1 between HG and inert layer with a final tube diameter of 20 μm . In the case, when the ratio between HG and inert layer was 1:1 a diagonal rolling was achieved giving tubes with 90 μm in diameter for $100 \leq W \leq 500 \mu\text{m}$. When values of L and W were significantly bigger than C, very defective rolling or rolling from all side occurs with no tube formation.

To overcome the rolling problem from left and right sides, conditions with different ratios L and W to C and with one side of the tube being connected to the substrate have been reproduced in the simulation. The results are presented in Figure 5.13a. When L or W is smaller than C, the tube has no rolling problems, but became unstable for both L and W equivalent to C or greater. To achieve a correct rolling process, one needs to artificially limit the aspect ratio of the planar structure locally. This could be achieved via specially designed structural elements (Figure 5.13b) introduced at sides of the

polyimide layer linking it to the substrate. The strong advantage of the side linking is a control of an assembly direction. The direction is defined by cut-off orientation of linkers, this could be however a bottle neck in overall self-assembly process leading to rolling defects and structural damages. To reveal possible problems additional simulations were performed.

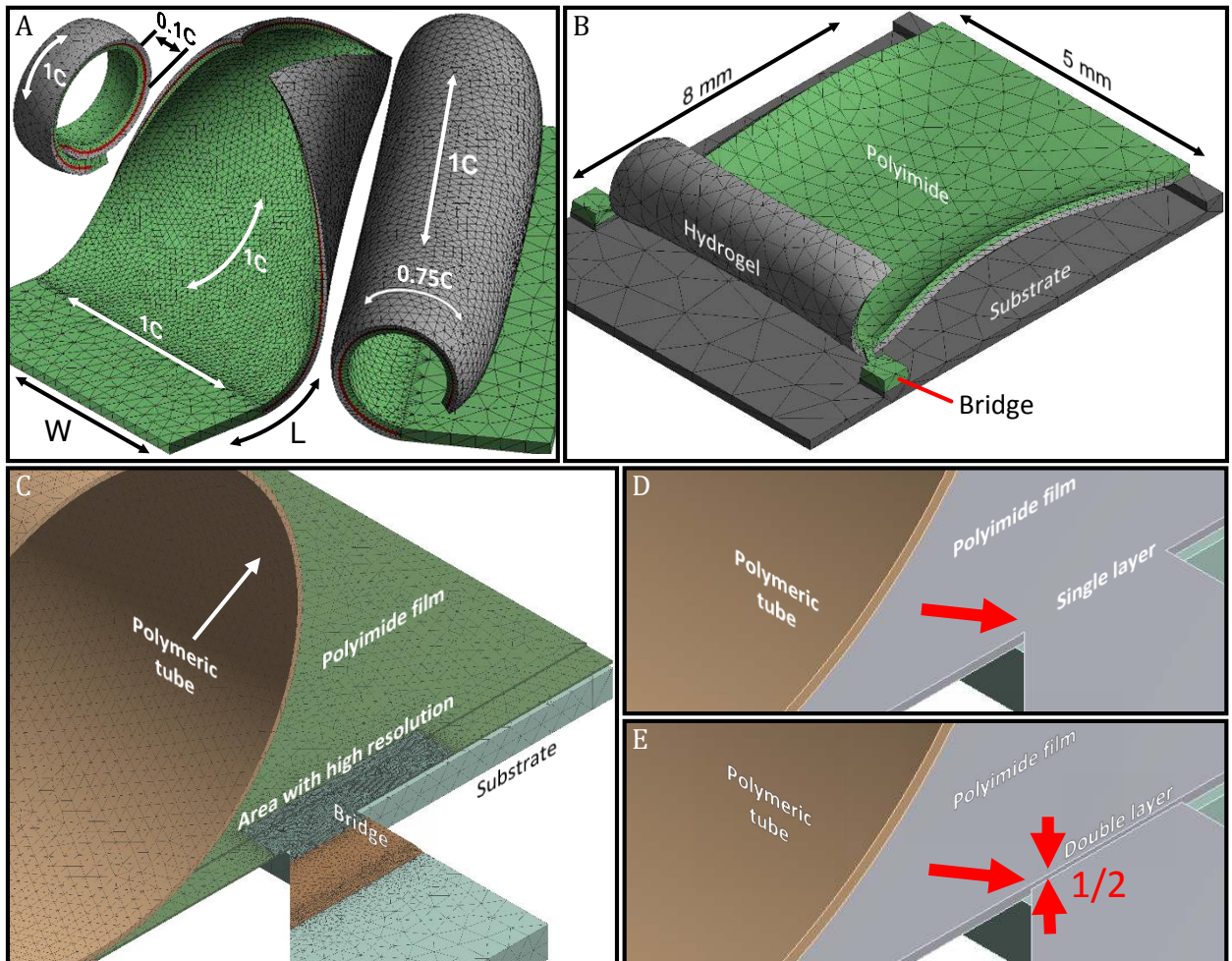


Figure 5.13: FEM model for the investigation of crack propagation behaviour. A) Models with different aspect ratios of L and W with respect to C . B) Planar structure with restricting elements for an artificial minimisation of the aspect ratio. C) Explicit model for investigation of crack formation and propagation over the linker. For simulations single (D) and double (E) PI layer configurations were used.

Investigation of crack formation and propagation through the linker structure was performed in an explicit simulation model. The geometry of the model was strongly simplified to perform simulations in a realistic time frame. However, in the single linker was introduced narrow element with the high-density mesh to minimise error during the calculation step at the area where the crack formation and propagation is expected (Figure 5.13c). In the simulation, linkers of two types were modelled having single (Figure 5.13d) and double (Figure 5.13e) layer polyimide layouts.

Figure 5.14a,b represents time frames when the crack begins to propagate through the linker. As it could be seen, the stress generated in the entire structure is significantly stronger in the single layer case (Figure 5.14a) in comparison to the two layer case (Figure 5.14b). The stress may affect the

5 Results and Discussions

assembly process as it leads to the deformation of the polymeric structure in the tube, eventually exceeding the yield strength of the materials involved. For the Figure 5.14a this moment has already happened and plastic deformation was introduced deeply into the layer, while for the case demonstrated on Figure 5.14b plastic deformation occurs only very close to the linker area. The crack forms at these highly stressed areas. For the single layer polyimide case, the crack propagates inside the structure in the direction equivalent to $\frac{1}{2}$ of the bridge entrance angle (Figure 5.14c). For the case when the length of the bridging element is longer, crack propagation inside the structure will have an even stronger character, until the structure fails completely. However, the double layer case effectively prevents penetration of the crack inside the structure (Figure 5.14b) independently on the bridge length resulting in a perfect cut exactly along the structure's edge. Real structures, however, exhibit misalignments and could contain non-ideal linker binding sites (Figure 5.15a,b), these non-idealities were also modeled (Figure 5.15c,d).

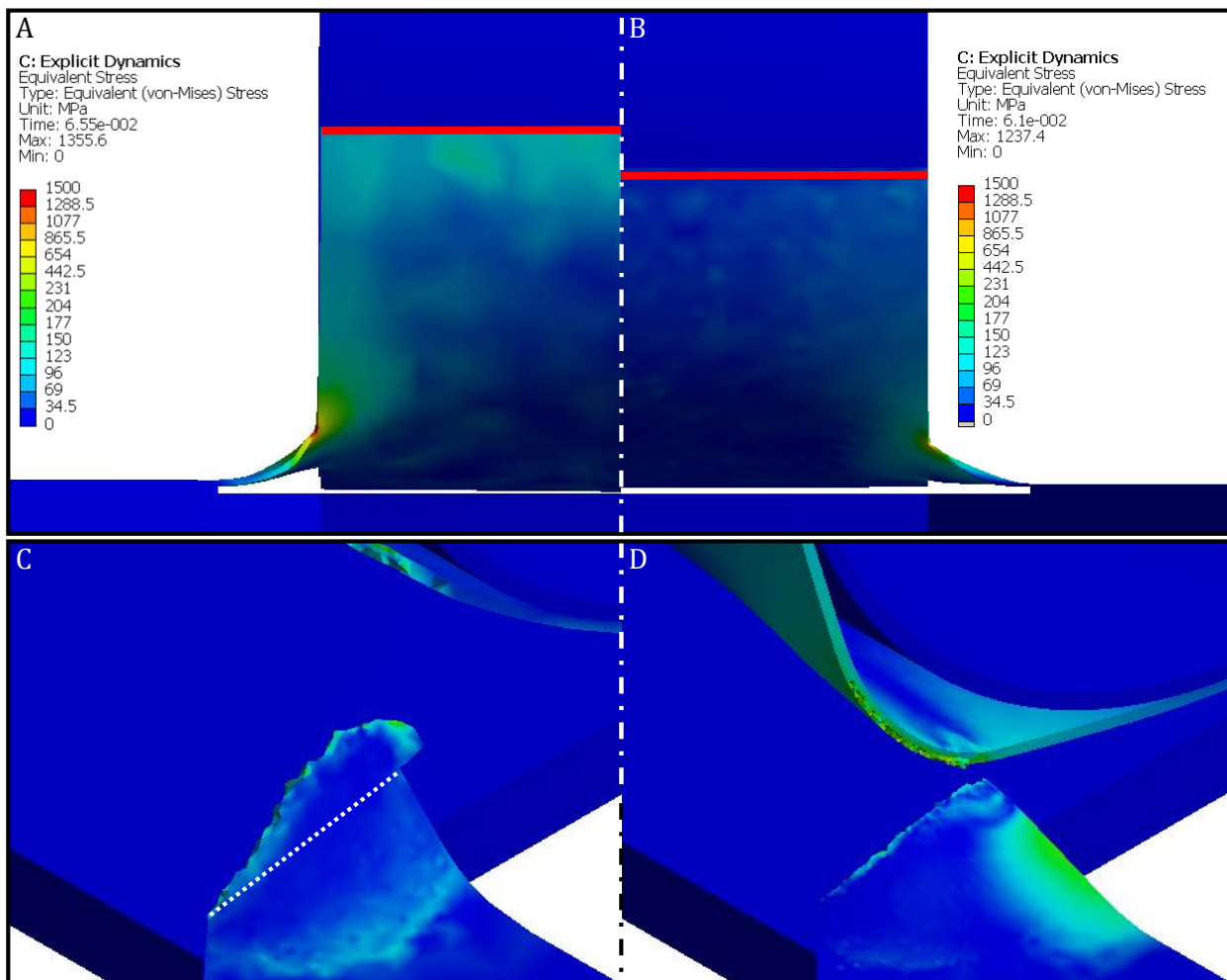


Figure 5.14: Comparative results between single and double layer structures. A and B) Timeframes taken exactly at the crack formation event (Back view). Crack propagation in the single layer (C) and the double layer (D) structures.

Figure 5.15c,d presents two frames just before the crack appearance and during its propagation, respectively. The crack forms and propagates from the entrance of the corner in the thin layer reaching the thick layer and continues its propagation along the edge until the end of the structure. This

simulation model reveals absolutely the same behavior as the respective experiment (Figure 5.15b,d). In some cases, cracks could propagate back to the outer edge like in a single layer structure (compare Figure 5.15a and Figure 5.14b) or could appear on the opposite side of the bridge. A secondary stress maximum occurs at the transition side between the SL and the substrate (Figure 5.15c). It is clear from the simulation that at this point an additional crack formation is may appear, when PI is thin. Shape and thickness of linker elements could be tuned to sustain stresses generated in the polyimide layer keeping the overall structure in the initial planar shape during the SL etching process and gradually realize the structure during the self-assembling process. An optimal thickness ratio of 1:2 between the bridging layer and the second PI layer was found experimentally.

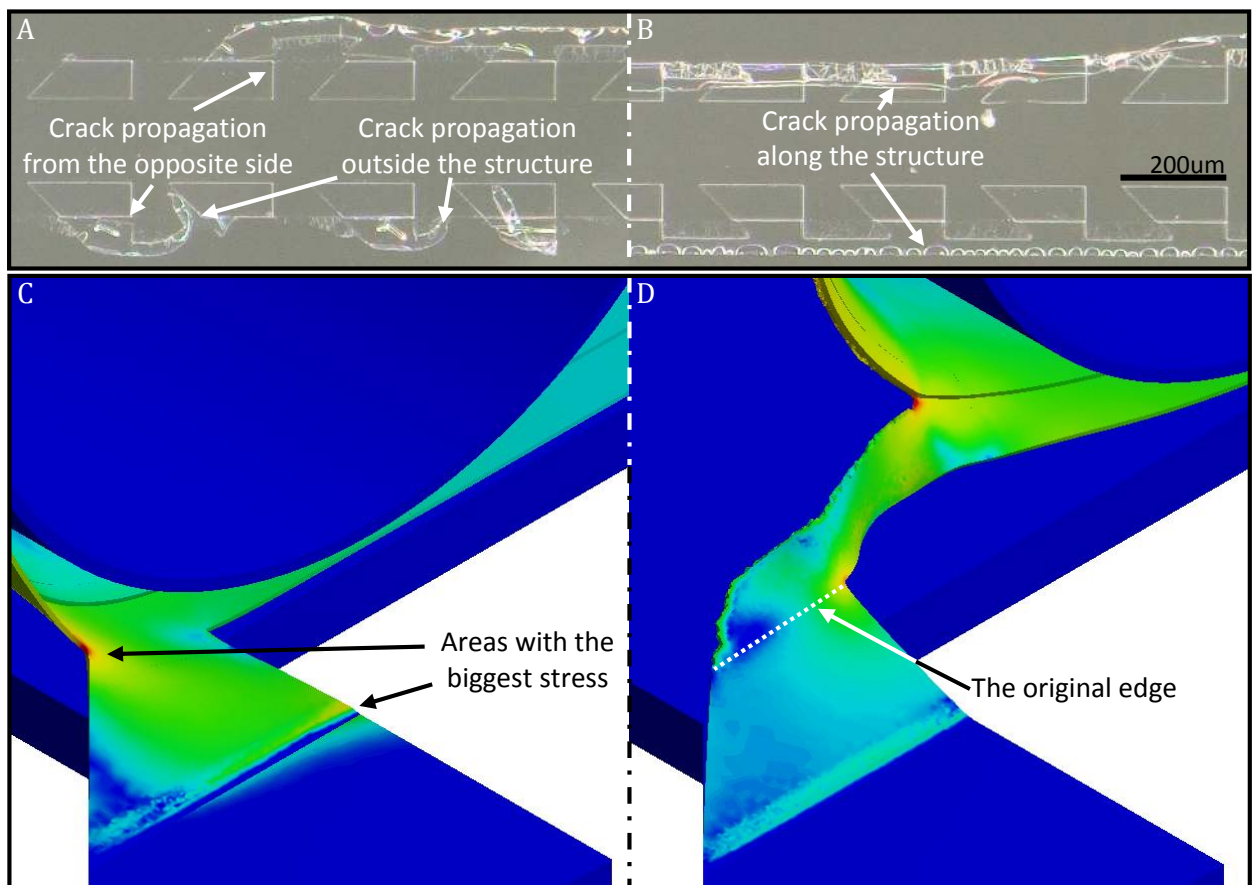


Figure 5.15: Linker braking behaviour in real experiments and simulations. A) Photo of linkers on the substrate after self-assembling process. White arrows pointing out similarities between simulation and experiment in the shape of broken linkers. B) Area with a potential back crack formation. Crack propagation along the edge of the missaligned structure. White dotted line marks the end of the bridge.

5.2 Experimental realization of compact helical antenna

Simulated and optimized antenna geometry was reproduced experimentally confirming mechanical and electrical characteristics of micro scale helical antennas. Fabrication steps of normal mode helical antennas are shown schematically on Figure 5.2. This process includes basic steps and additional intermediate steps e.g. substrate cleaning and adhesion improvement, fabrication of the SL and a mechanically active bilayer of HG and polyimide, photo lithographic definition of metallic electrodes of an antenna, and the final self-assembly of the planar geometry into a helical antenna. Then, antennas were encapsulated in a high-k dielectric material, reducing operational frequency. Afterwards, application as a tooth implant was demonstrated as well as injection into a polymeric matrix was performed simulating skin implantation in a close to biological environment. High yield fabrication and low spreading of antenna parameters pave the way for the cost-efficient fabrication and future commercialization of such implants realizing arrays of compact self-assembled antenna elements in a single process.

5.2.1 *Substrate cleaning*

Quadratic glass substrates with dimensions of 100x100 mm² and thickness of 1 mm (D263T eco glass, SCHOTT AG, Mainz, Germany) used in this work. Organic or inorganic contaminants, presented in a form of dust or film, were removed from the substrate surface by appropriate chemical and mechanical washing. First, all substrates were sonicated in an ultrasonic bath USC 1200 THD (VWR International GmbH, Darmstadt, Germany) for 5 min in acetone and isopropanol with a subsequent rinsing in deionized (DI) water. Then, substrates were sonicated for 60 minutes in a 2% solution of Alconox cleaner (Alconox Inc., New York, USA) in DI water at 60 °C and then rinsed thoroughly with DI water. Finally, substrates were washed in the solution containing 20 ml of 20% ammonia diluted in two liters of DI water under ultrasonic condition at 60 °C for 60 min and rinsed in DI water. Then substrates were stored in DI water preventing contamination and keeping surface in the hydrated state until the next process.

5.2.2 *Adhesion promotion of the glass surface*

For better adhesion of polymeric layers, surface of substrates was modified with self-assembled monolayers of 3-(trimethoxysilyl) propyl methacrylate (TMSPM). The process was performed in toluene (Sigma-Aldrich Chemie GmbH, Munich, Germany) solution of 1.5% (v/v) 3-(trimethoxysilyl) propyl methacrylate mixture for 20 min. Afterwards, the substrates were gently washed in a clean toluene, dried using nitrogen gas and baked on a hotplate PZ28-2 (Harry Gestigkeit GmbH, Düsseldorf, Germany) at 120 °C for 5 min under a nitrogen atmosphere to complete chemical reaction

between molecules and the glass surface. All the glasses are stored under vacuum before polymer processing steps.

5.2.3 Patterning of the sacrificial layer

The metal-organic polymeric SL was synthesized and patterned to form rectangular shaped islands (Subchapter 4.1). Solution of the polymer was spin coated with the following settings: polymer pre-spinning step was made at 500 rpm with acceleration 50 rpm/s for 10 s, main spinning is done at 3000 rpm for 30 s with acceleration of 500 rpm/s. Drying of the polymer was performed at 35 °C for 5 min on hotplate and followed by exposure in a mask aligner for 15 s through glass/Cr mask. The polymeric layer was developed by an immersion of exposed substrates into DI water for 15 s. Then substrates were washed in PGMEA (Sigma-Aldrich Chemie GmbH, Munich, Germany) to remove residuals of a water-insoluble photo initiator and annealed at 220°C for 5 min under nitrogen atmosphere removing rests of volatile molecules and hardening the layer. These patterns could be selectively etched away in water solutions containing chelating agents like diethylenetriaminepentaacetic acid (DETPA) or ethylenediaminetetraacetic acid (EDTA).

5.2.4 Patterning of the hydrogel layer

Three milliliters of the HG solution (Subchapter 4.2) was applied on the substrate through 1 µm syringe filter and then distributed over the surface using spin coating method using following parameters: polymer pre-spinning step was made at 500 rpm with acceleration 50 rpm/s for 10 s, main spinning is done at 3000 rpm for 30 s with acceleration of 500 rpm/s. The final post spinning step was done with acceleration of 2500 rpm/s for 3 s reaching >5000 rpm minimizing edge-beads. Then, to dry out remaining solvent from the HG layer, glass substrates were baked on the hotplate at 50 °C for 5 min. Exposure was done in the mask aligner through glass/Cr mask for 90 sec. Polymeric structures were obtained during development process in DEGMEE (Sigma-Aldrich Chemie GmbH, Munich, Germany) for 60 sec and washing in PGMEA for 5 sec. Then samples were annealed on the hot plate at 220°C for 5 min under nitrogen atmosphere. The thickness of resulted layer at the end of the process was around 700 nm.

5.2.5 Patterning of the polyimide layer

Polyamic acid precursor (Subchapter 4.3) in amount of 3 ml was applied on the substrate through 1 µm filter using following settings: polymer pre-spinning step was made at 500 rpm with acceleration 50 rpm/s for 10 s, main spinning is done at 2000 rpm for 30 s with acceleration of 500 rpm/s. The final post spinning step was done with acceleration of 2500 rpm/s for 3 s reaching 5000 rpm minimizing edge-beads. Then, to dry out remaining solvent the polymeric layer was baked on the

5 Results and Discussions

hotplate at 50 °C for 10 min. Exposure was done through glass/Cr mask in the mask aligner for 90 sec. Development of the exposed layer was done in the solution of solvents: 40 ml of NEP (Sigma-Aldrich Chemie GmbH), 20 ml of DEGMEE and 10 ml of ethanol (VWR International GmbH) for 90 sec with a subsequent washing in PGMEA for 5 sec. Afterwards, samples were annealed on the hot plate at 220 °C for 10 min under nitrogen atmosphere in order convert polyamic acid precursor into polyimide making the layer thermally and chemically stable. Figure 5.16a shows a sample after the polymer patterning process. The sample contain SL, HG, PI and patterned photoresist layers. Photoresist processing described in the following discussion. On the Figure 5.16b it is noticeable that the step between surfaces of the substrate and the polyimide layer has very smooth edge which should possess a uniform transition along metallic conductor reducing resistance, eliminating cracks and an overall RF contact loss.

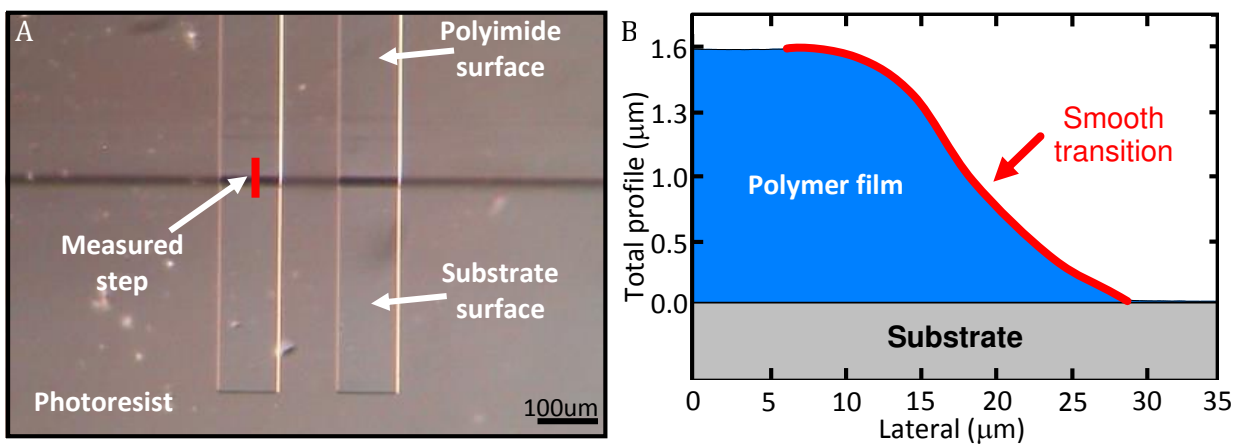


Figure 5.16: A sample after the polymer patterning process. A) Photolithographically patterned polymers and a photoresist layer. Red line marks the position of the measured profile at the PI edge. B) Profile of the PI edge reveals very smooth transition between the substrate surface and the top of the PI film. (Image is adopted from ^[359])

5.2.6 Structuring of metal electrodes

The antenna conductors were formed in a lift-off process using a double layer photoresist technology. The thick positive photo chemically amplified AZ40XT (Microchemicals GmbH) photoresists and the non-photosensitive polyamic acid precursor (Subchapter 4.4) were used for this process. Three ml of polyamic acid applied on the sample surface through 1 μm syringe filter (Figure 5.17a) via spin coating process using following parameters: polymer pre-spinning step was made at 500 rpm with acceleration 50 rpm/s for 10 s, main spinning is done at 3000 rpm for 30 s with acceleration of 500 rpm/s. The final post spinning step was done with acceleration of 2500 rpm/s for 3 s reaching 5000 rpm minimizing edge-beads. A soft-bake was done on the hotplate at 120 °C for 2 min to remove solvent and partially isoimidize the layer of polyamic acid. This process lowers etching rate enhancing control over the lift-off process. Then 100 x 100 mm² substrates were divided into four 50 x 50 mm² pieces. The photoresist AZ40XT was subsequently applied on the substrate using the same parameters as for polyamic acid layer (Figure 5.17b) and soft-baked on the hotplate for 4 min

5.2 Experimental realization of compact helical antenna

at 120 °C. The sample was exposed in the mask aligner through glass/Cr mask using UV band pass filter centered at 365 nm with the radiation power density of 8 mw/cm² for 60 s (Figure 5.17c). Then the photoresist was post-baked on the hotplate for 6 min at 115 °C.

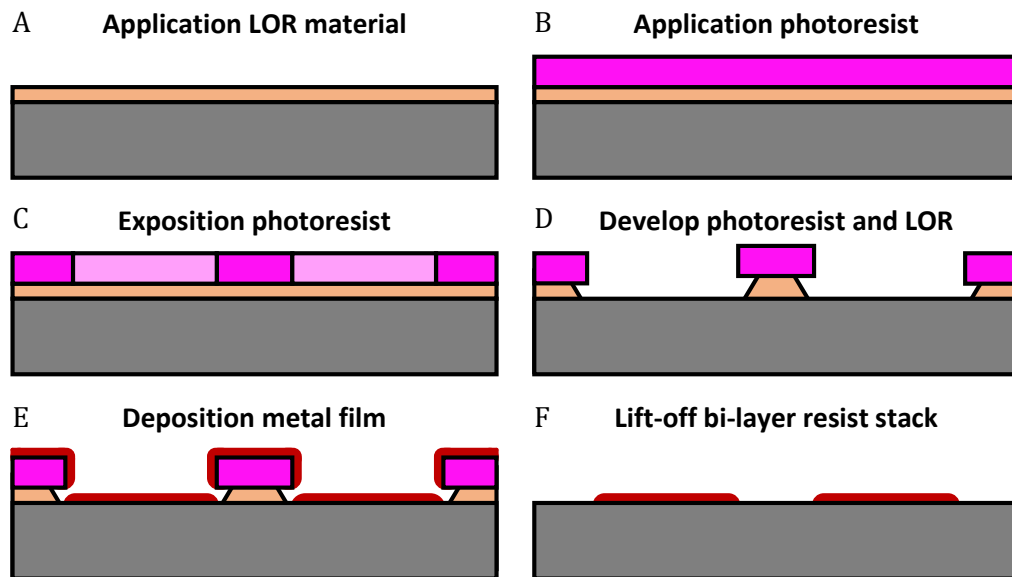


Figure 5.17: Double layer photolithographic process. A) Spin-coating and baking of LOR resist. B) Spin coat and bake of photoresist layer. C) Exposure of the photoresist through a glass/Cr mask. D) Developing photoresist and isotropic etching of the LOR resist. E) Deposition of Ta/Cu/Ta and Au films. F) Lift-off of bi-layer resist stack and removal of undesired metallic films.

Photoresist patterns were developed in MIF726 developer for 3 min with active agitation. When exposed areas of the photoresist are completely developed, MIF726 developer starts to isotropically etch the isoimidized first layer (Figure 5.17d). Every 5 sec the length of the etching profile was visually controlled through microscope until reaching a desired value of 20 μm . The etching process is shown on the Figure 5.18a-c demonstrating a good control on the process. A subsequent washing with DI water, blow and 50 °C for 5 min hot plate drying was necessary to remove all the remaining water under the photoresist gap before metal deposition.

Metal layer stack (Figure 5.17e) consisting of Ta(10 nm)/Cu(100 nm)/Ta(10 nm) was deposited using magnetron sputtering at room temperature (Ar was used as a sputter gas at partial pressure of 10^{-3} mbar; base pressure in the chamber was better than 10^{-7} mbar). Stability of the electrical contact was improved, and associated contact noise was removed by an additional layer of Au (100 nm), which was deposited using E-beam evaporation. The lift-off process was done by swelling and dissolution of the photoresist in acetone removing unnecessary metal from the surface. The isoimide was stripped away with the MIF726 developer. As a result, pattern of the photoresist was transferred on the sample surface leaving desired metal structures (Figure 5.17f). For better radiation efficiency of the antenna the thickness of the copper layer was increased up to 1.6 μm in the metal stack, but long deposition of very thick layers results in a deep over coatings as it could be seen on Figure 5.18d,e, and extra width of conductors must be taken into account in the design.

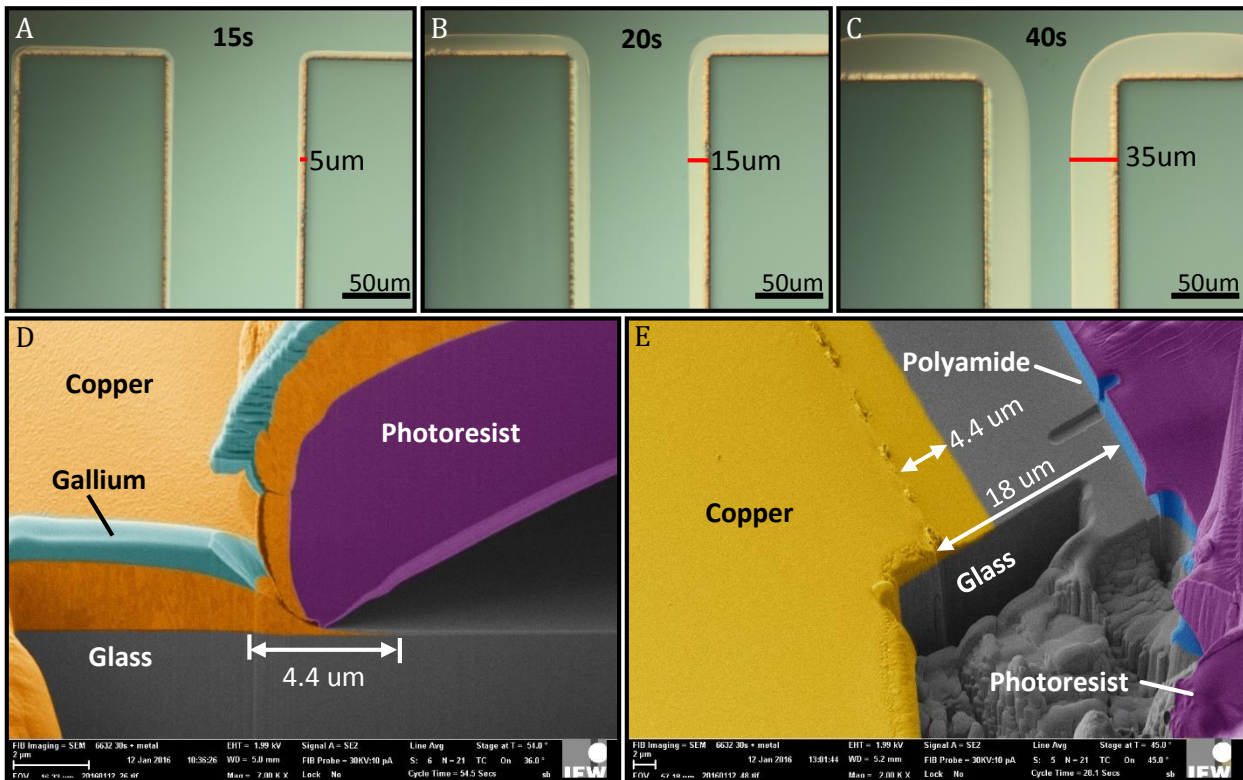


Figure 5.18: Sample after the bi-layer photolithographic process. (A – C) Etching process of the isoimidized layer under the photoresist layer with respect to etching time. After the metal film deposition (D, E) cross sectional images of the bi-layer photoresist stack were obtained using a SEM-FIB cross-beam tool to control under deposited material and adjust photoresist developing time accordingly.

5.2.7 Self-assembly process

After all the planar processing’s 2D layouts were self-assembled into 3D helical antennas by a selective etching of the SL in the solution of a strong chelating agent containing 15 g of DETPA (Alfa Aesar, UK) in 500 ml of DI water and a subsequent swelling of the HG. The chelating agent was required to uncrosslink SL by absorption of the lanthanum ions from the PAA-La 3D network. The solution of the chelator was prepared by neutralization of DETPA with sodium hydroxide in an amount sufficient for complete dissolution of DETPA powder and reach pH of up to 8. Etching of the SL was achieved in 100 ml of the DETPA solution, pH of which was adjusted with 37% of hydrochloric acid (HCl) (Alfa Aesar, UK) to the value of 5.5, this value of pH prevents swelling of the HG and bending of the functional bilayer, thus keeping linkers between the substrate and the structure unbroken. The pH of the etching solution has to be kept above or close to $pK_a = 4.5$ ^[386,387] of PAA, to keep the most of carboxylic acid functional groups in deprotonated hydrophilic form letting it to dissolve when La^{3+} ions are acquired by the DETPA, at the same time La^{3+} ions are kept in the non-hydrolysed water soluble form. During this process, La^{3+} ions exchanges with Na^+ ions altering the state of the SL from its three-dimensionally lanthanum cross-linked form to the linear water-soluble sodium PAA. Additionally, HCl works as a catalyst, which brakes anhydrides in the HG and SL

5.2 Experimental realization of compact helical antenna

producing acyl halides as by-products which rapidly decompose to carboxylic acids as final products in water solution. This process significantly reduces etching time from 6 hours down to 1.5 hour.

When the SL completely dissolved the sample is immersed into the clean DETPA solution having pH 8 to initiate the rolling process and remove residuals of lanthanum. During the self-assembling process some of the tubes could have roll out of longitudinal direction. In this case, assembled structures will be miss aligned at edges. To eliminate this problem a special device (Figure 5.19a) was constructed and applied for guidance of the self-assembly process achieving a high fabrication yield. For rolling using this setup, samples allocated in a dish and guiding glass piece placed above structures (Figure 5.19b). When the dish filled with the solution, rolling process is blocked by the glass. Then the glass piece can be moved in the direction of rolling allowing a homogeneous aligned assembly of structures. This process could be easily scaled-up by increasing of the guiding glass size.

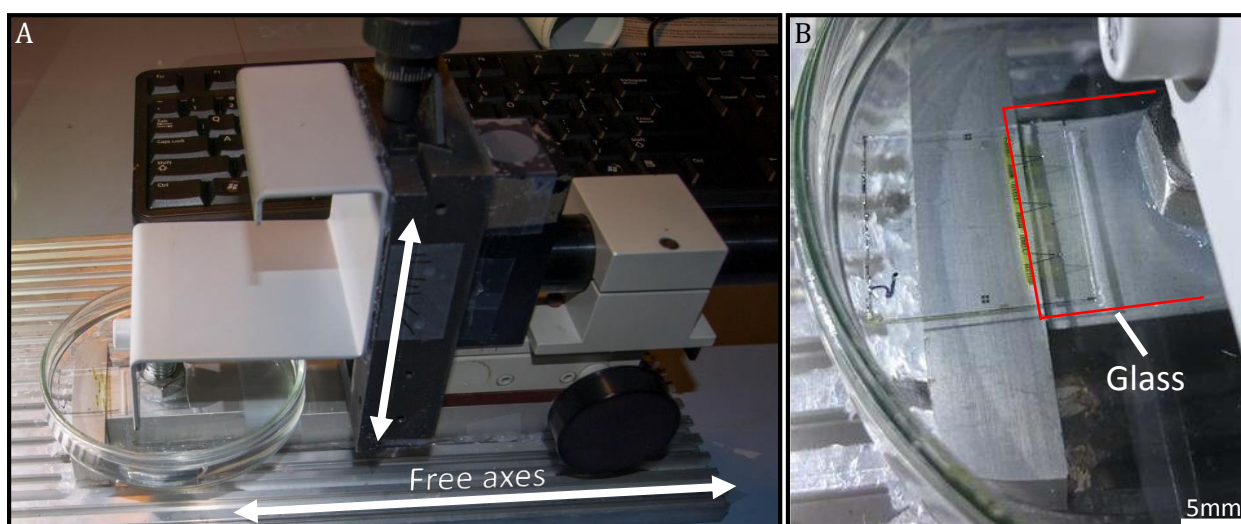


Figure 5.19: Set-up developed for assisting the self-assembly process. A) Tool for assisted rolling. B) The sample guided by the glass edge during self-assembly process. Red line marks the guiding glass.

To accomplish the self-assembly processes and completely swell the HG layer, antennas were left in the rolling solution for an hour obtaining their final shapes. Diameter of antennas could be adjusted by pH variation of the rolling solution. This method is useful during the fine-tuning of antenna resonances without the need in fabrication of new samples. Finally, substrates and antennas were then washed using a solution of DI water and isopropanol mixed in a proportion of 3:1 respectively with a subsequent drying on air. Isopropanol in washing solution reduces surface tension up to three times,^[388] additionally intensifying the drying process and increasing the total yield of tubular geometries to almost 100 %. Here, it is necessary to mention a key point and an outstanding property of developed polymeric materials. Achieved 3D architectures are mechanically stable and could be directly withdrawn from the liquid and then dried at ambient conditions without the use of a special equipment i.e. super-critical or freeze-drying. Figure 5.20 demonstrates achieved antennas having various helical geometries of conductors. Figure 5.20a shows tubular structures with 600 μm in

5 Results and Discussions

diameter that were assembled on a single substrate. Quality monitoring over 48th self-assembled helical antennas prepared in a single run on the 100x100 mm² substrate provides a possibility to quantify the fabrication yield as good as hundred percent.

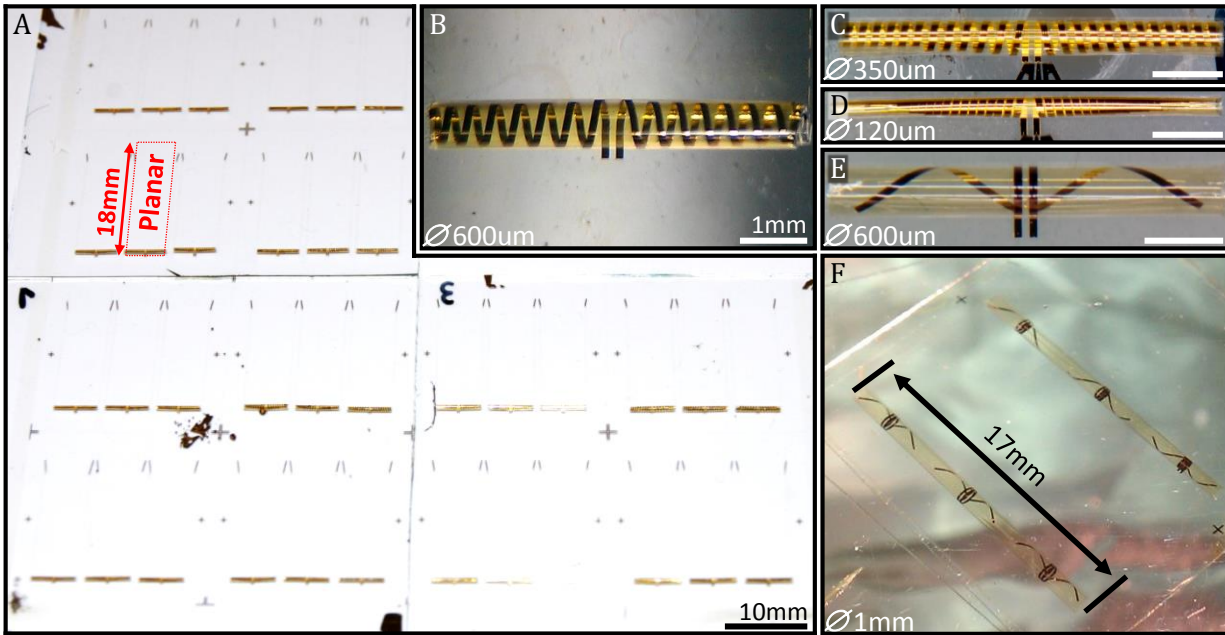


Figure 5.20: Experimental realization of helical antennas. A) Optical micrograph revealing a regular array of rolled-up structures with metallization assembled from planar structures having a length of 18 mm. The length of each tubular object is 5.5 mm. B, C and D) Tubes with different diameters could be achieved by tuning the pH level of the rolling solution. E) By varying the 2D layout before the self-assembly process, different geometries of individual antennas, as well as antenna arrays (F), can be fabricated. Scale bars on C – E images are 1 mm. (Images C – F were adopted from ^[359])

However, for a good reproducibility of diameters, it is necessary to keep spreading of functional layer thicknesses and pH level of the rolling solution at a very narrow window. pH tuning of the solution could be varied to get 5.5 mm long Swiss rolls of different diameters ranging from 80 to 600 µm with 7 – 40 windings (Figure 5.20b,c,d). High yield fabrication and outstanding stability of the polymeric platform opens new possibilities of generating variously sized rolls having different layouts in a planar state as demonstrated on the Figure 5.20e. A number of devices could be achieved in a single self-assembly process forming a 2D helical antenna array (Figure 5.20f) that can potentially function as a metamaterial in a microwave region in the spirit of recent works i.e. by Slobozhanyuk.^[389] All the rolled-up architectures were fabricated on quadratic glass substrates with areas of 100 × 100 mm², however larger dimensions were limited by the maximum working area of the available mask aligner (SUSS MA45) possessing a potential up-scaling.

5.2.8 Encapsulation of antennas

Fabricated antennas were then encapsulated into a polymeric matrix to enhance mechanical stability of the 3D architectures and to shift the resonant frequency of the rolled-up antennas to lower frequency band. For encapsulation, the tubular architectures were processed as follows. Firstly, the

dissolvable frame around the antenna was prepared (the frame solution is described in the chapter 4.5). When the region was determined by the frame (Figure 5.21b), an interior area was filled with the encapsulation solution consisting of functionalized BaTiO₃ mixed with the UV sensitive organic binder (Figure 5.21c). After curing of the encapsulation solution, sample was transferred to the aqueous ammonia solution, where the frame was removed (Figure 5.21d).

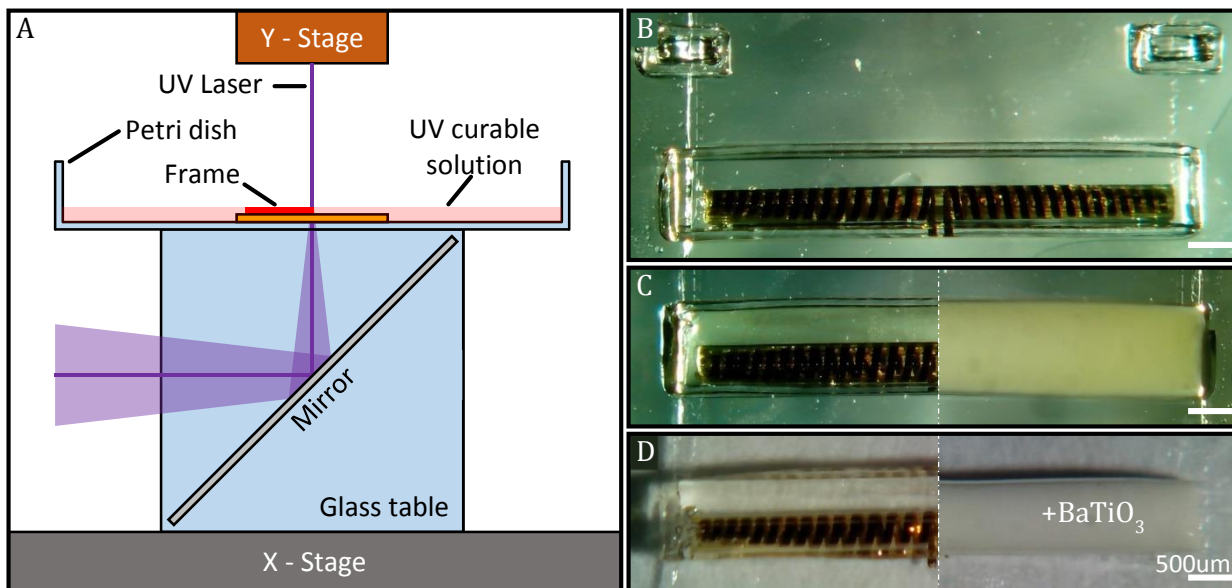


Figure 5.21: Antenna encapsulation process. A) Schematic representation of the direct laser writing device for fabrication of a frame around the antenna. B) Photo of the antenna surrounded by the frame. C) Antenna filled with clean (left) and mixed with dielectric material (right) encapsulation solutions respectively D) Encapsulated antennas with already removed frame releasing electrodes for characterization.

The frame was formed by exposure of the frame-solution using a direct laser writing method. The 8 mW-UV 376 nm laser from Coherent (Coherent LaserSystems GmbH & Co. KG, Hannover, Germany) was installed in a 3-axial robot (Fisnar F7300N, Fisnar Europe, Glasgow, UK). For this, the sample was placed in the Petri dish and filled with the frame solution covering antenna structures. Then, the glass with the solution and the sample were placed on a glass frame where a mirror was installed at 45° to minimize backscattered light (Figure 5.21a). For the curing process of the UV sensitive framing material, the scanning speed of the laser, along preprogrammed path, was set to 1 mm·s⁻¹. At the end of the direct writing process, the sample was washed in acetone, resulting in the frame around the antenna. The volume surrounded by the frame was then filled with the encapsulation solution (described in the chapter 4.6) the solution was then photo polymerized and the frame dissolved in an ammonia solution at pH 10 for 10 min with a subsequent rinsing in DI water and drying.

Before antenna encapsulation, dielectric permittivity of the cured material was measured. First, the encapsulation solution was applied between two 1 mm thick Teflon sheets and exposed for 20 s by a high intensity blue LED with a wavelength of 450 nm (100 W; 150 mW/cm² at a 10 cm distance). Then cross-linked polymeric foil was peeled from the Teflon surface and cut by a punch tool into 10 disks with 10-mm diameters. The averaged thickness of the disks in a value of 173±5 μm and

5 Results and Discussions

180±5 μm, for clean and filled encapsulation materials respectively, was measured over 10 samples by a micrometer screw gauge. A dielectric constant of the material was determined through capacitance measurement of the capacitor formed by placing each dielectric disc between polished aluminum cylinders of the same diameter. Capacitance measurements were performed at frequencies ranging from 100 Hz to 2 MHz using an Agilent E4980 precise LCR meter (Agilent Technologies Deutschland GmbH, Waldbronn, Germany), the averaged capacitance for clean and filled with BaTiO₃ dielectric materials are presented on the Figure 5.22a. The values vary from 20.5 pF and 58 pF to 16.64 pF and 19.83 pF from lowest to the highest frequencies respectively. The permittivity of the dielectric material was calculated from capacitance of the capacitor using the equation $C = \epsilon\epsilon_0 \frac{S}{d}$.

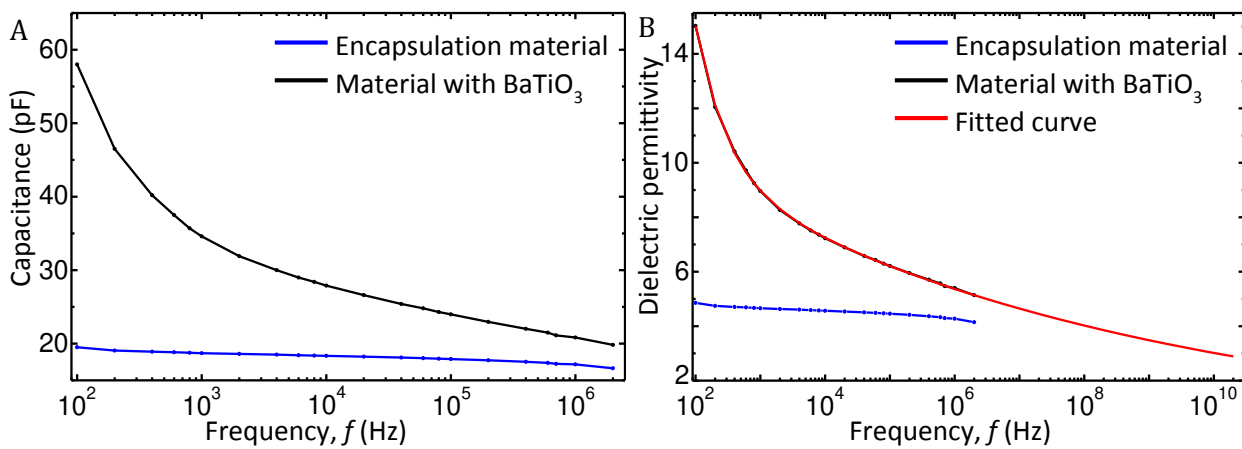


Figure 5.22: Parameters of the encapsulation solution. A) Capacitance of the capacitor formed by two metal cylinders and encapsulation material between them. B) Permittivity of the material versus frequency, calculated from the capacitance.

As it could be seen from the Figure 5.22b, the dielectric constant measured at lower frequencies for clean encapsulation solution is 3.86 and for filled version is 15. These values rapidly decrease at 2 MHz accounting for 3.95 and 4.87 respectively. The dielectric constant of the BaTiO₃ filled material was interpolated and used in simulations at the frequency range from 1 GHz to 20 GHz, where it has values ranging from 3.5 down to 2.0 respectively.

5.3 Characterisation of compact helical antennas

5.3.1 Return loss

All prepared antennas were characterized acquiring their S_{11} and S_{12} parameters using the Cascade PM-8 probe station and vector network analyzer Agilent E5071 (Agilent Technologies GmbH & Co.KG, Waldbronn, Germany) in the frequency range from 300 kHz to 20 GHz. All the electrical connections with antennas were made using ground signal ground (GSG) CASCADE |Z|-probes. To eliminate coupling effects due to the reactive near field of the antenna and the metallic chuck of the probe station, all the experiments were performed on a 20 mm thick PTFE block. Figure 5.23 shows dependence of return loss of antennas having diameters between 100 μm and 600 μm . As it could be seen, positions of the resonances are close to the simulated results (Figure 5.5b). The main resonance of antennas with diameters near 350 μm is located at 6.9 GHz (Figure 5.23b), where dash line represents simulated antennas with equivalent geometrical parameters. While the antennas of smaller diameters possess higher resonance frequency. Figure 5.23c present measurements of 12 antennas having diameters around 600 μm , arbitrarily chosen from the array fabricated on one quarter piece of the substrate. This figure demonstrates a good yield and reproducibility of antenna characteristics. Due to small non-uniformities in the beginning of the assembling process antennas exhibit miss alignment of resonance position at 16 GHz.

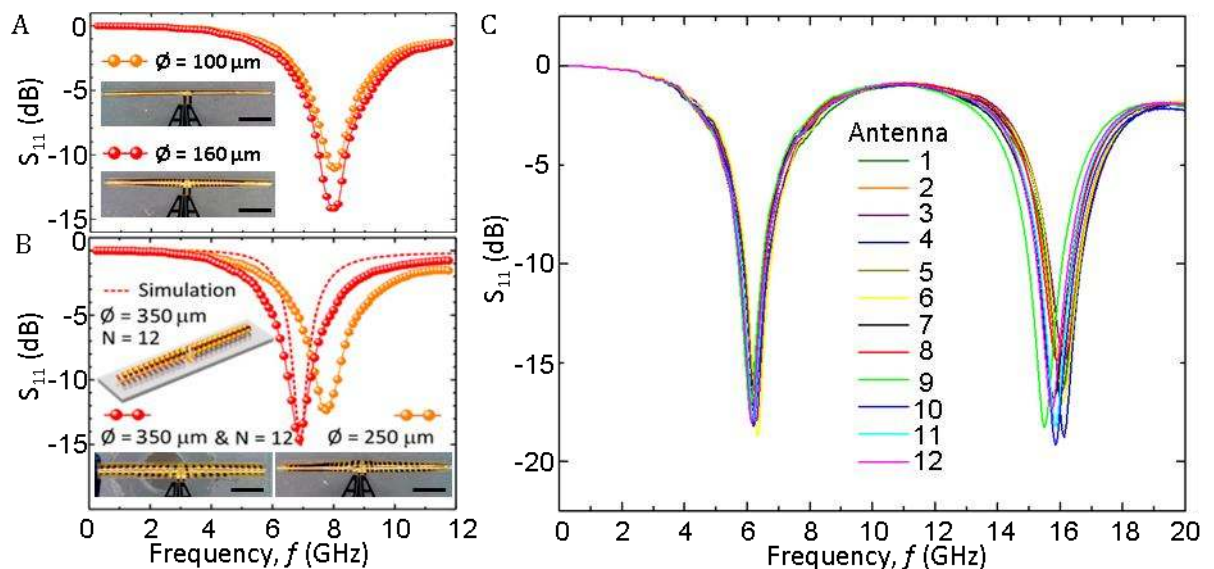


Figure 5.23: Measurement of S_{11} parameters for self-assembled helical antennas. A and B) Experimentally measured S_{11} parameter for antennas having different diameters (f). C) The S_{11} parameter for 12 arbitrarily chosen antennas (Figure 5.20a). Slight variation in position of resonant peaks at 16 GHz could be observed due to spreading of antenna diameters in the array. (Image A and B was adopted from ^[359])

As predicted in the simulation (Figure 5.8), encapsulated devices possess resonance peaks at smaller frequencies (Figure 5.24a). For instance, the resonance frequency of the antenna with a diameter of

5 Results and Discussions

350 μm was shifted to 5.7 GHz, which is close to the desired value of 5.8 GHz in the ISM band. It is important to emphasize that even after encapsulation, the antennas revealed an S_{11} parameter better than -10 dB, at the same time clearly demonstrating their suitability for communication tasks in the ISM radio bands.

5.3.2 Transmission between two normal mode helical antennas

The two encapsulated antennas shown on the Figure 5.24a were used to demonstrate possibility of transmission and reception using compact normal mode helical geometry. The S_{12} parameter is shown in Figure 5.24b representing signal accepted by the antenna #2 when emitted from the antenna #1. Black curve shows result for the simulation model presented on the Figure 5.1b and is in a good agreement with the measured signal (Figure 5.24b). The received signal consists of several peaks. Three of the peaks can be clearly attributed to the resonances of the antennas (~ 6 , ~ 14 , and ~ 19 GHz). Additionally, there are peaks at frequencies below 5 GHz, one of that peaks located exactly at 2.4 GHz. The Figure 5.24c shows the same parameter for different separations between the antennas. As expected for near field, increase in the distance between the helical antennas resulted in an exponential decay of the receiving signal (Figure 5.24c). Here we need to note that the signals level has a significant value in comparison to background noise.

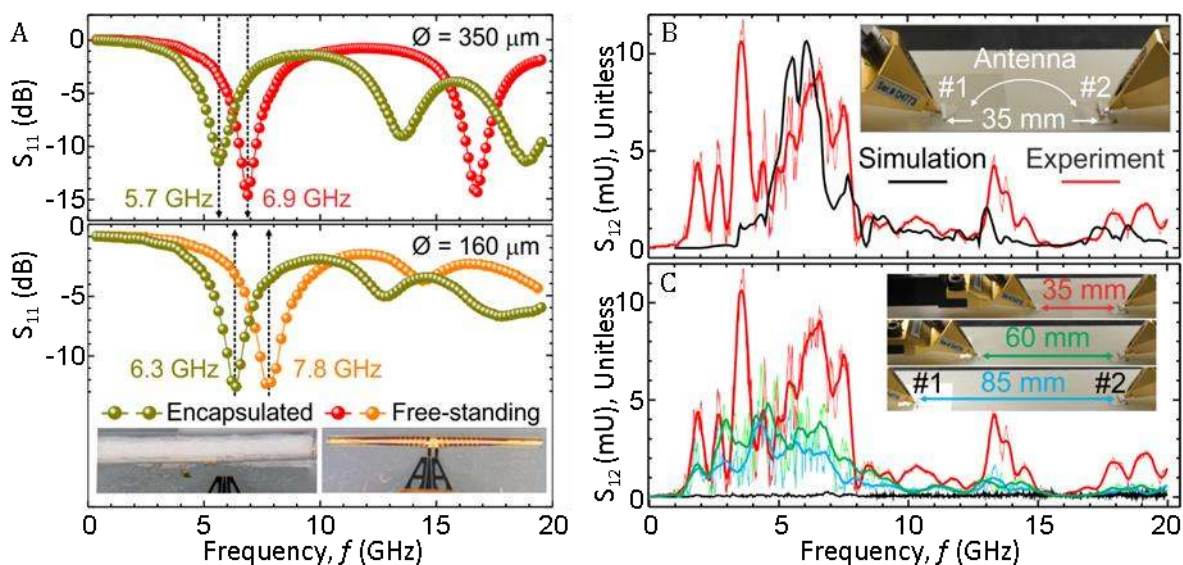


Figure 5.24: RF performance of encapsulated antennas. **A)** The S_{11} parameter of two experimentally realized antennas of different diameters measured as a function of frequency before and after the encapsulation process. Encapsulation results in a reduction of the resonance frequency of the antenna. The inset in (A) shows the optical micrographs of the antenna with 160 μm diameter before and after encapsulation. **B)** Communication between the two helical antennas separated by 35 mm. The experimental arrangement of the antennas is shown in the inset. **C)** An increase in distance between antennas resulted in lowering of the received signal intensity. The black line marks the background noise level and the inset shows distances between antennas. To convert mU into dB can be used the following equation: $\text{dB} = 20 \log(U)$. (Image was adopted from [359])

Additionally, a simple test was done checking possibility of the compact helical antenna to receive a signal from an external device. For the demonstration purposes, was selected a smartphone that could transmit in an appropriate RF band. For instance, Samsung Galaxy S2 operating under Android 4.0 operating system (OS) was a candidate for the test. This mobile phone has an engineering menu allowing a direct access to WiFi transceiver. Transceiver was settled to transmit data packages in a continuous 100 ms burst sequence mode with a 100% duty cycle and a 20 dBm power using 20 MHz bandwidth at 2.4 and 5.7 GHz channels. Because VNA was not synchronised with the transmitter of the smartphone, received power was averaged 36th times. At the same time, VNA was switched to S12 measurement mode with generator power adjusted to -5 dBm. In this configuration, the first $|Z|$ -probe was left disconnected preventing any occasional transfer of the own signal to the second port of the VNA, receiving only external signals by this port. Figure 5.25 shows a successful reception of the signal by an encapsulated helical antenna using the network analyser. Dipole type dependence was observed when the phone was swept around the antenna at a constant distance.

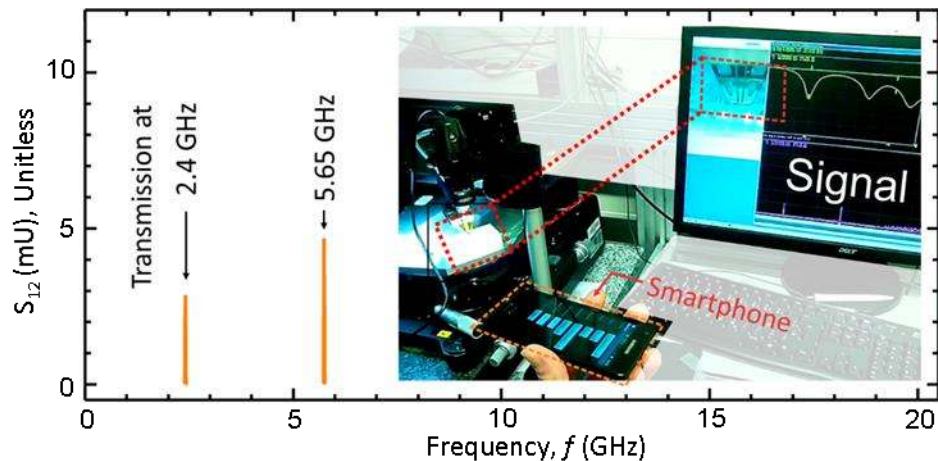


Figure 5.25: Experiment demonstrating the signal transmission from a smartphone to the antenna. Red dashed lines point out the antenna connected via $|Z|$ - probe. To convert mU into dB can be used the following equation: $\text{dB} = 20 \log(U)$. (Image is adopted from ^[359])

5.3.3 Implanted antenna

Small size of the antenna opens-up a possibility to implant it into a tooth during a dental operation or under the skin using for instance a regular syringe injection through a needle. Figure 5.26a presents conceptual application of such implants, where the relevant doctoral information or sensory data, e.g., temperature, pH, glucose level, could be acquired and transmitted by the implant to an external device, e.g., a smartphone. For a dental implant, the size of the device is absolutely crucial and cannot exceed $5 \times 3 \times 2 \text{ mm}^3$ of maximum cavity size applied in the dental surgery.^[390] For this demonstration, an encapsulated normal mode helical antenna was embedded into a tooth prosthetics made of an acrylic composite (inset in Figure 5.26b). As relevant for implant applications, the embedded antenna was located in the far-field region at a distance of 220 mm from the transmitting

5 Results and Discussions

antenna. For the latter, we used a standard helical antenna tuned to the resonance frequency of 5.8 GHz. As the self-assembled helical antenna is not equipped with a transceiver module, we applied the backscattering approach to address it. In this measurement protocol, we monitored the scattered power from the investigated antenna by receiving the reflected signal in phase with the transmitted signal (Figure 5.26c). If antenna is placed on the distance of several wavelengths down to one quarter, an incoming signal will be in the opposite phase resulting in power compensation, this will lead to increase in observed S_{11} parameter.

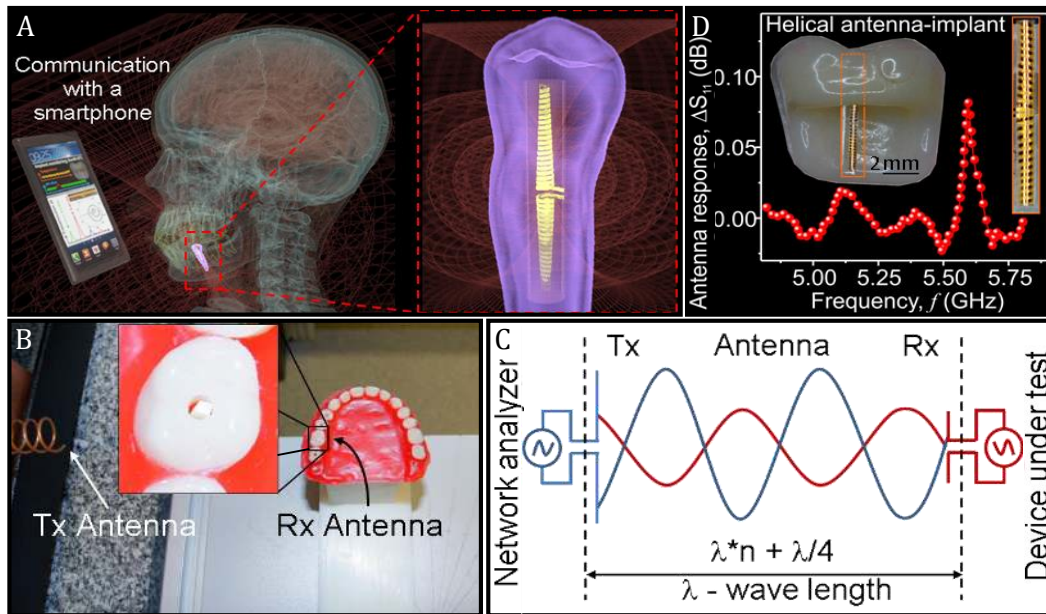


Figure 5.26: Concept of a smart implant for in-body applications. A) Such as a wireless tooth implant. B) The encapsulated compact helical antenna prepared by strain engineering with a total length of 5.5 mm and $\sim 400 \mu\text{m}$ width fits perfectly into a cavity prepared in the model of a tooth (inset). C) Schematic representation of the experiment performed in (B). D) The response of the antenna implant can be accessed wirelessly, as revealed by the presence of a peak in the scattered signal at the resonant frequency of the antenna. (Image A and D is adopted from [359])

The measurements were performed using a network analyzer set to an output power of -5 dBm , a bandwidth of 10 kHz and signal was averaged over 36 scans to eliminate the possible effect of the environment fluctuation. First, we performed the reference measurement of the transmitting antenna by investigating the frequency dependence of its return loss, the S_{11} parameter. In this study, the helical antenna is not inserted in the model of a tooth. In this manner, we captured the possible impact of the complex environment on the scattered signal. Next, we introduced the encapsulated helical antenna into the tooth and monitored the modification of the scattered signal with respect to the reference measurement. The response from the encapsulated helical antenna after subtracting the initial reference measurement is shown on the Figure 5.26d as the frequency dependent antenna response, ΔS_{11} . The presence of a clear peak in the scattered signal at the resonant frequency of the helical antenna unambiguously proves the possibility of radiating a signal sufficiently strong to be detected by the end device.

5.3 Characterisation of compact helical antennas

It was shown, that it is possible to make a small antenna operating in the ISM band and having dimensions of only $5.5 \times 0.5 \times 0.5 \text{ mm}^3$. Structures with these geometrical parameters could be easily implanted with standard medical syringes using 16–26 gauge needles with typical inner diameters of 1.19–0.26 mm. To demonstrate this possibility, were made to bio-mimicking polymeric dummies consisting from PDMS and Gelatine materials which has similar stiffness with a human cartilage^[391] and skin^[392], respectively. For the implantation were used hypodermic needles with wire gauge 26 (0.464 mm) and 17 (1.473 mm), internal diameter is (0.26 mm) and (1.067 mm) (Figure 5.27a, b), respectively. Needles were manually loaded with freestanding and encapsulated antennas. Afterward, needles were inserted into material and antennas were implanted using copper wire, to push the antenna in an opposite direction withdrawing the needle. It was found that is enough to move antenna outside the needle until the tip to be picked up by the surrounding material. Figure 5.27c,d present antennas after implantation procedure, and an optical investigation through material did not reveal any defect in the antennas. As a result, it could be considered that antennas are fully compatible with inject implantation technique.

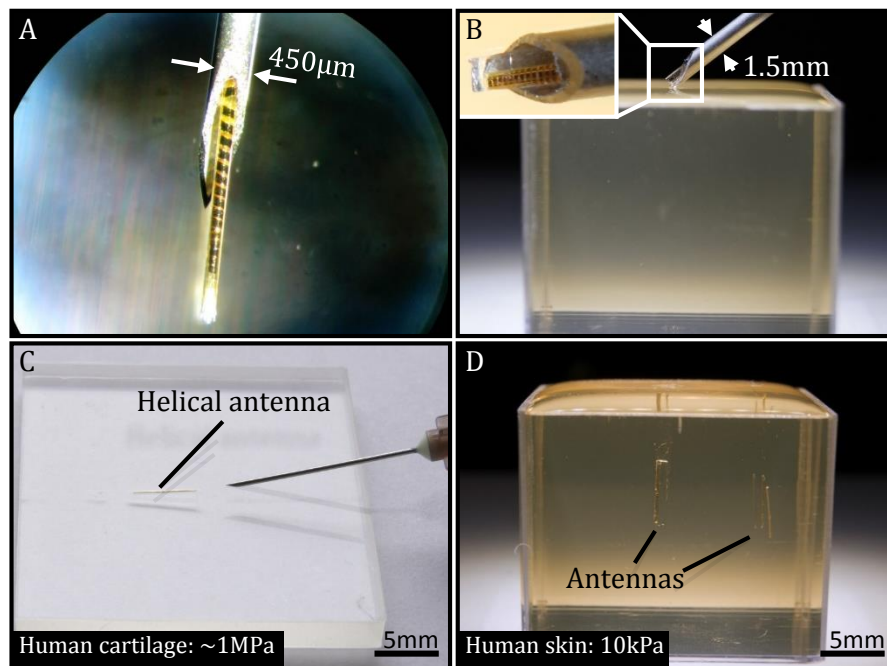


Figure 5.27: Antennas implanted into a bio-mimicking polymeric matrix. These antennas are sufficiently compact to be implanted in an elastomeric gelatine matrix using standard medical syringes with an inner diameter of $350 \mu\text{m}$, thus helping to minimize discomfort during and after implantation.

6 Conclusion and Outlook

6.1 Conclusion

In conclusion, compact self-assembled implantable helical antennas are developed, operating in the ISM radio band at 5.8 and 2.4 GHz in a biomimetic environment. The total length of the 3D antenna is only 5.5 mm, which is approximately 5 times smaller than the conventional 2D realization of a dipole antenna in a free space, operating at 5.8 GHz and being smaller than any implantable antenna reported so far. In this work, the main hurdles in the implementation of compact self-assembling antennas were successfully resolved, namely: (1) the difficulty of the impedance matching process requiring a specific design of the helical antenna to be used without introducing external matching components maintaining good transmission efficiency; (2) mechanical stabilization of 3D helical architectures; (3) the technology that features a cost- and time-efficient fabrication with a good yield for small antennas. A novel technological platform based on photopatternable, thermally, chemically and physically stable imide- and acrylic-based polymers was developed allowing encapsulation of the antenna into different dielectric materials and a possibility to tune the resonance frequency.

Mechanical simulations provide a clear vision on the rolling process of planar polymeric films into tubular structures. The simulations reveal that planar structures with a small longitudinal length and applied conditions when ($W \gg L$) and ($L \leq C$) could be self-assembled into the tube with a minimum probability of defects. To particularly overcome this narrow specification, the planar design was adjusted, introducing linker elements that represent local artificial limits in the aspect ratio of the structure and allow for virtually any geometry of the planar structure to be rolled. A successful optimization of linkers has significantly improved the yield of tubular structures. Relying on the developed polymeric technology, fabricating arrays of antennas on large areas with a yield close to 100% became possible in a highly parallel self-assembly process, which may potentially enable low-cost production of compact injectable wireless devices. Applicability for high volume commercial production is facilitated by application of industrially standard thin-film processing equipment and methods, including optical lithography and magnetron sputtering.

The realized self-assembled helical antenna was designed to match 50Ω , which is the most common impedance for microelectronic devices, without relying on any external active or passive components. Therefore, the total volume of the final encapsulated antenna is less than $5.5 \times 0.5 \times 0.5 \text{ mm}^3$. With these geometrical dimensions, this implantable antenna is the smallest reported among others that operate at 5.8 GHz in air and is impedance matched to 50Ω . At the same time this antenna demonstrates the simultaneous compatibility with higher impedance devices matched to 50, 75, 90 and 125Ω without any modifications in the geometry, it appears to be matched

Conclusion and Outlook

to all these standard impedances exhibiting the S11 parameter better than -10 dB at the resonance frequency. This is of great advantage for applications in various electronic circuits possessing non-standard impedances.

An efficient communication between antennas was confirmed experimentally; furthermore, the signal transmission from a smartphone to a helical antenna was successfully demonstrated. Because of their shape and dimensions, the fabricated antennas could be successfully implanted into biological phantoms using standard medical syringes. Accounting for relevant dielectric parameters of biological tissues, an acceptable SAR level for electromagnetic waves generated by the antenna was verified in the model. The antenna was embedded into a model of the human head, where the working frequency was reduced to 2.45 GHz, resulting in the smallest antenna operating at 2.45 GHz of ISM band still being matched to standard impedances. This demonstrates a strong application potential for the fabricated helical antennas as a key component of a transmitter system in smart wireless implants.

6.2 Outlook

This development revealed a straightforward approach for the fabrication of antennas possessing room for a simple optimization of electrical performance and miniaturization of the antenna. The experimental realization of functional smart implants requires further development steps, where the compact antenna can be integrated as part of a radio frequency flexible electronics e.g. identification systems, various data acquisition devices, pH, neuronal signal stimulators and acquisition systems as well as temperature sensors, to enable the realization of fully functional wireless in-body implants. Recently, flexible low frequency ^[393,394] and RF^[394] circuits based on IGZO semiconductors, and their potential application in cuff type devices for neuronal implant^[32] was demonstrated. This gives a possibility for future integration of both technologies in a single self-assembled helical implantable structure. The realized technology can be extended even further, and the helical antenna can be prepared in a single fabrication process from the planar layout, accommodating further functional elements, including energy storage,^[318,319] magnetic^[29] and fluidic^[324] sensors, hence realizing in-vivo smart implants based on multifunctional compact electronics, including even fully autonomous systems^[395]. One of the transition steps in the development will be implantation of helical antennas into real biological environment and its characterization with respect to biological, mechanical and electrical parameters.

References

1. F.S. Remington. "The Smoke Signal", Amon Carter Museum, Fort Worth, Texas, **1905**
2. E.B. Leonard. "Pigeon Voyagers". *Harper's New Monthly Magazine*, **1873**, 46(275), 659–668.
3. D.E. Johnson, J.L. Hilburn, J.R. Johnson. "Basic electric circuit analysis", Prentice-Hall, Inc., Upper Saddle River, NJ, USA, **1990**
4. R. Baierlein. "Newton to Einstein: the trail of light: an excursion to the wave-particle duality and the Special Theory of Relativity", Cambridge University Press, **1992**
5. P.K. Bondyopadhyay. "Guglielmo Marconi - The father of long distance radio communication - An engineer's tribute", In 25th European Microwave Conference; IEEE, Bologna, Italy, **1995**, 879–885. DOI: 10.1109/EUMA.1995.337090
6. A.E. Evenson. "The telephone patent conspiracy of 1876: the Elisha Gray-Alexander Bell controversy and its many players", McFarland, Jefferson, NC, USA, **2000**
7. C.K. Martin. "Pioneer Profiles: Donald Davies". *The Bulletin of the Computer Conservation Society*, Computer Resurrection, **2008**, 44(44)
8. S. Pace, G.P. Frost, I. Lachow, D.R. Frelinger, D. Fossum, D. Wassem, M.M. Pinto. "The Global Positioning System: Assessing National Policies", RAND Corporation, Santa Monica, **1995**
9. J. Landt, B. Catlin. "Shrouds of Time: The History of RFID". *AIM Publication*, **2001**, 11.
10. C. Bisdikian. "An overview of the Bluetooth wireless technology". *IEEE Communications Magazine*, **2001**, 39(12), 86–94. DOI: 10.1109/35.968817
11. K. Shailandra. "An overview of Technical aspect for WiFi Networks Technology". *International Journal of Electronics and Computer Science Engineering*, **2012**, 1(1), 28–34.
12. M. Anju, U. Gawas. "An Overview on Evolution of Mobile Wireless Communication Networks: 1G-6G". *IJRITCC*, **2015**, 3(5), 3130–3133.
13. W.H. Chen, S. Joo, S. Sayilir, R. Willmot, T.Y. Choi, D. Kim, J. Lu, D. Peroulis, B. Jung. "A 6-Gb/s Wireless Inter-Chip Data Link Using 43-GHz Transceivers and Bond-Wire Antennas". *IEEE Journal of Solid-State Circuits*, **2009**, 44(10), 2711–2721. DOI: 10.1109/JSSC.2009.2027932
14. P.K. Saha, N. Sasaki, T. Kikkawa. "A CMOS UWB transmitter for intra/inter-chip wireless communication", In Eighth IEEE International Symposium on Spread Spectrum Techniques and Applications - Programme and Book of Abstracts (IEEE Cat. No.04TH8738); IEEE, **2004**, 962–966. DOI: 10.1109/ISSSTA.2004.1371844
15. A. Josef, R. Peter, N. Tobias, M. Amine, T. Michel, K. Matthias, M. Farooq, Y. Hristomir, A. Johannes. "Chip-to-Chip and On-Chip Communications". In Ultra-Wideband Radio Technologies for Communications, Localization and Sensor Applications; I.W. and T.Z. Reiner Thomä, Reinhard H. Knöchel, Jürgen Sachs, Ed.; InTech, **2013**, 75–108. DOI: 10.5772/52981
16. M.F. Chang, V.P. Roychowdhury, Y. Zhang, Liyang Shin, Hyunchol Qian. "RF / Wireless Interconnect for Inter- and Intra-Chip Communications". **2001**, 89(4)
17. C. Brunckhorst, R. Candinas, S. Furman. "Ake Senning 1915-2000". *Pacing and Clinical Electrophysiology*, **2000**, 23(11), 1710–1710. DOI: 10.1046/j.1460-9592.2000.01710.x

References

18. K. Fischer, K. Degenkolb, W. Fischer, A. Mendelsohn. "Nanoscale Constrained Delivery: A Novel Technology for Subdermal Implants". *Controlled Release Society Newsletter*, **2014**, 31(4), 14–16.
19. A. Cobo, R. Sheybani, H. Tu, E. Meng. "A wireless implantable micropump for chronic drug infusion against cancer". *Sensors and Actuators, A: Physical*, Elsevier B.V., **2016**, 239, 18–25. DOI: 10.1016/j.sna.2016.01.001
20. D. Johnson, D. Borkholder. "Towards an Implantable, Low Flow Micropump That Uses No Power in the Blocked-Flow State". *Micromachines*, **2016**, 7(6), 99. DOI: 10.3390/mi7060099
21. T. Maleki, Ning Cao, Seung Hyun Song, Chinghai Kao, Song-Chu Ko, B. Ziaie. "An Ultrasonically Powered Implantable Micro-Oxygen Generator (IMOG)". *IEEE Transactions on Biomedical Engineering*, **2011**, 58(11), 3104–3111. DOI: 10.1109/TBME.2011.2163634
22. C. Pollo, A. Kaelin-Lang, M.F. Oertel, L. Stieglitz, E. Taub, P. Fuhr, A.M. Lozano, A. Raabe, M. Schupbach. "Directional deep brain stimulation: an intraoperative double-blind pilot study". *Brain*, **2014**, 137(7), 2015–2026. DOI: 10.1093/brain/awu102
23. E. Smeets. "Inbouw van een stoorzender bij clusterhoofdpijn". *Hoofdzaken*, **2015**, 1, 40–41.
24. R.J. Mobbs, S. Nair, P. Blum. "Peripheral nerve stimulation for the treatment of chronic pain". *Journal of Clinical Neuroscience*, **2007**, 14(3), 216–221. DOI: 10.1016/j.jocn.2005.11.007
25. M.S. Mannoor, H. Tao, J.D. Clayton, A. Sengupta, D.L. Kaplan, R.R. Naik, N. Verma, F.G. Omenetto, M.C. McAlpine. "Graphene-based wireless bacteria detection on tooth enamel". *Nature Communications*, Nature Publishing Group, **2012**, 3(2), 763. DOI: 10.1038/ncomms1767
26. Y.J. Lee, S.J. Park, K.S. Yun, J.Y. Kang, S.H. Lee. "Enzymeless glucose sensor integrated with chronically implantable nerve cuff electrode for in-situ inflammation monitoring". *Sensors and Actuators B: Chemical*, **2016**, 222, 425–432. DOI: 10.1016/j.snb.2015.08.091
27. S.L. Swisher, M.C. Lin, A. Liao, E.J. Leefflang, Y. Khan, F.J. Pavinatto, K. Mann, A. Naujokas, D. Young, ... M.M. Maharbiz. "Impedance sensing device enables early detection of pressure ulcers in vivo.". *Nature Communications*, Nature Publishing Group, **2015**, 6, 6575. DOI: 10.1038/ncomms7575
28. W. Wei, Y. Song, L. Wang, S. Zhang, J. Luo, S. Xu, X. Cai. "An implantable microelectrode array for simultaneous L-glutamate and electrophysiological recordings in vivo". *Microsystems {&} Nanoengineering*, **2015**, 1, 15002. DOI: 10.1038/micronano.2015.2
29. D. Karnaushenko, D.D. Karnaushenko, D. Makarov, S. Baunack, R. Schäfer, O.G. Schmidt. "Self-Assembled On-Chip-Integrated Giant Magneto-Impedance Sensorics". *Advanced Materials*, **2015**, 27(42), 6582–6589. DOI: 10.1002/adma.201503127
30. N. Münzenrieder, D. Karnaushenko, L. Petti, G. Cantarella, C. Vogt, L. Bütke, D.D. Karnaushenko, O.G. Schmidt, D. Makarov, G. Tröster. "Sensors: Entirely Flexible On-Site Conditioned Magnetic Sensorics". *Advanced Electronic Materials*, **2016**, 2(8), 1–10. DOI: 10.1002/aelm.201670043
31. K. Appasani, R.K. Appasani. "Stem Cells & Regenerative Medicine", K. Appasani, R.K. Appasani, Eds.; Humana Press, Totowa, USA, **2011**, DOI: 10.1007/978-1-60761-860-7
32. D.D. Karnaushenko, N. Münzenrieder, D.D. Karnaushenko, B. Koch, A.K. Meyer, S. Baunack, L. Petti, G. Tröster, D. Makarov, O.G. Schmidt. "Biomimetic Microelectronics for Regenerative Neuronal Cuff Implants". *Advanced Materials*, **2015**, 27(43), 6797–6805. DOI: 10.1002/adma.201503696

33. X. Navarro, T.B. Krueger, N. Lago, S. Micera, T. Stieglitz, P. Dario. "A Critical Review of Interfaces with the Peripheral Nervous System for the Control of Neuroprostheses and Hybrid Bionic Systems". *J Peripher Nerv Syst*, **2005**, *10*, 229–258. DOI: 10.1111/j.1085-9489.2005.10303.x
34. P. Troyk, S. Bredeson, S. Cogan, M. Romero-Ortega, S. Suh, Z. Hu, A. Kanneganti, R. Granja-Vazquez, J. Seifert, M. Bak. "In-vivo tests of a 16-channel implantable wireless neural stimulator", In 2015 7th International IEEE/EMBS Conference on Neural Engineering (NER); IEEE, **2015**, 474–477. DOI: 10.1109/NER.2015.7146662
35. S.K. Arfin, M.A. Long, M.S. Fee, R. Sarpeshkar. "Wireless neural stimulation in freely behaving small animals". *Journal of neurophysiology*, **2009**, *102*(1), 598–605. DOI: 10.1152/jn.00017.2009
36. K.D.D. Wise, A.M.M. Sodagar, Ying Yao, M.N.N. Gulari, G.E.E. Perlin, K. Najafi. "Microelectrodes, Microelectronics, and Implantable Neural Microsystems". *Proceedings of the IEEE*, **2008**, *96*(7), 1184–1202. DOI: 10.1109/JPROC.2008.922564
37. M.L. Homer, A. V. Nurmikko, J.P. Donoghue, L.R. Hochberg. "Sensors and decoding for intracortical brain computer interfaces". *Annual review of biomedical engineering*, **2013**, *15*, 383–405. DOI: 10.1146/annurev-bioeng-071910-124640
38. R.M. Rothschild. "Neuroengineering tools/applications for bidirectional interfaces, brain-computer interfaces, and neuroprosthetic implants – a review of recent progress". *Frontiers in Neuroengineering*, **2010**, *3*, 112. DOI: 10.3389/fneng.2010.00112
39. M. Kocaturk, H.O. Gulcur, R. Canbeyli. "Toward building hybrid biological/in silico neural networks for motor neuroprosthetic control". *Frontiers in Neurorobotics*, **2015**, *9*(AUG), 1–21. DOI: 10.3389/fnbot.2015.00008
40. A. Al-Kaisy, J.P. Van Buyten, I. Smet, S. Palmisani, D. Pang, T. Smith. "Sustained Effectiveness of 10 kHz High-Frequency Spinal Cord Stimulation for Patients with Chronic, Low Back Pain: 24-Month Results of a Prospective Multicenter Study". *Pain Medicine*, **2014**, *15*(3), 347–354. DOI: 10.1111/pme.12294
41. T.J. Oxley, N.L. Opie, S.E. John, G.S. Rind, S.M. Ronayne, T.L. Wheeler, J.W. Judy, A.J. McDonald, A. Dornom, ... T.J. O'Brien. "Minimally invasive endovascular stent-electrode array for high-fidelity, chronic recordings of cortical neural activity". *Nature Biotechnology*, **2016**, *34*(2), 320–327. DOI: 10.1038/nbt.3428
42. F. Thinnis-Elker, O. Iljina, J.K. Apostolides, F. Kraemer, A. Schulze-Bonhage, A. Aertsen, T. Ball. "Intention concepts and brain-machine interfacing". *Frontiers in Psychology*, **2012**, *3*, 1–10. DOI: 10.3389/fpsyg.2012.00455
43. T. Carlson, L. Tonin, S. Perdakis, R. Leeb, J.D.R. Millan. "A hybrid BCI for enhanced control of a telepresence robot". *Proceedings of the Annual International Conference of the IEEE Engineering in Medicine and Biology Society, EMBS*, **2013**, 3097–3100. DOI: 10.1109/EMBC.2013.6610196
44. D. a Borton, M. Yin, J. Aceros, A. Nurmikko. "An implantable wireless neural interface for recording cortical circuit dynamics in moving primates". *Journal of neural engineering*, **2013**, *10*(2), 26010. DOI: 10.1088/1741-2560/10/2/026010
45. M.R. Kasten, A.M. Ievins, C.T. Moritz. "Neural Prostheses". In eLS; John Wiley & Sons, Ltd, Chichester, UK, **2015**, 1–9. DOI: 10.1002/9780470015902.a0024011
46. E. Hardin, R. Kobetic, L. Murray, M. Corado-Ahmed, G. Pinault, J. Sakai, S.N. Bailey, C. Ho, R.J. Triolo. "Walking after incomplete spinal cord injury using an implanted FES system: a case

References

- report". *Journal of rehabilitation research and development*, **2007**, 44(3), 333–346. DOI: 10.1682/JRRD.2006.02.0013
47. D.M. Long. "Toward Replacement Parts of the Brain, Implantable Biomimetic Electronics as Neural Prostheses", T.W. Berger, D.L. Glanzman, Eds.; A Bradford Book the MIT press, Cambridge, Massachusetts, **2005**, DOI: 10.1097/01.wnq.0000190409.71157.53
48. T.W. Berger, M. Baudry, R.D. Brinton, J.S. Liaw, V.Z. Marmarelis, A. Yoondong Park, B.J. Sheu, A.R. Tanguay Jr., A.R. Tanguay Jr., ... A.R. Tanguay Jr. "Brain-implantable biomimetic electronics as the next era in neural prosthetics Proc. IEEE (USA)". *Proceedings of the IEEE*, **2001**, 89(7), 993–1012.
49. M. Grimmer, A. Seyfarth. "Mimicking Human-Like Leg Function in Prosthetic Limbs". In Neuro-Robotics, From Brain Machine Interfaces to Rehabilitation Robotics; Springer Science and Business Media Dordrecht, **2014**, 105–155. DOI: 10.1007/978-94-017-8932-5_5
50. R.F. Weir, D. Ph. "Design of Artificial Arms and Hands for Prosthetic Applications". *Standard Handbook of Biomedical Engineering and Design*, **2004**, 1–61.
51. B.S. Wilson. "Cochlear implants: Current designs and future possibilities". *The Journal of Rehabilitation Research and Development*, **2008**, 45(5), 695–730. DOI: 10.1682/JRRD.2007.10.0173
52. H. Lorach, X. Lei, L. Galambos, T. Kamins, K. Mathieson, R. Dalal, P. Huie, J. Harris, D. Palanker. "Interactions of prosthetic and natural vision in animals with local retinal degeneration". *Investigative Ophthalmology and Visual Science*, **2015**, 56(12), 7444–7450. DOI: 10.1167/iovs.15-17521
53. A.C. Ho, M.S. Humayun, J.D. Dorn, L. Da Cruz, G. Dagnelie, J. Handa, P.O. Barale, J.A. Sahel, P.E. Stanga, ... R.J. Greenberg. "Long-Term Results from an Epiretinal Prosthesis to Restore Sight to the Blind". *Ophthalmology*, Elsevier Inc, **2015**, 122(8), 1547–1554. DOI: 10.1016/j.ophtha.2015.04.032
54. F.H. Guenther, J.S. Brumberg, E. Joseph Wright, A. Nieto-Castanon, J.A. Tourville, M. Panko, R. Law, S.A. Siebert, J.L. Bartels, ... P.R. Kennedy. "A wireless brain-machine interface for real-time speech synthesis". *PLoS ONE*, **2009**, 4(12) DOI: 10.1371/journal.pone.0008218
55. T. Sekitani, T. Yokota, T. Someya. "Large-Area, Printed Organic Circuits for Ambient Electronics". *Large Area and Flexible Electronics*, **2015**, 365–380. DOI: 10.1002/9783527679973.ch13
56. M. Pritschow, C. Reuter, H. Richter, I. Schindler, M. Zimmermann. "Ultra-Thin Chips on Foil for Flexible Electronics Horst". *2008 IEEE International Solid-State Circuits Conference (ISSCC 2008)*, **2008**, 18, 334–335.
57. J. Reeder, M. Kaltenbrunner, T. Ware, D. Arreaga-Salas, A. Avendano-Bolivar, T. Yokota, Y. Inoue, M. Sekino, W. Voit, ... T. Someya. "Mechanically adaptive organic transistors for implantable electronics". *Advanced Materials*, **2014**, 26(29), 4967–4973. DOI: 10.1002/adma.201400420
58. L. Xu, S.R. Gutbrod, Y. Ma, A. Petrossians, Y. Liu, R.C. Webb, J.A. Fan, Z. Yang, R. Xu, ... J.A. Rogers. "Materials and Fractal Designs for 3D Multifunctional Integumentary Membranes with Capabilities in Cardiac Electrotherapy". *Advanced Materials*, **2015**, 27(10), 1731–1737. DOI: 10.1002/adma.201405017
59. M. Melzer, M. Kaltenbrunner, D. Makarov, D.D. Karnaushenko, D.D. Karnaushenko, T. Sekitani, T. Someya, O.G. Schmidt. "Imperceptible magnetoelectronics". *Nature Communications*, Nature

- Publishing Group, **2015**, 6(January), 1–8. DOI: 10.1038/ncomms7080
60. H.-L. (Cindy) Kao, C. Holz, A. Roseway, A. Calvo, C. Schmandt. "Rapidly prototyping on-skin user interfaces using skin-friendly materials", In Proceedings of the 2016 ACM International Symposium on Wearable Computers - ISWC '16; ACM Press, New York, New York, USA, **2016**, 16–23. DOI: 10.1145/2971763.2971777
 61. K. Ranganath, P. Krupali, M. Sravanthy. "Electronic Skin-the Sense of Touch". *IJCSET /August*, **2011**, 1(7), 387–390.
 62. J.A. Rogers. "Electronics for the Human Body". *Jama*, **2015**, 313(6), 561. DOI: 10.1001/jama.2014.17915
 63. W.H. Yeo, Y.S. Kim, J. Lee, A. Ameen, L. Shi, M. Li, S. Wang, R. Ma, S.H. Jin, ... J.A. Rogers. "Multifunctional epidermal electronics printed directly onto the skin". *Advanced Materials*, **2013**, 25(20), 2773–2778. DOI: 10.1002/adma.201204426
 64. A. Chortos, J. Liu, Z. Bao. "Pursuing prosthetic electronic skin". *Nature materials*, Nature Publishing Group, **2016**, (July), 1–14. DOI: 10.1038/nmat4671
 65. S.P. Lacour. "Epidermal electronics: Skin health monitoring". *Nature Materials*, Nature Publishing Group, **2015**, 14(7), 659–660. DOI: 10.1038/nmat4328
 66. D. Hodgins, A. Bertsch, N. Post, M. Frischholz, B. Volckaerts, J. Spensley, J.M. Wasikiewicz, H. Higgins, F. Von Stetten, L. Kenney. "Healthy Aims: Developing New Medical Implants and Diagnostic Equipment". *IEEE Pervasive Computing*, **2008**, 7(1), 14–20. DOI: 10.1109/MPRV.2008.8
 67. Y. Li, M. Alam, S. Guo, K. Ting, J. He. "Electronic bypass of spinal lesions: activation of lower motor neurons directly driven by cortical neural signals". *Journal of NeuroEngineering and Rehabilitation*, **2014**, 11(1), 107. DOI: 10.1186/1743-0003-11-107
 68. C.M. Boutry, H. Chandralalim, P. Streit, M. Schinhammer, C. Hanzi, C. Hierold. "Towards biodegradable wireless implants". *Philosophical Transactions of the Royal Society A: Mathematical, Physical and Engineering Sciences*, **2012**, 370(1967), 2418–2432. DOI: 10.1098/rsta.2011.0439
 69. G. Breed. "Basic Principles of Electrically Small Antennas". *High Frequency Electronics*, Summit Technical Media, LLC, **2007**, 1–3. DOI: 10.1016/B978-0-12-800036-6.00001-6
 70. Chung-Kwang Chou, J. D'Andrea, R. Petersen. "IEEE Standard for Safety Levels With Respect to Human Exposure to Radio Frequency Electromagnetic Fields, 3 kHz to 300 GHz", Institute of Electrical and Electronics Engineers, Inc., New York, **2006**
 71. Health Protection Agency. "Health Effects from Radiofrequency Electromagnetic Fields", Health Protection Agency, **2012**
 72. E.A. Williams, G.A. Jones, D.H. Layer, T.G. Osenowsky. "10th Edition", Elsevier, USA, Burlington, **2007**
 73. R. Syms, J. Cozens. "Optical Guided Waves and Devices", McGRAW-HILL, Berkshire, England, **1992**
 74. A. Balanis, Constantine, C. Balanis. "Modern Antenna Handbook", C.A. Balanis, Ed.; John Wiley & Sons, Inc., Hoboken, NJ, USA, **2008**, DOI: 10.1002/9780470294154
 75. R. Ludwig, P. Bretchko. "RF Circuit Design – Theory and Applications", Prentice Hall, USA, New

References

Jersey, 2000

76. G.E. Christensen, J.H. Song, W. Lu, I. El Naqa, D. a Low. "Tracking lung tissue motion and expansion/compression with inverse consistent image registration and spirometry". *Medical physics*, **2007**, *34*, 2155–2163. DOI: 10.1118/1.2731029
77. D. Stoyanov, G.P. Mylonas, F. Deligianni, A. Darzi, G.Z. Yang. "Soft-tissue motion tracking and structure estimation for robotic assisted MIS procedures". *Lecture Notes in Computer Science (including subseries Lecture Notes in Artificial Intelligence and Lecture Notes in Bioinformatics)*, **2005**, *3750 LNCS*, 139–146. DOI: 10.1007/11566489_18
78. P.R. Hoskins, W.N. McDicken. "Colour ultrasound imaging of blood flow and tissue motion.". *The British Journal of Radiology*, **1997**, *70*, 878–890. DOI: 10.1259/bjr.70.837.9486063
79. K. Fujimoto, H. Morishita. "Modern Small Antennas", Cambridge University Press, New York, **2013**, DOI: <https://doi.org/10.1017/CBO9780511977602>
80. H. Wheeler. "Small antennas". *IEEE Transactions on Antennas and Propagation*, **1975**, *23*(4), 462–469. DOI: 10.1109/TAP.1975.1141115
81. L.J. Chu. "Physical Limitations of Omnidirectional Antennas". *Journal of Applied Physics*, **1948**, *19*(64), 1163–1175. DOI: 10.1063/1.1715038
82. R.F. Harrington. "Effect of antenna size on gain, bandwidth, and efficiency". *Journal of Research of the National Bureau of Standards, Section D: Radio Propagation*, **1960**, *64D*(1), 1. DOI: 10.6028/jres.064D.003
83. K. Song, A. Shon, J. Chu, K. Choi, D. Hwang, I. Youn. "An Implantable Wireless System for Muscle Afferent Recording from the Sciatic Nerve during Functional Electrical Stimulation". *35th Annual International Conference of the IEEE EMBS*, **2013**, 3610–3613.
84. P. Larson, B. Towe. "Miniature Ultrasonically Powered Wireless Nerve Cuff Stimulator". *Proceedings of the 5th International IEEE EMBS Conference on Neural Engineering*, **2011**, *ThE1.6*, 265–268.
85. S.H. Lee, J.H. Jung, Y.M. Chae, J.-K.F. Suh, J.Y. Kang. "Fabrication and characterization of implantable and flexible nerve cuff electrodes with Pt, Ir and IrOx films deposited by RF sputtering". *Journal of Micromechanics and Microengineering*, **2010**, *20*(3), 1–8. DOI: 10.1088/0960-1317/20/3/035015
86. X. Li, W.A. Serdijn, W. Zheng, Y. Tian, B. Zhang. "The injectable neurostimulator: An emerging therapeutic device". *Trends in Biotechnology*, Elsevier Ltd, **2015**, *33*(7), 388–394. DOI: 10.1016/j.tibtech.2015.04.001
87. B.L. McLaughlin, B. Smith, J. Lachapelle, D. Traviglia, T.S. Sriram, D. O'Dowd. "Ultra-high density packaging technology for injectable medical devices", In Proceedings of the Annual International Conference of the IEEE Engineering in Medicine and Biology Society, EMBS; **2011**, 2897–2900. DOI: 10.1109/IEMBS.2011.6090798
88. J. Liu, T.-M.M. Fu, Z. Cheng, G. Hong, T. Zhou, L. Jin, M. Duvvuri, Z. Jiang, P. Kruskal, ... C.M. Lieber. "Syringe-injectable electronics". *Nature Nanotechnology*, Nature Publishing Group, **2015**, *advance on*(June), 629–636. DOI: 10.1038/nnano.2015.115
89. P.R. Troyk. "Injectable Electronic Identification, Monitoring, and Stimulation Systems". *Annual Review of Biomedical Engineering*, **1999**, *1*(1), 177–209. DOI: 10.1146/annurev.bioeng.1.1.177

90. G.E. Loeb, F.J.R. Richmond, L.L. Baker. "The BION devices: injectable interfaces with peripheral nerves and muscles". *Neurosurgical focus*, **2006**, 20(5), E2. DOI: 10.3171/foc.2006.20.5.3
91. O. Yildiz, M. Seyrek, K.G. Ulusoy. "Biocompatibility of Dental Polymers". In *Polymer science: research advances, practical applications and educational aspects*; Formatex Research Center, Spain, Badajoz, **2016**, 89–98.
92. R. Bhola, S.M. Bhola, H. Liang, B. Mishra. "Biocompatible denture polymers - A review". *Trends in Biomaterials and Artificial Organs*, **2010**, 23(3), 129–136.
93. C. Hassler, T. Boretius, T. Stieglitz. "Polymers for neural implants". *Journal of Polymer Science, Part B: Polymer Physics*, **2011**, 49(1), 18–33. DOI: 10.1002/polb.22169
94. C. Cesar, B. Bufon, J. Diego, A. Espinoza, D.J. Thurmer, M. Bauer, C. Deneke, U. Zschieschang, H. Klauk, O.G. Schmidt. "Strained Nanomembranes". *Nano*, **2011**, 11(9), 3727–3733. DOI: 10.1021/nl201773d
95. M. Huang, F. Cavallo, F. Liu, M.G. Lagally. "Nanomechanical architecture of semiconductor nanomembranes". *Nanoscale*, **2011**, 3(1), 96–120. DOI: 10.1039/C0NR00648C
96. Y. Mei, D.J. Thurmer, C. Deneke, S. Kiravittaya, Y.-F.F. Chen, A. Dadgar, F. Bertram, B. Bastek, A. Krost, ... O.G. Schmidt. "Fabrication, self-assembly, and properties of ultrathin AlN/GaN porous crystalline nanomembranes: Tubes, spirals, and curved sheets". *ACS Nano*, **2009**, 3(7), 1663–1668. DOI: 10.1021/nn900580j
97. H.R. Kwag, J. V Serbo, P. Korangath, S. Sukumar, L.H. Romer, D.H. Gracias. "A Self-Folding Hydrogel In Vitro Model for Ductal Carcinoma.". *Tissue engineering. Part C, Methods*, **2016**, 22(4), 398–407. DOI: 10.1089/ten.TEC.2015.0442
98. V. Luchnikov, L. Balan. "Photochemistry for Advanced Nanoengineering: Polymer Microtubes with Inner Walls Coated with Silver Nanoparticles". *Nanomaterials and Nanotechnology*, **2014**, 4(20), 20. DOI: 10.5772/58762
99. G. Stoychev, S. Turcaud, J.W.C. Dunlop, L. Ionov. "Hierarchical Multi-Step Folding of Polymer Bilayers". *Advanced Functional Materials*, **2013**, 23(18), 2295–2300. DOI: 10.1002/adfm.201203245
100. S. Zakharchenko, E. Sperling, L. Ionov. "Fully biodegradable self-rolled polymer tubes: A candidate for tissue engineering scaffolds". *Biomacromolecules*, **2011**, 12(6), 2211–2215. DOI: 10.1021/bm2002945
101. L.P. Chia Gómez, P. Bollgruen, A.I. Egunov, D. Mager, F. Malloggi, J.G. Korvink, V. a. Luchnikov. "Vapour processed self-rolled poly(dimethylsiloxane) microcapillaries form microfluidic devices with engineered inner surface". *Lab on a Chip*, **2013**, 13(19), 3827. DOI: 10.1039/c3lc50542a
102. J. Gemio, J. Parron, J. Soler. "Parison and Propagation Losses Study". *Progress In Electromagnetics Research*, **2010**, 110, 437–452.
103. C. Buckenmaier, L. Bleckner, M.K. Sracic. "Military Advanced Regional Anesthesia and Analgesia", 3rd U.S. r The Henry M. Jackson Foundation for the Advancement of Military Medicine, Inc., Washington DC, **2004**
104. D.L. Hayes, S. Furman. "Cardiac Pacing : How It Started , Where We Are , Where We Are Going". **1957**, 619–627. DOI: 10.1046/j.1540-8167.2004.04088.x
105. W. Greatbatch, C.F. Holmes. "History of implantable devices". *IEEE Engineering in Medicine and*

References

- Biology Magazine*, **1991**, 10(3), 38--41+49. DOI: 10.1109/51.84185
106. P.M. Zoll, H.A. Frank, L.R.N. Zarsky, A.J. Linenthal, A.H. Belgard. "Long-term electric stimulation of the heart for Stokes-Adams disease.". *Annals of surgery*, **1961**, 154, 330–346.
107. M. Riordan, L. Hoddeson, C. Herring. "The invention of the transistor". *Reviews of Modern Physics*, **1999**, 71(2), S336–S345. DOI: 10.1103/RevModPhys.71.S336
108. T. Mittal. "Pacemakers – A journey through the years". *IJTCVS*, **2005**, 21, 236–249.
109. "Study: World Medical Devices Market", Acmite Market Intelligence, Ratingen, Germany, **2015**
110. O. Aquilina. "A brief history of cardiac pacing". *Images in Paediatric Cardiology*, **2006**, 8(2), 17–81.
111. S. Warren, R.L.L. Craft, J.T. Bosma. "Designing smart health care technology into the home of the future". *Proceedings of the First Joint BMES/EMBS Conference.*, **1999**, 2(505) DOI: 10.1109/IEMBS.1999.803832
112. H. Costin, C. Rotariu, O. Morancea, G. Andrusac, V. Cehan, V. Felea, I. Alexa, C. Costin. "Complex telemonitoring of patients and elderly people for telemedical and homecare services". *1st WSEAS International Conference on Biomedical Electronics and Biomedical Informatics (BEBI '08)*, **2008**, 183–187.
113. C. Chen, C. Pomalaza-Raez. "IMPLEMENTING AND EVALUATING A WIRELESS BODY SENSOR SYSTEM FOR AUTOMATED PHYSIOLOGICAL DATA ACQUISITION AT HOME". *International Journal of Computer Science and Information Technology*, **2010**, 2(3), 24–38. DOI: 10.5121/ijcsit.2010.2303
114. P.S. Hall, Y. Hao. "Antennas and Propagation for Body-Centric Wireless Communications", Second edi Artech House, London, England, **2012**
115. C.C. Vassiliou, V.H. Liu, M.J. Cima. "Miniaturized, biopsy-implantable chemical sensor with wireless, magnetic resonance readout". *Lab Chip*, Royal Society of Chemistry, **2015**, 15(17), 3465–3472. DOI: 10.1039/C5LC00546A
116. A. Guiseppi-Elie. "An implantable biochip to influence patient outcomes following trauma-induced hemorrhage". *Analytical and Bioanalytical Chemistry*, **2011**, 399(1), 403–419. DOI: 10.1007/s00216-010-4271-x
117. A. Cavallini. "An implantable biosensor array for personalized therapy applications", {É}COLE POLYTECHNIQUE F{É}D{É}RALE DE LAUSANNE, **2013**
118. V.V.A.M. Schreurs, G. Schaafsma. "Lactic acid and lactates". *Nutrafoods*, **2010**, 9(1), 7–16. DOI: 10.1007/BF03223326
119. G. Chen, H. Ghaed, R. Haque, M. Wieckowski, Y. Kim, G. Kim, D. Fick, D. Kim, M. Seok, ... D. Sylvester. "A cubic-millimeter energy-autonomous wireless intraocular pressure monitor", In 2011 IEEE International Solid-State Circuits Conference; IEEE, **2011**, 310–312. DOI: 10.1109/ISSCC.2011.5746332
120. B. Bradford, W. Krautschneider, D. Schr. "Wireless Power and Data Transmission for a Pressure Sensing Medical Implant". In *Tagungsband "BMT2010"*, **2010**, 1–4.
121. J. Holmberg. "Battery-Less Wireless Instrumented Tibial Tray", UNIVERSITY OF MINNESOTA, **2011**

122. R. Sicree, J. Shaw, P.Z. Baker, I.H. and D. Institute. "The Global Burden: Diabetes and Impaired Glucose Tolerance". *IDF Diabetes Atlas fourth edition*, fourth edi **2010**, 1–105. DOI: 10.1097/01.hjr.0000368191.86614.5a
123. Y.J. Li, C.C. Lu. "A Novel Scheme and Evaluations on a Long-Term and Continuous Biosensor Platform Integrated with a Dental Implant Fixture and Its Prosthetic Abutment". *Sensors*, **2015**, 15(10), 24961–24976. DOI: 10.3390/s151024961
124. S. Afroz, S.W. Thomas, G. Mumcu, S.E. Saddow. "Implantable SiC based RF antenna biosensor for continuous glucose monitoring", In 2013 IEEE SENSORS; IEEE, **2013**, 1–4. DOI: 10.1109/ICSENS.2013.6688379
125. R. Schlierf, U. Horst, M. Ruhl, T. Schmitz-Rode, W. Mokwa, U. Schnakenberg. "A fast telemetric pressure and temperature sensor system for medical applications". *Journal of Micromechanics and Microengineering*, **2007**, 17(7), S98--S102. DOI: 10.1088/0960-1317/17/7/S06
126. W.H. Ko, M.R. Neuman. "Implant Biotelemetry and Microelectronics". *Science*, Intergovernmental Panel on Climate Change, Ed.; Cambridge University Press, Cambridge, **1967**, 156(3773), 351–360. DOI: 10.1126/science.156.3773.351
127. Fraunhofer-Gesellschaft. "Sensor In Artery Measures Blood Pressure". **2009**, <https://www.sciencedaily.com/releases/2009/01/090119081512.htm> [Last access: Sep 12 2016]
128. S. kyun Kang, R.K.J. Murphy, S.W. Hwang, S.H.S.M. Lee, D. V. Harburg, N.A. Krueger, J. Shin, P. Gamble, H. Cheng, ... J.A. Rogers. "Bioresorbable silicon electronic sensors for the brain". *Nature*, Nature Publishing Group, **2016**, 530(7588), 71–76. DOI: 10.1038/nature16492
129. T. Kakaday, a W. Hewitt, N.H. Voelcker, J.S.J. Li, J.E. Craig. "Advances in telemetric continuous intraocular pressure assessment". *The British journal of ophthalmology*, **2009**, 93(8), 992–996. DOI: 10.1136/bjo.2008.144261
130. H. Mahmoud, N. Khaled, L. Marnat, O. Mh, M. Arsalan, K. Salama, A. Shamim, L. Marnat, M.H. Ouda, ... A. Shamim. "Repository On-Chip Implantable Antennas for Wireless Power and Data Transfer in a Glaucoma-Monitoring SoC On-chip Implantable Antennas for Wireless Power and Data Transfer in a Glaucoma Monitoring SoC". **2013**, DOI: 10.1109/LAWP.2013.2240253.Post-print
131. T. Ohki, K. Ouriel, P.G. Silveira, B. Katzen, R. White, F. Criado, E. Diethrich. "Initial results of wireless pressure sensing for endovascular aneurysm repair: The APEX Trial—Acute Pressure Measurement to Confirm Aneurysm Sac EXclusion". *Journal of Vascular Surgery*, **2007**, 45(2), 236–242. DOI: 10.1016/j.jvs.2006.09.060
132. M.A. Fonseca, M.G. Allen, J. Kroh, J. White. "Flexible wireless passive pressure sensors for biomedical applications". *Solid-State Sensor, Actuator, and Microsystems Workshop*, **2006**, (1), 37–42. DOI: 0-9640024-6-9/hh2006
133. E.C. Benzel, M. Kayanja, A. Fleischman, S. Roy. "Spine Biomechanics : Fundamentals and Future". *Spine Biomechanics: Fundamentals and Future*, **2006**, 53, 98–105.
134. P. Damm. ", Loading of total hip joint replacements – In vivo measurements with instrumented hip implants """, Technischen Universit{ä}t Berlin, **2014**
135. C.E. Carlson, R.W. Mann, W.H. Harris. "A Radio Telemetry Device for Monitoring Cartilage Surface Pressures in the Human Hip". *IEEE Transactions on Biomedical Engineering*, **1974**, BME-21(4), 257–264. DOI: 10.1109/TBME.1974.324311

References

136. A. Vena, B. Sorli, B. Charlot, S. Naudi. "An RFID-based implant for identification and pressure sensing of orthopedic prosthesis", In 2015 1st URSI Atlantic Radio Science Conference (URSI AT-RASC); IEEE, **2015**, 1. DOI: 10.1109/URSI-AT-RASC.2015.7303024
137. M. Simoncini. "Design and integration of an instrumented knee prosthesis", ÉCOLE POLYTECHNIQUE FÉDÉRALE DE LAUSANNE, **2014**
138. C.W. Colwell, D.D. D'Lima, D.D. D'Lima. "The Electronic Knee". In Total Knee Arthroplasty; Springer-Verlag, Berlin/Heidelberg, **2005**, 282–287. DOI: 10.1007/3-540-27658-0_45
139. D.D. D'Lima, B.J. Fregly, C.W. Colwell, C.W. Colwell Jr., C.W. Colwell. "Implantable sensor technology: measuring bone and joint biomechanics of daily life in vivo." *Arthritis research & therapy*, **2013**, 15(1), 203. DOI: 10.1186/ar4138
140. W.A. Hodge, R.S. Fijan, K.L. Carlson, R.G. Burgess, W.H. Harris, R.W. Mann. "Contact pressures in the human hip joint measured in vivo." *Proceedings of the National Academy of Sciences of the United States of America*, **1986**, 83, 2879–2883.
141. J.C.K. Fong. "Wireless MEMS drug delivery device enabled by a micromachined Nitinol actuator as a pumping mechanism by", The University of British Columbia, **2014**
142. M.J. Nitsch, U. V. Banakar. "Implantable Drug Delivery Devices". *Journal of Biomaterials Applications*, **2002**, 8, 247–284.
143. R. Farra, N.F. Sheppard, L. McCabe, R.M. Neer, J.M. Anderson, J.T. Santini, M.J. Cima, R. Langer. "First-in-Human Testing of a Wirelessly Controlled Drug Delivery Microchip". *Science Translational Medicine*, **2012**, 4(122), 1–10. DOI: 10.1126/scitranslmed.3003276
144. M. Zaki, S.K. Patil, D.T. Baviskar, D.K. Jain. "Implantable Drug Delivery System : A Review". *International Journal of PharmTech Research*, **2012**, 4(1), 280–292.
145. H. Hafezi, T.L. Robertson, G.D. Moon, K.-Y.Y. Au-Yeung, M.J. Zdeblick, G.M. Savage. "An Ingestible Sensor for Measuring Medication Adherence". *IEEE Transactions on Biomedical Engineering*, **2015**, 62(1), 99–109. DOI: 10.1109/TBME.2014.2341272
146. K.Y. Au-Yeung, T. Robertson, H. Hafezi, G. Moon, L. DiCarlo, M. Zdeblick, G. Savage. "A networked system for self-management of drug therapy and wellness". *Wireless Health 2010*, **2010**, 1–9. DOI: 10.1145/1921081.1921083
147. S. Rodriguez, S. Ollmar, M. Waqar, A. Rusu. "A Batteryless Sensor ASIC for Implantable Bio-impedance Applications". *IEEE Transactions on Biomedical Circuits and Systems*, **2015**, 10(3), 533–544. DOI: 10.1109/TBCAS.2015.2456242
148. A. Mercanzini, P. Colin, J.-C. Bensadoun, A. Bertsch, P. Renaud. "In Vivo Electrical Impedance Spectroscopy of Tissue Reaction to Microelectrode Arrays". *IEEE Transactions on Biomedical Engineering*, **2009**, 56(7), 1909–1918. DOI: 10.1109/TBME.2009.2018457
149. S.P. Lacour, S. Benmerah, E. Tarte, J. FitzGerald, J. Serra, S. McMahon, J. Fawcett, O. Graudejus, Z. Yu, B. Morrison. "Flexible and stretchable micro-electrodes for in vitro and in vivo neural interfaces". *Medical & Biological Engineering & Computing*, **2010**, 48(10), 945–954. DOI: 10.1007/s11517-010-0644-8
150. J.C. Williams, J.A. Hippensteel, J. Dilgen, W. Shain, D.R. Kipke. "Complex impedance spectroscopy for monitoring tissue responses to inserted neural implants". *Journal of Neural Engineering*, **2007**, 4(4), 410–423. DOI: 10.1088/1741-2560/4/4/007

151. N. Alba, Z. Du, K. Catt, T. Kozai, X. Cui. "In Vivo Electrochemical Analysis of a PEDOT/MWCNT Neural Electrode Coating". *Biosensors*, **2015**, 5(4), 618–646. DOI: 10.3390/bios5040618
152. W. Dong, E.S. Olson. "In Vivo Impedance of the Gerbil Cochlear Partition at Auditory Frequencies". *Biophysical Journal*, Biophysical Society, **2009**, 97(5), 1233–1243. DOI: 10.1016/j.bpj.2009.05.057
153. T.R. Deer. "Atlas of Implantable Therapies for Pain Management", Springer New York, New York, NY, **2011**, DOI: 10.1007/978-0-387-88567-4
154. N. Horizon, I. Centre. "Freedom Spinal Cord Stimulator System for chronic back and leg pain". *Horizon Scanning Research & Intelligence Centre*, **2015**, (July)
155. M.A. Kemler, H.C.W. de Vet, G.A.M. Barendse, F.A.J.M. van den Wildenberg, M. van Kleef. "Effect of spinal cord stimulation for chronic complex regional pain syndrome Type I: five-year final follow-up of patients in a randomized controlled trial". *Journal of Neurosurgery*, **2008**, 108(2), 292–298. DOI: 10.3171/JNS/2008/108/2/0292
156. D. De Ridder, M. Plazier, N. Kamerling, T. Menovsky, S. Vanneste. "Burst Spinal Cord Stimulation for Limb and Back Pain". *World Neurosurgery*, Elsevier Inc, **2013**, 80(5), 642–649.e1. DOI: 10.1016/j.wneu.2013.01.040
157. J.M. DeSantana, D.M. Walsh, C. Vance, B.A. Rakel, K.A. Sluka. "Effectiveness of Transcutaneous Electrical Nerve Stimulation for Treatment of Hyperalgesia and Pain". *Curr Rheumatol Rep*, **2008**, 10(6), 492–499.
158. E.B. Plow, A. Pascual-Leone, A. Machado. "Brain stimulation in the treatment of chronic neuropathic and non-cancerous pain.". *The journal of pain : official journal of the American Pain Society*, Elsevier Ltd, **2012**, 13(5), 411–424. DOI: 10.1016/j.jpain.2012.02.001
159. D. Khurana, S. Kaul, N.M. Bornstein. "augmentation of cerebral blood flow trial 1: a pilot study evaluating the safety and effectiveness of the Ischaemic Stroke System for treatment of acute ischaemic stroke". {...} *Journal of Stroke*, **2009**, 4(December), 480–485.
160. J. Schoenen, R.H. Jensen, M. Lantéri-Minet, M.J. a Láinez, C. Gaul, A.M. Goodman, A. Caparso, A. May. "Stimulation of the sphenopalatine ganglion (SPG) for cluster headache treatment. Pathway CH-1: a randomized, sham-controlled study.". *Cephalalgia : an international journal of headache*, **2013**, 33(10), 816–830. DOI: 10.1177/0333102412473667
161. D.S. Kern, R. Kumar. "Deep brain stimulation.". *The neurologist*, **2007**, 13(5), 237–252. DOI: 10.1097/NRL.0b013e3181492c48
162. W.H. Li. "Wearable computer vision systems for a cortical visual prosthesis". *Proceedings of the IEEE International Conference on Computer Vision*, **2013**, 428–435. DOI: 10.1109/ICCVW.2013.63
163. L.S. Wright, M.J. Phillips, I. Pinilla, D. Hei, D. Gamm. "Restoring Vision to the Blind The Lasker / IRRF Initiative for Innovation in Vision Science". *Exp Eye Res*, **2014**, 161(72), 123.
164. R.C. Pinnell, J. Dempster, J. Pratt. "Miniature wireless recording and stimulation system for rodent behavioural testing". *Journal of Neural Engineering*, IOP Publishing, **2015**, 12(6), 66015. DOI: 10.1088/1741-2560/12/6/066015
165. Ming Yin, D.A. Borton, J. Aceros, W.R. Patterson, A. V. Nurmikko. "A 100-Channel Hermetically Sealed Implantable Device for Chronic Wireless Neurosensing Applications". *IEEE Transactions on Biomedical Circuits and Systems*, **2013**, 7(2), 115–128. DOI: 10.1109/TBCAS.2013.2255874

References

166. M.A.L. Nicolelis, M.A. Lebedev. "Principles of neural ensemble physiology underlying the operation of brain-machine interfaces". *Nature reviews. Neuroscience*, Nature Publishing Group, **2009**, *10*(7), 530–540. DOI: 10.1038/nrn2653
167. V. Gilja, C. Pandarinath, C.H. Blabe, P. Nuyujukian, J.D. Simeral, A. a Sarma, B.L. Sorice, J. a Perge, B. Jarosiewicz, ... J.M. Henderson. "Clinical translation of a high-performance neural prosthesis". *Nature medicine*, **2015**, *21*(10), 6–8. DOI: 10.1038/nm.3953
168. M. Yin, D.A. Borton, J. Komar, N. Agha, Y. Lu, H. Li, J. Laurens, Y. Lang, Q. Li, ... A. V. Nurmikko. "Wireless neurosensor for full-spectrum electrophysiology recordings during free behavior". *Neuron*, **2014**, *84*(6), 1170–1182. DOI: 10.1016/j.neuron.2014.11.010
169. S. Musallam, M.J. Bak, P.R. Troyk, R.A. Andersen. "A floating metal microelectrode array for chronic implantation". *Journal of Neuroscience Methods*, **2007**, *160*(1), 122–127. DOI: 10.1016/j.jneumeth.2006.09.005
170. R.J. Vetter, J.C. Williams, J.F. Hetke, E.A. Nunamaker, D.R. Kipke. "Chronic neural recording using silicon-substrate microelectrode arrays implanted in cerebral cortex". *IEEE Transactions on Biomedical Engineering*, **2004**, *51*(6), 896–904. DOI: 10.1109/TBME.2004.826680
171. M.A.L. Nicolelis, D. Dimitrov, J.M. Carmena, R. Crist, G. Lehew, J.D. Kralik, S.P. Wise. "Chronic, multisite, multielectrode recordings in macaque monkeys". *Pnas*, **2003**, *100*(19), 11041–11046. DOI: 10.1073/pnas.1934665100
172. M.A.M. Freire, J. Faber, N.A.M. Lemos, J.R. Santos, P.F. Cavalcanti, R.H. Lima, E. Morya. "Distribution and Morphology of Calcium-Binding Proteins Immunoreactive Neurons following Chronic Tungsten Multielectrode Implants". *PloS one*, **2015**, *10*(6), e0130354. DOI: 10.1371/journal.pone.0130354
173. J. Wang, F. Wagner, D.A. Borton, J. Zhang, I. Ozden, R.D. Burwell, A. V Nurmikko, R. van Wagenen, I. Diester, K. Deisseroth. "Integrated device for combined optical neuromodulation and electrical recording for chronic in vivo applications.". *Journal of neural engineering*, **2012**, *9*(1), 16001. DOI: 10.1088/1741-2560/9/1/016001
174. S. Suner, M.R. Fellows, C. Vargas-Irwin, K. Nakata, J.P. Donoghue. "Reliability of signals from a chronically implanted, silicon-gated electrode array in non-human primate primary motor cortex". *IEEE Trans Neural Syst Rehabil Eng*, **2005**, *13*(4), 524–541. DOI: 10.1109/TNSRE.2005.857687
175. R.E. Isaacs, D.J. Weber, A.B. Schwartz. "Work toward real-time control of a cortical neural prosthesis". *IEEE Transactions on Rehabilitation Engineering*, **2000**, *8*(2), 196–198. DOI: 10.1109/86.847814
176. H. Miranda, V. Gilja, C. a Chestek, K. V Shenoy, T.H. Meng. "HermesD: A High-Rate Long-Range Wireless Transmission System for Simultaneous Multichannel Neural Recording Applications". *IEEE Transactions on Biomedical Circuits and Systems*, **2010**, *4*(3), 181–191. DOI: 10.1109/TBCAS.2010.2044573
177. C.A. Chestek, S.S. Member, V. Gilja, P. Nuyujukian, S.S. Member, R.J. Kier, S.S. Member, F. Solzbacher, S.I. Ryu, ... S.S. Member. "HermesC : Low-Power Wireless Neural Recording System for Freely Moving Primates". *330 IEEE TRANSACTIONS ON NEURAL SYSTEMS AND REHABILITATION ENGINEERING*, **2009**, *17*(4), 330–338.
178. G. Santhanam, M.D. Linderman, V. Gilja, A. Afshar, S.I. Ryu, T.H. Meng, K. V. Shenoy. "HermesB: A continuous neural recording system for freely behaving primates". *IEEE Transactions on Biomedical Engineering*, **2007**, *54*(11), 2037–2050. DOI: 10.1109/TBME.2007.895753

179. F. Sauter-Starace, G. Charvet, A.-L. Benabid. "Implantable device of the neural interface type and associated method" Issued **2013**, 1–13.
180. S.-I. Il Chang, K. AlAshmouny, M. McCormick, Y.-C.C. Chen, E. Yoon. "BioBolt: A minimally-invasive neural interface for wireless epidural recording by intra-skin communication". *2011 Symposium on VLSI Circuits - Digest of Technical Papers*, **2011**, 146–147.
181. Y.-K. Song, Y.-K. Song, D. a Borton, D. a Borton, S. Park, S. Park, W.R. Patterson, W.R. Patterson, C.W. Bull, ... a V Nurmikko. "Active microelectronic neurosensor arrays for implantable brain communication interfaces.". *IEEE transactions on neural systems and rehabilitation engineering: a publication of the IEEE Engineering in Medicine and Biology Society*, **2009**, 17(4), 339–345. DOI: 10.1109/TNSRE.2009.2024310
182. T. Tsaousides, W. a Gordon. "Cognitive rehabilitation following traumatic brain injury: assessment to treatment.". *The Mount Sinai journal of medicine, New York*, **2009**, 76(2), 173–181. DOI: 10.1002/MSJ
183. A. Ivorra, L. Becerra-Fajardo, Q. Castellví. "In vivo demonstration of injectable microstimulators based on charge-balanced rectification of epidermally applied currents". *Journal of Neural Engineering*, IOP Publishing, **2015**, 12(6), 66010. DOI: 10.1088/1741-2560/12/6/066010
184. E.C. Leuthardt, G. Schalk, J.R. Wolpaw, J.G. Ojemann, D.W. Moran. "A brain-computer interface using electrocorticographic signals in humans.". *Journal of neural engineering*, **2004**, 1(2), 63–71. DOI: 10.1088/1741-2560/1/2/001
185. D.-H. Kim, J. Viventi, J.J. Amsden, J. Xiao, L. Vigeland, Y.-S. Kim, J.A. Blanco, B. Panilaitis, E.S. Frechette, ... J.A. Rogers. "Dissolvable films of silk fibroin for ultrathin conformal bio-integrated electronics". *Nature Materials*, **2010**, 9(6), 511–517. DOI: 10.1038/nmat2745
186. J.T. Mortimer, N. Bhadra. "PERIPHERAL NERVE AND MUSCLE STIMULATION". In *Neuroprosthetics: Theory and Practice*; K.W. Horch, G.S. Dhillon, Eds.; World Scientific Publishing Co., Singapore, **2004**, 638–682. DOI: 10.1142/9789812561763_0020
187. K.P. Hoffmann, K.P. Koch, T. Doerge, S. Micera. "New technologies in manufacturing of different implantable microelectrodes as an interface to the peripheral nervous system". *Proceedings of the First IEEE/RAS-EMBS International Conference on Biomedical Robotics and Biomechatronics, 2006, BioRob 2006*, **2006**, 2006(February 2001), 414–419. DOI: 10.1109/BIOROB.2006.1639123
188. S.P. Lacour, R. Atta, J.J. FitzGerald, M. Blamire, E. Tarte, J. Fawcett. "Polyimide micro-channel arrays for peripheral nerve regenerative implants". *Sensors and Actuators, A: Physical*, **2008**, 147(2), 456–463. DOI: 10.1016/j.sna.2008.05.031
189. B. Ziaie, A. Member, M.D. Nardin, A.R. Coghlan, K. Najafi. "A Single-Channel Implantable Microstimulator for Functional Neuromuscular Stimulation". *IEEE TRANSACTIONS ON BIOMEDICAL ENGINEERING*, **1997**, 44(10), 909–920.
190. K.L. Montgomery, A.J. Yeh, J.S. Ho, V. Tsao, S. Mohan Iyer, L. Grosenick, E.A. Ferenczi, Y. Tanabe, K. Deisseroth, ... A.S.Y. Poon. "Wirelessly powered, fully internal optogenetics for brain, spinal and peripheral circuits in mice". *Nature Methods*, **2015**, 12(10), 969–974. DOI: 10.1038/nmeth.3536
191. C.T. Wentz, J.G. Bernstein, P. Monahan, A. Guerra, A. Rodriguez, E.S. Boyden. "A wirelessly powered and controlled device for optical neural control of freely-behaving animals.". *Journal of neural engineering*, **2011**, 8(4), 46021. DOI: 10.1088/1741-2560/8/4/046021

References

192. T. Kim, J.G. McCall, Y.H. Jung, X. Huang, E.R. Siuda, Y. Li, J. Song, Y.M. Song, H.A. Pao, ... M.R. Bruchas. "Injectable, Cellular-Scale Optoelectronics with Applications for Wireless Optogenetics". *Science*, **2013**, 340(6129), 211–216. DOI: 10.1126/science.1232437
193. D. Schwarz, M. Lebedev, T. Hanson, D. Dimitrov, G. Lehew, J. Meloy, S. Rajangam, V. Subramanian, P. Ifft, ... M. Nicolelis. "Chronic, wireless recordings of large-scale brain activity in freely moving rhesus monkeys". *Nature Methods*, Nature Publishing Group, **2014**, 11(6), 670–676. DOI: 10.1038/nmeth.2936
194. D.A. Lobel, K.H. Lee. "Brain machine interface and limb reanimation technologies: Restoring function after spinal cord injury through development of a bypass system". *Mayo Clinic Proceedings*, Elsevier Inc, **2014**, 89(5), 708–714. DOI: 10.1016/j.mayocp.2014.02.003
195. M. Sun, M. Mickle, W. Liang, Q. Liu, R.J. Scwabassi. "Data communication between brain implants and computer". *IEEE Transactions on Neural Systems and Rehabilitation Engineering*, **2003**, 11(2), 189–192. DOI: 10.1109/TNSRE.2003.814421
196. B.C. Towe, P.J. Larson, D.W. Gulick. "A Microwave Powered Injectable Neurostimulator". *34th Annual International Conference of the IEEE EMBS*, **2012**, 5006–5009.
197. T. Cameron, G.E. Loeb, R.A. Peck, J.H. Schulman, P. Strojnik, P.R. Troyk, L. Member, P. Strojnik, P.R. Troyk, S. Member. "Micromodular implants to provide electrical stimulation of paralyzed muscles and limbs". *IEEE Transactions on Biomedical Engineering*, **1997**, 44(9), 781–790. DOI: 10.1109/10.623047
198. C. Libedinsky, R. So, Z. Xu, T.K. Kyar, D. Ho, C. Lim, L. Chan, Y. Chua, L. Yao, ... S.C. Yen. "Independent mobility achieved through a wireless brain-machine interface". *PLoS ONE*, **2016**, 11(11), 1–13. DOI: 10.1371/journal.pone.0165773
199. A.O.G. Barbosa, D.Z. Freitas. "Implementation of a Wheelchair Control Using a Four-Command Brain Computer Interface". *ABCM Symposium Series in Mechatronics*, **2013**, 6, 120–131.
200. L.R. Hochberg, D. Bacher, B. Jarosiewicz, N.Y. Masse, J.D. Simeral, J. Vogel, S. Haddadin, J. Liu, S.S. Cash, ... J.P. Donoghue. "Reach and grasp by people with tetraplegia using a neurally controlled robotic arm". *Nature*, Nature Publishing Group, **2012**, 485(7398), 372–375. DOI: 10.1038/nature11076
201. M.A. Lebedev, M. a. L.L. Nicolelis, M. a.L. Nicolelis, M. a. L.L. Nicolelis. "Brain-machine interfaces: past, present and future". *Trends in Neurosciences*, **2006**, 29(9), 536–546. DOI: 10.1016/j.tins.2006.07.004
202. D. Celik. "Computation of the Cell Phone-Induced SAR Distribution in a 3D Multi-Layered Model of the Human Head / Brain Using ANSYS HFSS". *Ozen Engineering*, **2013**, 1–16.
203. P. Soontornpipit. "Effects of radiation and SAR from wireless implanted medical devices on the human body". *Journal of the Medical Association of Thailand*, **2012**, 95(9), S189–S197.
204. P.A. Bottomley, E.R. Andrew. "RF magnetic field penetration, phase shift and power dissipation in biological tissue: implications for NMR imaging". *Physics in medicine and biology*, **1978**, 23(4), 630–643. DOI: 10.1088/0031-9155/23/4/006
205. S. Mutashar, M. Hannan, S. Samad, A. Hussain. "Analysis and Optimization of Spiral Circular Inductive Coupling Link for Bio-Implanted Applications on Air and within Human Tissue". *Sensors*, **2014**, 14(7), 11522–11541. DOI: 10.3390/s140711522
206. T.G. Mahn. "Wireless Medical Technologies: Navigating Government Regulation in the New Medical Age I", Washington, D.C, **2013**

207. J.L. Abita, W. Schneider. "Transdermal optical communications". *Johns Hopkins APL Technical Digest (Applied Physics Laboratory)*, **2004**, 25(3), 261–268.
208. J.E. Ferguson, a D. Redish. "Wireless communication with implanted medical devices using the conductive properties of the body.". *Expert review of medical devices*, **2011**, 8(4), 427–433. DOI: 10.1586/erd.11.16
209. M.N. Islam, M.R. Yuce. "Review of Medical Implant Communication System (MICS) band and network". *ICT Express*, **2016**, 2(4), 188–194. DOI: 10.1016/j.ict.2016.08.010
210. J.A. Stine, D.L. Portigal. "An Introduction to Spectrum Management", The MITRE Corporation, **2004**
211. D.G. Messerschmitt. "How Digital Communication Works". *University of California*, **1999**, 1–6.
212. M. Loy, R. Karingattil, L. Williams. "ISM-Band and Short Range Device Regulatory Compliance Overview". *Texas Instruments*, **2005**, SWRA048, 1–17.
213. T.G. Mahn, K.A. Barritt. "Wireless Medical Technologies: Navigating Government Regulation in the New Medical Age", Fish's Regulatory & Government Affairs Group, Washington, USA, **2016**
214. N. Vidal, S. Curto, J.M.L. Villegas, J. Sieiro, F.M. Ramos. "Detuning Study of Implantable Antennas Inside the Human Body". *Progress In Electromagnetics Research*, **2012**, 124, 265–283.
215. B. Rajeev. "Handbook of Electromagnetics Engineering", Marcel Dekker Inc., New York, USA, **2004**
216. D.Andreuccetti, R.Fossi, C.Petrucci. "An Internet resource for the calculation of the dielectric properties of body tissues in the frequency range 10 Hz - 100 GHz". **1997**, <http://niremf.ifac.cnr.it/tissprop/> [Last access: Jan 1 2016]
217. P.A. Hasgall, E. Neufeld, M.C. Gosselin, A. Klingenböck, N. Kuster, N. Kuste, P. Hasgall, M. Gosselin. "IT'IS Database for thermal and electromagnetic parameters of biological tissues". **2015**, DOI: 10.13099/VIP21000-03-0. www.itis.ethz.ch/database [Last access: Nov 1 2016]
218. V. Komarov, S. Wang, J. Tang. "Permittivity and Measurements". *Encyclopedia of RF and Microwave Engineering*, **2005**, 3693–3711. DOI: 10.1002/0471654507.eme308
219. D.H. Gadani, V.A. Rana, S.P. Bhatnagar, A.N. Prajapati, A.D. Vyas. "Effect of salinity on the dielectric properties of water". *Indian Journal of Pure & Applied Physics*, **2012**, 50, 405–410.
220. A. Boughriet, Z. Wu, H. McCann, L.E. Davis. "The Measurement of Dielectric Properties of Liquids at Microwave Frequencies Using Open-ended Coaxial Probes". *World Congress on Industrial Process Tomography*, **1999**, 2(2), 318–322.
221. Y. Lasne, P. Paillou, A. Freeman, T. Farr, K.C. McDonald, G. Ruffie, J.M. Malezieux, B. Chapman, F. Demontoux. "Effect of Salinity on the Dielectric Properties of Geological Materials: Implication for Soil Moisture Detection by Means of Radar Remote Sensing". *IEEE Transactions on Geoscience and Remote Sensing*, **2008**, 46(6), 1674–1688. DOI: 10.1109/TGRS.2008.916220
222. M. Wiegel, A. Reske, R. Hennebach, F. Schmidt, T. Elias, H. Gupta, D. Olthoff. "Anterior sciatic nerve block - New landmarks and clinical experience". *Acta Anaesthesiologica Scandinavica*, **2005**, 49(4), 552–557. DOI: 10.1111/j.1399-6576.2005.00675.x
223. J.E. Chelly, L. Delaunay. "A new anterior approach to the sciatic nerve block". *Anesthesiology*, **1999**, 91(6), 1655–1660.

References

224. R.A. McCahon, N.M. Bedford. "Peripheral nerve block at the elbow and wrist". *Continuing Education in Anaesthesia, Critical Care and Pain*, **2007**, 7(2), 42–44. DOI: 10.1093/bjaceaccp/mkm005
225. S.L. Orebaugh, B.A. Williams. "Brachial Plexus Anatomy: Normal and Variant". *The Scientific World JOURNAL*, **2009**, 9, 300–312. DOI: 10.1100/tsw.2009.39
226. E.Y. Chow, Y. Ouyang, B. Beier, W.J. Chappell, P.P. Irazoqui. "Evaluation of cardiovascular stents as antennas for implantable wireless applications". *IEEE Transactions on Microwave Theory and Techniques*, **2009**, 57(10), 2523–2532. DOI: 10.1109/TMTT.2009.2029954
227. B. Godara, K.S. Nikita. "Wireless Mobile Communication and Healthcare", Springer, Berlin, Heidelberg, **2013**, DOI: 10.1007/978-3-642-37893-5
228. Z. Duan, Y.X. Guo, M. Je, D.L. Kwong. "Design and in vitro test of a differentially fed dual-band implantable antenna operating at MICS and ISM Bands". *IEEE Transactions on Antennas and Propagation*, **2014**, 62(5), 2430–2439. DOI: 10.1109/TAP.2014.2309130
229. A. Kiourti, K.A. Psathas, J.R. Costa, C.A. Fernandes, K.S. Nikita. "Dual-band implantable antennas for medical telemetry: a fast design methodology and validation for intra-cranial pressure monitoring". *Progress In Electromagnetics Research*, **2013**, 141, 161–183. DOI: 10.2528/PIER13051706
230. L. Xu, M. Meng, H. Ren, Y. Chan. "Radiation characteristics of ingestible wireless devices in human intestine following radio frequency exposure at 430, 800, 1200, and 2400 MHz". *IEEE Transactions on Antennas and Propagation*, **2009**, 57(8), 2418–2428. DOI: 10.1109/TAP.2010.2046873
231. A. Kiourti, K.S. Nikita. "A Review of Implantable Patch Antennas for Biomedical Telemetry: Challenges and Solutions". *IEEE Antennas and Propagation Magazine*, **2012**, 54(3), 210–228. DOI: 10.1109/MAP.2012.6293992
232. J.L. Volakis, C.-C. Chen, K. Fujimoto. "Small Antennas: Miniaturization Techniques & Applications", McGrawHill, United States of America, **2010**
233. R. Alrawashdeh, Y. Huang, P. Cao. "A conformal U-shaped loop antenna for biomedical applications". *Antennas and Propagation (EuCAP), 2013 7th European Conference on*, **2013**, 157–160.
234. E.G. Lim, J.C. Wang, Z. Wang, G. Juans, T. Tillo, K.L. Man. "Wireless Capsule Antennas". *Proceedings of the International MultiConference of Engineers and Computer Scientists (IMECS 2013)*, **2013**, 2, 13–16.
235. S.R. Best. "A Discussion on Electrically Small Antennas Loaded with High Permittivity and Permeability Materials". *The MITRE Corporation*, **2011**, 1–4.
236. H. Bahrami, S.A. Mirbozorgi, L.A. Rusch, B. Gosselin. "Biological channel modeling and implantable UWB antenna design for neural recording systems". *IEEE Transactions on Biomedical Engineering*, **2015**, 62(1), 88–98. DOI: 10.1109/TBME.2014.2339836
237. M. Gustafsson, L. Jonsson. "Stored Electromagnetic Energy and Antenna Q". *Progress In Electromagnetics Research*, **2015**, 150, 13–27.
238. A. Kiourti, K.S. Nikita. "Miniature Scalp-Implantable Antennas for Telemetry in the MICS and ISM Bands: Design, Safety Considerations and Link Budget Analysis". *IEEE Transactions on Antennas and Propagation*, **2012**, 60(8), 3568–3575. DOI: 10.1109/TAP.2012.2201078

239. Y. Jin, J. Tak, J. Choi. "Broadband hybrid water antenna for ISM-band ingestible capsule endoscope systems", In 2016 International Workshop on Antenna Technology (iWAT); IEEE, **2016**, 82–85. DOI: 10.1109/IWAT.2016.7434808
240. K. Okabe, H.P. Jeewan, S. Yamagiwa, T. Kawano, M. Ishida, I. Akita. "Co-Design Method and Wafer-Level Packaging Technique of Thin-Film Flexible Antenna and Silicon CMOS Rectifier Chips for Wireless-Powered Neural Interface Systems". *Sensors*, **2015**, 15(12), 31821–31832. DOI: 10.3390/s151229885
241. Ho-Yu Lin, M. Takahashi, K. Saito, K. Ito. "Development of UHF implanted RFID antenna for medical/health-care applications". *2011 30th URSI General Assembly and Scientific Symposium*, IEEE, **2011**, 1, 1–4. DOI: 10.1109/URSIGASS.2011.6051334
242. M.H. Ghaed, G. Chen, R.U. Haque, M. Wieckowski, Y. Kim, G. Kim, Y. Lee, I. Lee, D. Fick, ... D. Sylvester. "Circuits for a cubic-millimeter energy-autonomous wireless intraocular pressure monitor". *IEEE Transactions on Circuits and Systems I: Regular Papers*, **2013**, 60(12), 3152–3162. DOI: 10.1109/TCSI.2013.2265973
243. A. Ibraheem, M. Manteghi. "Performance of an Implanted Electrically Coupled Loop Antenna Inside Human Body". *Progress In Electromagnetics Research*, **2014**, 145, 195–202. DOI: 10.2528/PIER14022005
244. N.H. Ramli, M.R. Kamarudin, N.A. Samsuri, E.N. Ahyat, A.Y. Abdulrahman, M.F. Jamlos. "A 6.0GHz SMALL PRINTED MONOPOLE ANTENNA FOR WIRELESS IMPLANTABLE BODY AREA NET- WORK APPLICATIONS". *Progress In Electromagnetics Research C*, **2013**, 41, 189–200.
245. W. Xia, K. Saito, M. Takahashi, K. Ito. "Performances of an implanted cavity slot antenna embedded in the human arm". *IEEE Transactions on Antennas and Propagation*, **2009**, 57(4), 894–899. DOI: 10.1109/TAP.2009.2014579
246. J. Kim, Y. Rahmat-Samii. "Implanted antennas inside a human body: Simulations, designs, and characterizations". *IEEE Transactions on Microwave Theory and Techniques*, **2004**, 52(8), 1934–1943. DOI: 10.1109/TMTT.2004.832018
247. C.J.J. Sánchez-Fernández, O. Quevedo-Teruel, J. Requena-Carrión, L. Inclán-Sánchez, E. Rajo-Iglesias. "Dual-band microstrip patch antenna based on short-circuited ring and spiral resonators for implantable medical devices". *IET Microwaves, Antennas & Propagation*, **2010**, 4(8), 1048. DOI: 10.1049/iet-map.2009.0594
248. T.F. Chien, C.M. Cheng, H.C. Yang, C.H. Luo. "Develop implantable ceramic antennas with no superstrate", In 2010 IEEE Antennas and Propagation Society International Symposium; IEEE, **2010**, 1–4. DOI: 10.1109/APS.2010.5561745
249. H.C. Yang, T.F. Chien, C.M. Cheng, K.H. Chen. "Develop an Implantable CPW-Fed Antenna on the MgTa_{1.5}Nb_{0.5}O₆ Ceramic Substrate". *Key Engineering Materials*, **2010**, 434–435, 630–633. DOI: 10.4028/www.scientific.net/KEM.434-435.630
250. S.A. Kumar, T. Shanmuganantham. "Implantable CPW fed slot monopole antenna for biomedical applications", In 2012 IEEE International Conference on Computational Intelligence and Computing Research; IEEE, **2012**, 1–4. DOI: 10.1109/ICCIC.2012.6510204
251. H. Permana, Q. Fang, W.S.T. Rowe. "HERMETIC IMPLANTABLE ANTENNA INSIDE VITRE- OUS HUMOR SIMULATING FLUID". *Progress In Electromagnetics Research C*, **2013**, 133, 571–590.
252. K.A. Psathas, A. Kiourti, K.S. Nikita. "A Novel Conformal Antenna for Ingestible Capsule Endoscopy in the MedRadio Band". *Progress In Electromagnetics Research Symposium Proceedings*, **2013**, 1899–1902.

References

253. T. Houzen, M. Takahashi, K. Ito. "Implanted Antenna for an Artificial Cardiac Pacemaker System". *Progress In Electromagnetics Research Symposium 2007*, **2007**, 51–54.
254. Y. Ahmed, Y. Hao, C. Parini. "A 31.5 GHz Patch Antenna Design for Medical Implants". *International Journal of Antennas and Propagation*, **2008**, 2008(167980), 1–6. DOI: 10.1155/2008/167980
255. C. Liu, Y. Guo, S. Xiao. "Capacitively Loaded Circularly Polarized Implantable Patch Antenna for ISM-Band Biomedical Applications". *IEEE Transactions on Antennas and Propagation*, **2014**, PP(99), 1–1. DOI: 10.1109/TAP.2014.2307341
256. N.A. Aziz, N.R. Mohamad, M. Abu, A. Othman. "Design of ultra-wideband (UWB) implantable antenna for biomedical telemetry". **2016**, 11(5), 3249–3252.
257. M. Khabiri. "Design and Simulation of Implantable PIFA in Presence of ANSYS Human Body Model for Biomedical Telemetry Using ANSYS HFSS", Ozen Engineering Inc.,
258. S. Bhattacharjee, S. Maity, S.K. Metya, C.T. Bhunia. "Performance enhancement of implantable medical antenna using differential feed technique". *Engineering Science and Technology, an International Journal*, Elsevier B.V., **2016**, 19(1), 642–650. DOI: 10.1016/j.jestch.2015.09.001
259. M. Usluer, S.C. Basaran. "Dual band implantable antenna for biomedical applications", In 2016 URSI International Symposium on Electromagnetic Theory (EMTS); IEEE, **2016**, 528–529. DOI: 10.1109/URSI-EMTS.2016.7571445
260. S. Surapan, S. Kawdungta, H.-C. Yang, Chih-Kuang Wu. "Design of dual band implantable antenna for biomedical applications", In 2016 13th International Conference on Electrical Engineering/Electronics, Computer, Telecommunications and Information Technology (ECTI-CON); IEEE, **2016**, 1–4. DOI: 10.1109/ECTICon.2016.7561374
261. A. Kiourti, K.S. Nikita. "Implantable Antennas: A Tutorial on Design, Fabrication, and In Vitro/In Vivo Testing". *IEEE Microwave Magazine*, **2014**, 15(4), 77–91. DOI: 10.1109/MMM.2014.2308765
262. A. Sondas, M.H.B. Ucar. "An implantable microstrip antenna design for biomedical telemetry". *2013 International Conference on Electronics, Computer and Computation, ICECCO 2013*, **2013**, 3, 32–35. DOI: 10.1109/ICECCO.2013.6718221
263. R. Warty, M.R. Tofighi, U. Kawoos, A. Rosen. "Characterization of implantable antennas for intracranial pressure monitoring: Reflection by and transmission through a scalp phantom". *IEEE Transactions on Microwave Theory and Techniques*, **2008**, 56(10), 2366–2376. DOI: 10.1109/TMTT.2008.2004254
264. H. Li, Y. Guo, S. Xiao. "Broadband circularly polarised implantable antenna for biomedical applications". *Electronics Letters*, **2016**, 52(7), 504–506. DOI: 10.1049/el.2015.4445
265. C.-F. Tseng, S.-Y. Chang, P.-J. Chang, W.-S. Chen, J.-S. Lin, C.-H. Hsu. "An implanted antenna design for biomedical applications operating in MICS and ISM bands", In 2015 Asia-Pacific Microwave Conference (APMC); IEEE, **2015**, 1–3. DOI: 10.1109/APMC.2015.7413410
266. A. Kiourti, K.S. Nikita. "Miniaturization vs gain and safety considerations of implantable antennas for wireless biotelemetry", In Proceedings of the 2012 IEEE International Symposium on Antennas and Propagation; IEEE, **2012**, 1–2. DOI: 10.1109/APS.2012.6348100
267. P. Soontornpipit, C.M. Furse, Y.C. Chung. "Design of implantable microstrip antenna for communication with medical implants". *IEEE Transactions on Microwave Theory and Techniques*, **2004**, 52(8 II), 1944–1951. DOI: 10.1109/TMTT.2004.831976

268. T. Karacolak, R. Cooper, E. Topsakal. "Electrical properties of rat skin and design of implantable antennas for medical wireless telemetry". *IEEE Transactions on Antennas and Propagation*, **2009**, 57(9), 2806–2812. DOI: 10.1109/TAP.2009.2027197
269. K. Sayrafian-Pour, W.-B. Yang, J. Hagedorn, J. Terrill, K.Y. Yazdandoost. "A statistical path loss model for medical implant communication channels". *2009 IEEE 20th International Symposium on Personal, Indoor and Mobile Radio Communications*, **2009**, 2995–2999. DOI: 10.1109/PIMRC.2009.5449869
270. F. Merli, L. Bolomey, E. Meurville, K. Skrivervik. "Dual band antenna for subcutaneous telemetry applications", In 2010 IEEE Antennas and Propagation Society International Symposium; **2010**, 1–4. DOI: 10.1109/APS.2010.5562054
271. F. Merli, L. Bolomey, J.F. Zürcher, G. Corradini, E. Meurville, A.K. Skrivervik. "Design, realization and measurements of a miniature antenna for implantable wireless communication systems". *IEEE Transactions on Antennas and Propagation*, **2011**, 59(10), 3544–3555. DOI: 10.1109/TAP.2011.2163763
272. W. Huang, A. Kishk. "Embedded Spiral Microstrip Implantable Antenna". *International Journal of Antennas and Propagation*, **2011**, 2011, 1–6. DOI: 10.1155/2011/919821
273. A.K. Skrivervik, F. Merli. "Design strategies for implantable antennas", In 2011 IEEE Loughborough Antennas & Propagation Conference; **2011**, 1–5. DOI: 10.1109/LAPC.2011.6114011
274. F.J. Huang, C.M. Lee, C.L. Chang, L.K. Chen, T.C. Yo, C.H. Luo. "Rectenna application of miniaturized implantable antenna design for triple-band biotelemetry communication". *IEEE Transactions on Antennas and Propagation*, **2011**, 59(7), 2646–2653. DOI: 10.1109/TAP.2011.2152317
275. Haiyu Huang, K. Nieman, Ye Hu, D. Akinwande. "Electrically small folded ellipsoidal helix antenna for medical implant applications", In 2011 IEEE International Symposium on Antennas and Propagation (APSURSI); IEEE, **2011**, 769–771. DOI: 10.1109/APS.2011.5996826
276. J. Abadia, F. Merli, J.F. Zurcher, J.R. Mosig, A.K. Skrivervik. "3D-Spiral small antenna design and realization for biomedical telemetry in the MICS band". *Radioengineering*, **2009**, 18(4), 359–367.
277. K. Bazaka, M. Jacob. "Implantable Devices: Issues and Challenges". *Electronics*, **2012**, 2(1), 1–34. DOI: 10.3390/electronics2010001
278. K.A. Psathas, A. Kiourti, K.S. Nikita. "Biocompatibility of implantable antennas: Design and performance considerations". *8th European Conference on Antennas and Propagation, EuCAP 2014*, **2014**, 1566–1570. DOI: 10.1109/EuCAP.2014.6902083
279. F. Merli, S. Member, B. Fuchs, J.R. Mosig, A.K. Skrivervik. "The Effect of Insulating Layers on the Performance of Implanted Antennas". *IEEE Transactions on Antennas and Propagation*, **2011**, 59(1), 21–31. DOI: 10.1109/TAP.2010.2090465
280. L. Marnat, M.H. Ouda, M. Arsalan, K. Salama, A. Shamim. "On-Chip Implantable Antennas for Wireless Power and Data Transfer in a Glaucoma-Monitoring SoC". *IEEE Antennas and Wireless Propagation Letters*, **2012**, 11, 1671–1674. DOI: 10.1109/LAWP.2013.2240253
281. E.J. Smith, D. Makarov, S. Sanchez, V.M. Fomin, O.G. Schmidt. "Magnetic microhelix coil structures". *Physical Review Letters*, **2011**, 107(9), 97204. DOI: 10.1103/PhysRevLett.107.097204

References

282. A. Erentok, R.W. Ziolkowski. "Metamaterial-Inspired Efficient Electrically Small Antennas". **2008**, 56(3), 691–707.
283. S.S. Pattnaik, J.G. Joshi, S. Devi, M.R. Lohokare. "Electrically Small rectangular microstrip patch antenna loaded with metamaterial", In IEEE Proceedings of the 9th International Symposium on Antennas, Propagation and EM Theory; **2010**, 247–250. DOI: 10.1109/ISAPE.2010.5696445
284. H.R. Stuart, A. Pidwerbetsky. "Electrically small antenna elements using negative permittivity resonators". *IEEE Transactions on Antennas and Propagation*, **2006**, 54(6), 1644–1653. DOI: 10.1109/TAP.2006.875498
285. J.B. PENDRY. "Negative refraction". *Contemporary Physics*, **2004**, 45(3), 191–202. DOI: 10.1080/00107510902734771
286. S. Hrabar, G. Jankovic. "Experimental Investigation of Radiation Properties of Waveguides Filled with Uniaxial Single Negative Metamaterials", In 2005 IEEE 18th International Conference on Applied Electromagnetics and Communications; **2005**, 1–4. DOI: 10.1109/ICECOM.2005.204982
287. P. Ikonen. "Electrically small metamaterial-based antennas - have we seen any real practical benefits?". *3rd European Conference on Antennas and Propagation, 2009 (EuCAP 2009)*, **2009**, 1–4.
288. A. Kiourti, M. Christopoulou, S. Koulouridis, K.S. Nikita. "Design of a Novel Miniaturized Implantable PIFA for Biomedical Telemetry". In Lecture Notes of the Institute for Computer Sciences, Social-Informatics and Telecommunications Engineering; **2011**, 127–134. DOI: 10.1007/978-3-642-20865-2_17
289. P.P. Mercier, S. Bandyopadhyay, A.C. Lysaght, K.M. Stankovic, A.P. Chandrakasan. "A Sub-nW 2.4 GHz Transmitter for Low Data-Rate Sensing Applications". *IEEE Journal of Solid-State Circuits*, **2014**, 49(7), 1463–1474. DOI: 10.1109/JSSC.2014.2316237
290. K. Gosalia, M.S. Humayun, G. Lazzi. "Impedance matching and implementation of planar space-filling dipoles as intraocular implanted antennas in a retinal prosthesis". *IEEE Transactions on Antennas and Propagation*, **2005**, 53(8 I), 2365–2373. DOI: 10.1109/TAP.2005.852514
291. H. Mizuno, K. Ito, M. Takahashi, K. Saito. "A helical folded dipole antenna for implantable communication devices", In 2010 IEEE Antennas and Propagation Society International Symposium; IEEE, **2010**, 1–4. DOI: 10.1109/APS.2010.5561748
292. H. Mizuno, M. Takahashi, K. Saito, K. Ito. "Development of an implanted helical folded dipole antenna for 2.45 GHz applications". *Final Program and Book of Abstracts - iWAT 2010: 2010 International Workshop on Antenna Technology: Small Antennas, Innovative Structures and Materials*, **2010**, (1), 6–9. DOI: 10.1109/IWAT.2010.5464689
293. H. Mizuno, M. Takahashi, K. Saito, N. Haga, K. Ito. "Design of a helical folded dipole antenna for biomedical implants". *Proceedings of the 5th European Conference on Antennas and Propagation (EUCAP)*, **2011**, 1, 3484–3487.
294. Basari, D. Zakaria, F.Y. Zulkifli, E.T. Rahardjo. "Implanted helical dipole antenna for UHF band applications". *2012 International Symposium on Antennas and Propagation (ISAP)*, **2012**, 1256–1259.
295. O.H. Murphy, C.N. McLeod, M. Navaratnarajah, M. Yacoub, C. Toumazou. "A Pseudo-Normal-Mode Helical Antenna for Use With Deeply Implanted Wireless Sensors". *IEEE Transactions on Antennas and Propagation*, **2012**, 60(2), 1135–1139. DOI: 10.1109/TAP.2011.2173106

296. Basari, D.C. Irait, F.Y. Zulkifli, E.T. Rahardjo. "A helical folded dipole antenna for medical implant communication applications". *2013 IEEE MTT-S International Microwave Workshop Series on RF and Wireless Technologies for Biomedical and Healthcare Applications, IMWS-BIO 2013 - Proceedings*, **2013**, 8–10. DOI: 10.1109/IMWS-BIO.2013.6756247
297. P. Anacleto, E. Gultepe, S. Gomes, P.M. Mendes, D.H. Gracias. "Self-folding microcube antennas for wireless power transfer in dispersive media". *Technology*, **2016**, 4(2), 120–129. DOI: 10.1142/S2339547816500047
298. P. Anacleto, P.M. Mendes, E. Gultepe, D.H. Gracias. "3D small antenna for energy harvesting applications on implantable micro-devices", In 2012 IEEE Loughborough Antennas & Propagation Conference (LAPC); **2012**, 1–4. DOI: 10.1109/LAPC.2012.6402975
299. R. Bashirullah, N. Euliano. "Capsule antennas for medication compliance monitoring", In 2009 IEEE Radio and Wireless Symposium; IEEE, **2009**, 123–126. DOI: 10.1109/RWS.2009.4957300
300. H. Yu, G.S.S. Irby, D.M.M. Peterson, M.-T. Nguyen, G. Flores, N. Euliano, R. Bashirullah. "Printed capsule antenna for medication compliance monitoring". *Electronics Letters*, **2007**, 43(22), 1179. DOI: 10.1049/el:20072204
301. O.G. Schmidt, K. Eberl. "Nanotechnology: Thin solid films roll up into nanotubes". *Nature*, **2001**, 410(6825), 168–168. DOI: 10.1038/35065525
302. D.J. Bell, L. Dong, B.J. Nelson, M. Golling. "Fabrication and Characterization of Three-Dimensional InGaAs / GaAs Nanosprings". *Nano*, **2006**
303. S.M. Harazim, W. Xi, C.K. Schmidt, S. Sanchez, O.G. Schmidt. "Fabrication and applications of large arrays of multifunctional rolled-up SiO/SiO₂ microtubes". *Journal of Materials Chemistry*, **2012**, 22(7), 2878. DOI: 10.1039/c1jm14800a
304. L. Ionov. "Soft microorigami: self-folding polymer films". *Soft Matter*, **2011**, 7(15), 6786. DOI: 10.1039/c1sm05476g
305. F. Ongaro, S. Scheggi, C. Yoon, F. Van den Brink, S.H. Oh, D.H. Gracias, S. Misra. "Autonomous planning and control of soft untethered grippers in unstructured environments". *Journal of Micro-Bio Robotics*, **2016**, 1, 1–9. DOI: 10.1007/s12213-016-0091-1
306. D. Sobel. "Longitude", Fourth Estate, London, **1995**
307. V.Y. Prinz, V.A. Seleznev, A.K. Gutakovskiy, A.V. Chehovskiy, V.V. Preobrazhenskii, M.A. Putyato, T.A. Gavrilova. "Free-standing and overgrown InGaAs/GaAs nanotubes, nanohelices and their arrays". *Physica E*, **2000**, 6, 828–831.
308. T. Huang, Z. Liu, G. Huang, R. Liu, Y. Mei. "Grating-structured metallic microsprings". *Nanoscale*, Royal Society of Chemistry, **2014**, 6(16), 9428–35. DOI: 10.1039/C4NR00316K
309. J.H. Cho, D. Datta, S.Y. Park, V.B. Shenoy, D.H. Gracias. "Plastic deformation drives wrinkling, saddling, and wedging of annular bilayer nanostructures". *Nano Letters*, **2010**, 10(12), 5098–5102. DOI: 10.1021/nl1035447
310. J.H. Cho, T. James, D.H. Gracias. "Curving nanostructures using extrinsic stress". *Advanced Materials*, **2010**, 22(21), 2320–2324. DOI: 10.1002/adma.200904410
311. E. Bermúdez Ureña, Y. Mei, E. Coric, D. Makarov, M. Albrecht, O.G. Schmidt. "Fabrication of ferromagnetic rolled-up microtubes for magnetic sensors on fluids". *Journal of Physics D: Applied Physics*, **2009**, 42(5), 55001. DOI: 10.1088/0022-3727/42/5/055001

References

312. G. Huang, Y. Mei, D.J. Thurmer, E. Coric, O.G. Schmidt. "Rolled-up transparent microtubes as two-dimensionally confined culture scaffolds of individual yeast cells.". *Lab on a chip*, **2009**, *9*, 263–268. DOI: 10.1039/b810419k
313. S. Böttner, S. Li, M.R. Jorgensen, O.G. Schmidt, S. Böttner, S. Li, M.R. Jorgensen, O.G. Schmidt. "Vertically aligned rolled-up SiO₂ optical microcavities in add-drop configuration". *Applied Physics Letters*, **2013**, *102*(25), 251119. DOI: 10.1063/1.4812661
314. D.J. Thurmer, C.C. Bof Bufon, C. Deneke, O.G. Schmidt. "Nanomembrane-Based Mesoscopic Superconducting Hybrid Junctions". *Nano Letters*, **2010**, *10*(9), 3704–3709. DOI: 10.1021/nl1022145
315. C. Deneke, C. Müller, N.Y. Jin-Phillipp, O.G.G. Schmidt. "Diameter scalability of rolled-up In (Ga) As / GaAs nanotubes". *Semiconductor science and technology*, **2002**, *17*, 1278–1281.
316. S.K. Srivastava, M. Guix, O.G. Schmidt. "Wastewater Mediated Activation of Micromotors for Efficient Water Cleaning". *Nano Letters*, **2016**, *16*(1), 817–821. DOI: 10.1021/acs.nanolett.5b05032
317. C.C.C. Bof Bufon, J.D. Cojal González, D.J. Thurmer, D. Grimm, M. Bauer, O.G. Schmidt, J.D. Cojal González, D.J. Thurmer, D. Grimm, ... O.G. Schmidt. "Self-assembled ultra-compact energy storage elements based on hybrid nanomembranes". *Nano Letters*, **2010**, *10*(7), 2506–2510. DOI: 10.1021/nl1010367
318. R. Sharma, C.C.B. Bufon, D. Grimm, R. Sommer, A. Wollatz, J. Schadewald, D.J. Thurmer, P.F. Siles, M. Bauer, O.G. Schmidt. "Large-area rolled-up nanomembrane capacitor arrays for electrostatic energy storage". *Advanced Energy Materials*, **2014**, *4*(9), 1–8. DOI: 10.1002/aenm.201301631
319. W. Si, I. Mönch, C. Yan, J. Deng, S. Li, G. Lin, L. Han, Y. Mei, O.G. Schmidt. "A single rolled-Up Si tube battery for the study of electrochemical kinetics, electrical conductivity, and structural integrity". *Advanced Materials*, **2014**, *26*(47), 7973–7978. DOI: 10.1002/adma.201402484
320. A. Vlada, A.L.M. Reddy, A. Ajayana, N. Singha, J.-F. Gohyc, S. Melinteb, P.M. Ajayan. "Roll up nanowire battery from silicon chips". *Proceedings of the National Academy of Sciences*, **2012**, *109*(38), 15168–15173. DOI: 10.1073/pnas.1208638109
321. A. Madani, S.M. Harazim, V.A. Bolaños Quiñones, M. Kleinert, A. Finn, E.S. Ghareh Naz, L. Ma, O.G. Schmidt. "Optical microtube cavities monolithically integrated on photonic chips for optofluidic sensing". *Optics Letters*, **2017**, *42*(3), 486. DOI: 10.1364/OL.42.000486
322. W. Xi, C.K. Schmidt, S. Sanchez, D.H. Gracias, R.E. Carazo-Salas, R. Butler, N. Lawrence, S.P. Jackson, O.G. Schmidt. "Molecular Insights into Division of Single Human Cancer Cells in On-Chip Transparent Microtubes". *ACS Nano*, **2016**, *10*(6), 5835–5846. DOI: 10.1021/acs.nano.6b00461
323. B. Koch, A.K. Meyer, L. Helbig, S.M. Harazim, A. Storch, S. Sanchez, O.G. Schmidt. "Dimensionality of Rolled-up Nanomembranes Controls Neural Stem Cell Migration Mechanism". *Nano Letters*, **2015**, *15*(8), 5530–5538. DOI: 10.1021/acs.nanolett.5b02099
324. M. Medina-Sanchez, B. Ibarlucea, N. Perez, D.D. Karnaushenko, S.M. Weiz, L. Baraban, G. Cuniberti, O.G. Schmidt. "High-performance three-dimensional tubular nanomembrane sensor for DNA detection". *Nano Letters*, **2016**, *16*(7), 4288–4296. DOI: 10.1021/acs.nanolett.6b01337
325. C.S. Martinez-Cisneros, S. Sanchez, W. Xi, O.G. Schmidt. "Ultracompact three-dimensional tubular conductivity microsensors for ionic and biosensing applications". *Nano Letters*, **2014**,

- 14(4), 2219–2224. DOI: 10.1021/nl500795k
326. S. Xu, Z. Yan, K.-I.K.-I. Jang, W. Huang, H. Fu, J. Kim, Z. Wei, M. Flavin, J. McCracken, ... J.A. Rogers. "Assembly of micro/nanomaterials into complex, three-dimensional architectures by compressive buckling". *Science*, American Association for the Advancement of Science, **2015**, 347(6218), 154–159. DOI: 10.1126/science.1260960
327. E.J. Smith, D. Makarov, O.G. Schmidt. "Polymer delamination: towards unique three-dimensional microstructures". *Soft Matter*, **2011**, 7(24), 11309. DOI: 10.1039/c1sm06416a
328. G. Stoychev, N. Pureskiy, L. Ionov. "Self-folding all-polymer thermoresponsive microcapsules". *Soft Matter*, **2011**, 7(7), 3277. DOI: 10.1039/c1sm05109a
329. N. Bassik, B.T. Abebe, K.E. Laflin, D.H. Gracias. "Photolithographically patterned smart hydrogel based bilayer actuators". *Polymer*, **2010**, 51(26), 6093–6098. DOI: 10.1016/j.polymer.2010.10.035
330. C.L. Randall, E. Gultepe, D.H. Gracias. "Self-folding devices and materials for biomedical applications". *Trends in Biotechnology*, Elsevier Ltd, **2012**, 30(3), 138–146. DOI: 10.1016/j.tibtech.2011.06.013
331. Y. V. Kalinin, J.S. Randhawa, D.H. Gracias. "Three-dimensional chemical patterns for cellular self-organization". *Angewandte Chemie - International Edition*, **2011**, 50(11), 2549–2553. DOI: 10.1002/anie.201007107
332. J.H. Cho, M.D. Keung, N. Verellen, L. Lagae, V. V. Moshchalkov, P. Van Dorpe, D.H. Gracias. "Nanoscale origami for 3D optics". *Small*, **2011**, 7(14), 1943–1948. DOI: 10.1002/sml.201100568
333. T.G. Leong, A.M. Zarafshar, D.H. Gracias. "Three-dimensional fabrication at small size scales". *Small*, **2010**, 6(7), 792–806. DOI: 10.1002/sml.200901704
334. M. Jamal, A.M. Zarafshar, D.H. Gracias. "Differentially photo-crosslinked polymers enable self-assembling microfluidics (Supplementary Information)". *Nature communications*, **2011**, 2, 527. DOI: 10.1038/ncomms1531
335. Q. Zhang, K. Zhang, G. Hu. "Smart three-dimensional lightweight structure triggered from a thin composite sheet via 3D printing technique". *Scientific reports*, Nature Publishing Group, **2016**, 6(November 2015), 22431. DOI: 10.1038/srep22431
336. C. Yoon, R. Xiao, J. Park, J. Cha, T.D. Nguyen, D.H. Gracias. "Functional stimuli responsive hydrogel devices by self-folding". *Smart Materials and Structures*, IOP Publishing, **2014**, 23(9), 94008. DOI: 10.1088/0964-1726/23/9/094008
337. H.-W. Huang, M.S. Sakar, A.J. Petruska, S. Pane, B.J. Nelson. "Soft micromachines with programmable motility and morphology". *Nat Commun*, **2016**, 7, 1–10. DOI: 10.1038/ncomms12263
338. M. Yang, B. Liu, G. Gao, X. Liu, F. Liu. "Poly(maleic anhydride-co-acrylic acid)/poly(ethylene glycol) hydrogels with pH- and ionic-strength-responses". *Chinese Journal of Polymer Science*, **2010**, 28(6), 951–959. DOI: 10.1007/s10118-010-9191-x
339. W.R.K. Illeperuma, J.-Y. Sun, Z. Suo, J.J. Vlassak. "Force and stroke of a hydrogel actuator". *Soft Matter*, **2013**, 9(35), 8504–8511. DOI: 10.1039/c3sm51617b
340. K. Song, E. Yeom, S.J. Seo, K. Kim, H. Kim, J.H. Lim, S. Joon Lee. "Journey of water in pine cones". *Scientific Reports*, **2015**, 5(1), 9963. DOI: 10.1038/srep09963

References

341. W. Jung, W. Kim, H.Y. Kim. "Self-burial mechanics of hygroscopically responsive awns". *Integrative and Comparative Biology*, **2014**, 54(6), 1034–1042. DOI: 10.1093/icb/icu026
342. M. Rüggeberg, I. Burgert. "Bio-Inspired wooden actuators for large scale applications". *PLoS ONE*, **2015**, 10(4), 1–16. DOI: 10.1371/journal.pone.0120718
343. S.A. Evenson, C.A. Fail, J.P.S. Badyal. "Surface esterification of poly(ethylene-alt-maleic anhydride) copolymer". *Journal of Physical Chemistry B*, **2000**, 104(45), 10608–10611. DOI: 10.1021/jp002059y
344. R. Streubel, L. Han, F. Kronast, A. a. Ünal, O.G. Schmidt, D. Makarov. "Imaging of buried 3D magnetic rolled-up nanomembranes". *Nano Letters*, **2014**, 14(7), 3981–3986. DOI: 10.1021/nl501333h
345. T. Deng, C. Yoon, Q. Jin, M. Li, Z. Liu, D.H. Gracias. "Self-folding graphene-polymer bilayers". *Applied Physics Letters*, **2015**, 106(20) DOI: 10.1063/1.4921530
346. K. Yang, R. Torah, Y. Wei, S. Beeby, J. Tudor. "Water Based PVA Sacrificial Material for Low Temperature MEMS Fabrication and Applications on e-textiles". *Procedia Engineering*, Elsevier B.V., **2014**, 87, 1565–1568. DOI: 10.1016/j.proeng.2014.11.599
347. V. Linder, B.D. Gates, D. Ryan, B.A. Parviz, G.M. Whitesides. "Water-soluble sacrificial layers for surface micromachining". *Small*, **2005**, 1(7), 730–736. DOI: 10.1002/sml.200400159
348. R. Fernandes, M. Zuniga, F.R. Sassine, M. Karakoy, D.H. Gracias. "Enabling cargo-carrying bacteria via surface attachment and triggered release". *Small*, **2011**, 7(5), 588–592. DOI: 10.1002/sml.201002036
349. F. Bouyer, N. Sanson, M. Destarac, C. Gerardin. "Hydrophilic block copolymer-directed growth of lanthanum hydroxide nanoparticles". *New J. Chem.*, **2006**, 30(3), 399–408. DOI: 10.1039/b516368d
350. C.M. Roland. "Encyclopedia of Polymeric Nanomaterials". *Encyclopedia of Polymeric Nanomaterials*, **2014**, 1–9. DOI: 10.1007/978-3-642-36199-9
351. S. Swann. "Magnetron sputtering". *Physics in Technology*, **1988**, 19(2), 67–75. DOI: 10.1088/0305-4624/19/2/304
352. D.B. Asay, S.H. Kim. "Evolution of the Adsorbed Water Layer Structure on Silicon Oxide at Room Temperature". *The Journal of Physical Chemistry B*, **2005**, 109(35), 16760–16763. DOI: 10.1021/jp053042o
353. T. Takahagi, H. Sakaue, S. Shingubara. "Adsorbed Water on a Silicon Wafer Surface Exposed to Atmosphere". *Japanese Journal of Applied Physics*, **2001**, 40(11), 6198–6201.
354. C.A. Schlecht, J.A. Maurer. "Functionalization of glass substrates: mechanistic insights into the surface reaction of trialkoxysilanes". *RSC Advances*, **2011**, 1(8), 1446. DOI: 10.1039/c1ra00421b
355. Dow Corning. "Silane Coupling Agents The Concept of Coupling with". **2009**
356. B. Hafner. "Scanning Electron Microscopy Primer", University of Minnesota, **2007**
357. W.H. Kuo, M. Briceno, D. Ozkaya. "Characterisation of Catalysts Using Secondary and Backscattered Electron In-lens Detectors". *Platinum Metals Review*, **2014**, 58(2), 106–110. DOI: 10.1595/147106714X680113

358. D. Makarov, D. Karnaushenko, O.G. Schmidt. "Printable Magnetolectronics". *ChemPhysChem*, **2013**, 14(9), 1771–1776.
359. D.D. Karnaushenko, D.D. Karnaushenko, D. Makarov, O.G. Schmidt. "Compact helical antenna for smart implant applications". *NPG Asia Materials*, Nature Publishing Group, **2015**, 7(6), e188. DOI: 10.1038/am.2015.53
360. D. Karnaushenko, D. Makarov, M. Stöber, D.D. Karnaushenko, S. Baunack, O.G. Schmidt. "High-Performance Magnetic Sensorics for Printable and Flexible Electronics". *Advanced Materials*, Wiley Online Library, **2015**, 27(5), 880–885. DOI: 10.1002/adma.201403907
361. M. Melzer, J.I. Mönch, D. Makarov, Y. Zabala, G.S. Cañón Bermúdez, D. Karnaushenko, S. Baunack, F. Bahr, C. Yan, ... O.G. Schmidt. "Wearable Magnetic Field Sensors for Flexible Electronics". *Advanced Materials*, Wiley Online Library, **2015**, 27(7), 1274–1280. DOI: 10.1002/adma.201405027
362. M. Melzer, D. Karnaushenko, G. Lin, S. Baunack, D. Makarov, O.G. Schmidt. "Direct Transfer of Magnetic Sensor Devices to Elastomeric Supports for Stretchable Electronics". *Advanced Materials*, Wiley Online Library, **2015**, 27(8), 1333–1338. DOI: 10.1002/adma.201403998
363. A.M. Wilson, P.J. Bailey, P.A. Tasker, J.R. Turkington, R.A. Grantb, J.B. Love, The. "Solvent extraction: the coordination chemistry behind extractive metallurgy". *Chem. Soc. Rev.*, **2014**, 43(1), 123–134. DOI: 10.1039/C3CS60275C
364. A. Richter, G. Paschew, S. Klatt, J. Lienig, K.F. Arndt, H.J.P. Adler. "Review on Hydrogel-based pH Sensors and Microsensors". *Sensors*, **2008**, 8(1), 561–581. DOI: 10.3390/s8010561
365. Y. Qiu, K. Park. "Environment-sensitive hydrogels for drug delivery". *Advanced Drug Delivery Reviews*, **2012**, 64, 321–339. DOI: 10.1016/j.addr.2012.09.024
366. R.A. Gemeinhart, J.U.N. Chen, H. Park, K. Park. "pH-sensitivity of fast responsive superporous hydrogels". *Journal of biomaterials science. Polymer edition*, **2000**, 11(12), 1371–1380. DOI: 10.1163/156856200744390
367. R. Marcombe, S. Cai, W. Hong, X. Zhao, Y. Lapusta, Z. Suo. "A theory of constrained swelling of a pH-sensitive hydrogel". *Soft Matter*, **2010**, 6(4), 784. DOI: 10.1039/b917211d
368. J.K. Chen, C.J. Chang. "Fabrications and Applications of Stimulus-Responsive Polymer Films and Patterns on Surfaces: A Review". *Materials*, **2014**, 7(2), 805–875. DOI: 10.3390/ma7020805
369. S. Dubinsky, G.S. Grader, G.E. Shter, M.S. Silverstein. "Thermal degradation of poly(acrylic acid) containing copper nitrate". *Polymer Degradation and Stability*, **2004**, 86(1), 171–178. DOI: 10.1016/j.polymdegradstab.2004.04.009
370. G.T. Castro, S.E. Blanco, O.S. Giordano. "UV spectral properties of benzophenone. Influence of solvents and substituents". *Molecules*, **2000**, 5(3), 424–425. DOI: 10.3390/50300424
371. P. Xiao, F.F. Dumur, B. Graff, D. Gigmes, J.P. Fouassier, J. Lalevée, J. Lalevée. "Variations on the benzophenone skeleton: Novel high performance blue light sensitive photoinitiating systems". *Macromolecules*, **2013**, 46(19), 7661–7667. DOI: 10.1021/ma401766v
372. A. Hou, G. Feng, J. Zhuo, G. Sun. "UV Light-Induced Generation of Reactive Oxygen Species and Antimicrobial Properties of Cellulose Fabric Modified by 3,3',4,4'-Benzophenone Tetracarboxylic Acid". *ACS Applied Materials & Interfaces*, **2015**, 7(50), 27918–27924. DOI: 10.1021/acsami.5b09993

References

373. K. Othmer. "Kirk-Othmer Encyclopedia of Chemical Technology", John Wiley & Sons, Inc., Hoboken, NJ, USA, **2000**, DOI: 10.1002/0471238961
374. B.S. Furniss, A.J. Hannaford, P.W.G. Smith, A.R. Tatchell. "Vogel's textbook of practical organic chemistry", Fifth edit John Wiley & Sons, Inc., New York, USA, **1989**
375. S. Kaufman, C.R. Singleterry. "The Reaction between Tertiary Amines and Organic Acids in Non-polar Solvents". *The Journal of Physical Chemistry*, **1952**, 56(5), 604–610. DOI: 10.1021/j150497a011
376. Y.K. Cheung, B.M. Gillette, M. Zhong, S. Ramcharan, S.K. Sia. "Direct patterning of composite biocompatible microstructures using microfluidics". *Lab on a chip*, **2007**, 7(5), 574–579. DOI: 10.1039/b700869d
377. M.A. Muter. "Synthesis and Biocompatibility of New Contact Lenses Based On Derivatives of 2-Hydroxy Ethyl Meth Acrylate and 2-Ethyl Hexyl Methacrylate". **2015**, 3(3), 152–160.
378. J.W. Choi, R. Wicker, S.H. Lee, K.H. Choi, C.S. Ha, I. Chung. "Fabrication of 3D biocompatible/biodegradable micro-scaffolds using dynamic mask projection microstereolithography". *Journal of Materials Processing Technology*, **2009**, 209(15), 5494–5503. DOI: 10.1016/j.jmatprotec.2009.05.004
379. J.L. Ferracane. "Current trends in dental composites". *Critical Reviews in Oral Biology and Medicine*, **1995**, 6(4), 302–318. DOI: 10.1177/10454411950060040301
380. M. Jorfi, M.N. Roberts, E.J. Foster, C. Weder. "Physiologically responsive, mechanically adaptive bio-nanocomposites for biomedical applications". *ACS Applied Materials and Interfaces*, ACS Publications, **2013**, 5(4), 1517–1526. DOI: 10.1021/am303160j
381. S.C. Bayne. "Jada Landmark Series.". *Journal of the American Dental Association (JADA)*, **2013**, 144(8), 880–884.
382. M.W. Cole, E. Ngo, C. Hubbard, S.G. Hirsch, M. Ivill, W.L. Sarney, J. Zhang, S.P. Alpay. "Enhanced dielectric properties from barium strontium titanate films with strontium titanate buffer layers". *Journal of Applied Physics*, **2013**, 114(16), 164107. DOI: 10.1063/1.4827421
383. A. Wypych, I. Bobowska, M. Tracz, A. Opasinska, S. Kadlubowski, A. Krzywania-Kaliszewska, J. Grobelny, P. Wojciechowski. "Dielectric Properties and Characterisation of Titanium Dioxide Obtained by Different Chemistry Methods". *Journal of Nanomaterials*, **2014**, 2014(124814), 1–9. DOI: 10.1155/2014/124814
384. C. Goldsmith. "Measurement of stresses generated in cured polyimide films". *Journal of Vacuum Science & Technology A: Vacuum, Surfaces, and Films*, **1983**, 1(2), 407. DOI: 10.1116/1.571931
385. G. Stoychev. "Shape-programmed folding of stimuli-responsive polymer bilayers", Technische Universität Dresden, **2013**
386. S.W. Cranford, C. Ortiz, M.J. Buehler. "Mechanomutable properties of a PAA/PAH polyelectrolyte complex: rate dependence and ionization effects on tunable adhesion strength". *Soft Matter*, **2010**, 6(17), 4175. DOI: 10.1039/c0sm00095g
387. D. Abegg, N. Calo, E. Mazamay, P. Surriabre. "Analytical Chemistry II Potentiometric Titration", Universite de Geneve, **2008**
388. G. Vazquez, E. Alvarez, J.M. Navaza. "Surface Tension of Alcohol + Water from 20 to 50 °C". *Journal of Chemical & Engineering Data*, **1995**, 40(3), 611–614. DOI: 10.1021/je00019a016

-
389. A.P. Slobozhanyuk, M. Lapine, D.A. Powell, I. V. Shadrivov, Y.S. Kivshar, R.C. McPhedran, P.A. Belov. "Flexible helices for nonlinear metamaterials". *Advanced Materials*, **2013**, 25(25), 3409–3412. DOI: 10.1002/adma.201300840
390. A.M. Kemoli, W.E. Van Amerongen. "Influence of the cavity-size on the survival rate of proximal ART restorations in primary molars". *International Journal of Paediatric Dentistry*, **2009**, 19(6), 423–430. DOI: 10.1111/j.1365-263X.2009.01013.x
391. E.M. Darling, R.E. Wilusz, M.P. Bolognesi, S. Zauscher, F. Guilak. "Biomechanical Properties of Articular Cartilage Pericellular Matrix Measured in situ via Atomic Force Microscopy 1,2". *55th Annual Meeting of the Orthopaedic Research Society*, **2009**, 147, 1–1.
392. T.J. Hall, M. Bilgen, M.F. Insana, T.A. Krouskop. "Phantom materials for elastography". *IEEE Transactions on Ultrasonics, Ferroelectrics, and Frequency Control*, **1997**, 44(6), 1355–1365. DOI: 10.1109/58.656639
393. L. Petti, N. Münzenrieder, C. Vogt, H. Faber, L. Büthe, G. Cantarella, F. Bottacchi, T.D. Anthopoulos, G. Tröster. "Metal oxide semiconductor thin-film transistors for flexible electronics". *Applied Physics Reviews*, **2016**, 3(2) DOI: 10.1063/1.4953034
394. J. Zhang, Y. Li, B. Zhang, H. Wang, Q. Xin, A. Song. "Flexible indium–gallium–zinc–oxide Schottky diode operating beyond 2.45 GHz". *Nature Communications*, **2015**, 6, 7561. DOI: 10.1038/ncomms8561
395. Y. Mei, A.A. Solovev, S. Sanchez, O.G. Schmidt. "Rolled-up nanotech on polymers: from basic perception to self-propelled catalytic microengines". *Chemical Society Reviews*, **2011**, 40(5), 2109. DOI: 10.1039/c0cs00078g

List of figures

Figure 1.1: Information delivery over long distances in past times.	3
Figure 1.2: Fast long range communication.	4
Figure 1.3: From imagination to reality.	4
Figure 2.1: Evolution of the implantable cardiac device.	12
Figure 2.2: Conceptual view on the medical care system.	13
Figure 2.3: Implantable sensors and drug delivery systems.	14
Figure 2.4: Different types of neurological devices.	16
Figure 2.5: Dielectric constant and losses of water as function of frequency	21
Figure 2.6: Resonance shift in the dielectric material.	23
Figure 2.7: Realization of physically and electrically small antennas.....	25
Figure 2.8: Rolled-up technology.	30
Figure 2.9: Stimuli responsive structures.....	31
Figure 3.1: Profile of slopes for conventional photoresists.....	35
Figure 3.2: Construction of the electron beam evaporation device.....	36
Figure 3.3: Simplified representation of the magnetron sputtering system.....	37
Figure 3.4: Chemical layer deposition.....	39
Figure 3.5: Stylus profilometry.....	40
Figure 3.6: Schematic representation of the network analyzer.	41
Figure 3.7: Construction of a scanning electron microscope.....	42
Figure 4.1: Synthesis steps for the sacrificial polymer material.	46
Figure 4.2: Illustrates synthesis steps for stimuli responsive polymer material.	47
Figure 4.3: Illustrate synthesis steps for the polyimide material.	49
Figure 4.4: Different attachment mechanisms of the PI layer to the HG layer.....	50
Figure 4.5: Illustrates synthesis steps of bottom resist for bi-layer photolithographic process.....	51
Figure 4.6: Dimer of carboxylic acids in the presence of tertiary amine.	52
Figure 5.1: Model for high frequency simulation.	56
Figure 5.2: Fabrication process of self-assembled helical antennas.	57

List of figures

Figure 5.3: Model of the compact helical antenna.....	58
Figure 5.4: Resonance frequency as a function of the wire thickness respect to its conductivity.	58
Figure 5.5: Parametric simulation of compact helical antenna characteristics.....	59
Figure 5.6: Number of windings versus tube diameter.....	60
Figure 5.7: Distribution of the intensity of the magnetic field.....	60
Figure 5.8: Influence of dielectric material on resonance frequency.	61
Figure 5.9: Targeting in vivo applications.....	63
Figure 5.10: The S ₁₁ parameter of the helical antenna for different impedances.....	64
Figure 5.11: Typical fails in self-assembly process for structures having big aspect ratios.	65
Figure 5.12: FEM model for investigation of self-assembling behaviour.....	66
Figure 5.13: FEM model for investigation of crack propagation behaviour.	67
Figure 5.14: Comparative results between single and double layer structures.....	68
Figure 5.15: Linker braking behaviour in real experiments and in simulations.....	69
Figure 5.16: A sample after polymers patterning process.....	72
Figure 5.17: Double layer photolithographic process.....	73
Figure 5.18: Sample after the bi-layer photolithographic process.	74
Figure 5.19: Set-up developed for assisting the self-assembly process.....	75
Figure 5.20: Experimental realization of helical antennas.....	76
Figure 5.21: Antenna encapsulation process.....	77
Figure 5.22: Parameters of the encapsulation solution.....	78
Figure 5.23: Measurement of S ₁₁ parameters for self-assembled helical antennas.....	79
Figure 5.24: RF performance of encapsulated antennas.....	80
Figure 5.25: Experiment demonstrating signal transmission from a smartphone to the antenna.	81
Figure 5.26: Concept of a smart implant for in-body applications.	82
Figure 5.27: Implanted antenna into a bio-mimicking polymeric matrix.....	83

List of tables

Table 1. Various antennas reported in the literature for MICS, ISM and WiBAN applications.	27
Table 2. Various antennas reported in the literature for ISM 2.45 GHz radio band.	28
Table 3. Dielectric parameters for the human head model.	62

Selbständigkeitserklärung

Hiermit versichere ich, dass ich die vorliegende Arbeit ohne unzulässige Hilfe Dritter und ohne Benutzung anderer als der angegebenen Hilfsmittel angefertigt habe; die aus fremden Quellen direkt oder indirekt übernommenen Gedanken sind als solche kenntlich gemacht. Bei der Auswahl und Auswertung des Materials sowie bei der Herstellung des Manuskripts habe ich Unterstützungsleistungen von folgenden Personen erhalten:

Prof. Dr. Oliver G. Schmidt

Dr. Denys Makarov

Daniil Karnaushenko

Weitere Personen waren an der Abfassung der vorliegenden Arbeit nicht beteiligt. Die Hilfe eines Promotionsberaters habe ich nicht in Anspruch genommen. Weitere Personen haben von mir keine geldwerten Leistungen für Arbeiten erhalten, die im Zusammenhang mit dem Inhalt der vorgelegten Dissertation stehen. Die Arbeit wurde bisher weder im Inland noch im Ausland in gleicher oder ähnlicher Form einer anderen Prüfungsbehörde vorgelegt.

Datum der Einreichung

Unterschrift des Bewerbers

Acknowledgements

Finally, it is the right time to recall all the people, who has helped, supported and motivated me during my Ph.D. work and without whom it would be difficult or almost impossible to finish my thesis.

At first, I would like to express my greatest gratitude to my supervisor Prof. Oliver G. Schmidt (head of the Institute for Integrative Nanosciences (IIN) at IFW Dresden) and my second supervisor Dr. Denys Makarov. For a great chance to work in the warm and friendly environment that they provided to me. With whom I could extend my field of knowledge and experience in research and development of the multidisciplinary scientific project. For their kind support, guidance and motivation along my work.

I am also thankful to Prof. Dr. Jeroen van den Brink and Dr. Manuel Richter from Institut für Theoretische Festkörperphysik (ITF) for the access to their high performance computational cluster system. Additional thanks go to Ulrike Nitzsche and Thomas Fichte for their great technical support with the installation and maintenance of ANSYS FEM tool.

I would like to thank Dr. Alexey Shaporin (Fraunhofer ENAS), with whom I had many useful technical discussions about the working principle of the mechanical FEM simulation software, during which I have got a clear practical knowledge performing successful simulations.

My special thanks I would give to my brother Daniil Karnaushenko for our everyday working discussions, collaborative work on the polymeric platform, help in assembly process of the experimental setups. I would also like to thank his wife Olga Karnaushenko, Dr. Ivan Soldatov and his wife Svetlana for our excellent pastime during weekends and holidays.

Additional thanks to our hiwi students Michail Michailow, Christoph Schade, Simon Schlei and Alexander Kutscher who partially have assisted me in my sample preparation process.

Thanks goes to Cornelia Krien, Irina Fiering, Sebastian Seifert, Martin Bauer and Sandra Sieber for their help with metal film depositions. Here I would specially thank Ronny Engelhard whom was overloaded from my side by huge amount of technical questions and suggestions about the working principle of deposition devices, their upgrade and maintaining them at the highest working performance level.

I appreciate the help of Dr. Stefan Baunack (SEM/FIB), Barbara Eichler (AFM) and Dr. Steffen Oswald (XPS) for their help in data acquisition process. I wish to thank Dr. Jens Ingolf Mönch,

Acknowledgements

Dr. Stefan Harazim and Dr. Daniel Grimm for their kind advises at the beginning of my experience with the photolithographic process and great introduction to the cleanroom.

I would sincerely like to thank all the current group members: Michael Melzer, Christian Becker and previous members: Dr. Tobias Kosub, Martin Kopte, Dr. Gungun Lin, Santiago Cañón, Dr. Robert Streubel, Dr. Luyang Han, Max Stöber, Karsten Rost, Dr. Yevhen Zabyla, Dr. Nicolas Perez with Dr. Mariana Medina-Sanchez and other IIN members for many nice projects collaborative works, discussions, advises and corrections for my Ph.D. seminars.

Many thanks to Dr. Roman Rezaev, Dr. Pavel Leksin, Prof. Vladimir Fomin, Dr. Elliot Smith, Dr. Dominic Thurmer, Dr. Abbas Madani and Ehsan Saei Ghareh Naz with whom I have a lot of fruitful discussions during my Ph. D. life.

I would like to thank Prof. Viktor A. Gridchin (head of the Department of Semiconductors and Microelectronics at Novosibirsk State Technical University) who provided me an opportunity to begin my carrier as a researcher during my bachelor and master education.

I would like to acknowledge the funding financed in part via the European Research Council within the European Union's Seventh Framework Programme (FP7/2007–2013)/ERC grant agreement no. 306277 and German Science Foundation (DFG) grant MA 5144/2-1.

Finally, I would like to thank my parents and family members who are continuously supporting and guiding me during my life towards scientific career and motivating me during difficult periods of time.

Research achievements

List of publications (*Reverse chronological*)

1. G. Lin, **D. D. Karnaushenko**, G. S. C. Bermúdez, O. G. Schmidt, and D. Makarov.
"Magnetic Suspension Array Technology: Controlled Synthesis and Screening in Microfluidic Networks"
Small **2016**, 12(33). DOI: 10.1002/sml.201601166
2. M. Medina-Sanchez, B. Ibarlucea, N. Perez, **D. D. Karnaushenko**, S. M. Weiz, L. Baraban, G. Cuniberti, and O. G. Schmidt
"High-performance 3D tubular nanomembrane sensor for DNA detection"
Nano Letters **2016**, 16(7). DOI: 10.1021/acs.nanolett.6b01337
3. N. Münzenrieder, D. Karnaushenko, L. Petti, G. Cantarella, C. Vogt, L. Büthe, **D. D. Karnaushenko**, O. G. Schmidt, D. Makarov, and G. Tröster.
"Entirely Flexible On-Site Conditioned Magnetic Sensorics".
Adv. Electron. Mater. **2016**, 1600188. DOI: 10.1002/aelm.201600188
4. D. Karnaushenko, N. Münzenrieder, **D. D. Karnaushenko**, B. Koch, A. K. Meyer, S. Baunack, L. Petti, G. Tröster, D. Makarov, O. G. Schmidt
"Biomimetic Microelectronics for Regenerative Neuronal Cuff Implants"
Advanced Materials **2015**, 27(43), p. 6797. DOI:10.1002/adma.201503696
5. D. Karnaushenko, **D. D. Karnaushenko**, D. Makarov, S. Baunack, R. Schäfer, O. G. Schmidt
"Self-Assembled On-Chip-Integrated Giant Magneto-Impedance Sensorics"
Advanced Materials **2015**, 27(42), p. 6582. DOI: 10.1002/adma.201503127
6. **D. D. Karnaushenko**, D. Karnaushenko, D. Makarov, and O. G. Schmidt
"Rolled-up helical antenna for on-chip applications"
NPG Asia Materials **2015**, 7(e188). DOI: 10.1038/am.2015.53
7. M. Melzer, M. Kaltenbrunner, D. Makarov, **D. D. Karnaushenko**, D. Karnaushenko, T. Sekitani, T. Someya, and O. G. Schmidt
"Imperceptible magnetoelectronics"
Nature Communications **2015**, 6, 6080. DOI: 10.1038/ncomms7080
8. D. Karnaushenko, D. Makarov, M. Stöber, **D. D. Karnaushenko**, S. Baunack, and O. G. Schmidt
"High-Performance Magnetic Sensorics for Printable and Flexible Electronics"
Advanced Materials **2014**, 27(5), p. 880. DOI: 10.1002/adma.201403907
9. V. M. Fomin, E. J. Smith, **D. D. Karnaushenko**, D. Makarov, and O. G. Schmidt
"Asymmetric drag in oscillatory motion: Ratchet effect without an asymmetric potential"
Physical Review E **2013**, 87, 052122. DOI: 10.1103/PhysRevE.87.052122

Research achievements

10. L. Baraban, R. Streubel, D. Makarov, L. Han, **D. D. Karnaushenko**, O. G. Schmidt, and G. Cuniberti
“*Fuel-Free Locomotion of Janus Motors: Magnetically Induced Thermophoresis*”
ACS Nano **2013**, 7, 2, p. 1360. DOI: 10.1021/nn305726m

Cover page

1. Droplet Microfluidics: Magnetic Suspension Array Technology: Controlled Synthesis and Screening in Microfluidic Networks. **Cover page doi: 10.1002/sml.201670167**



Accepted patents

1. D. Karnaushenko, **D. D. Karnaushenko**, and I. I. Lee: "Multicontact hybrid interconnection", 18 Feb. 2008, RU2363072C1.
2. D. Karnaushenko, **D. D. Karnaushenko**, V. G. Polovinkin, and I. I. Lee: "Multicontact hybrid interconnection", 27 Oct. 2008, RU2383966C1.

List of oral presentations

1. "Compact helical antenna for smart implant applications", Fachverband Biologische Physik: Biotechnology & Bioengineering (BP44), Regensburg (Germany): 6. - 11. March, 2016.
2. "Compact rolled-up antenna for implants applications", Fachverband Metall- und Materialphysik: Sensors and Actuators (MM16), Berlin (Germany): 15. - 20. March, 2015.
3. "Rolled-up antenna for on-chip application", Fachverband Dünne Schichten: Sensoric Micro and Nano-systems II (DS16), Dresden (Germany): 30. March - 4. April, 2014.

List of poster sessions

1. **D. D. Karnaushenko**, D. Karnaushenko, D. Makarov, O. G. Schmidt
"Compact antenna for on-chip and smart implant applications". **Best poster award.**
581. Wilhelm und Else Heraeus-Seminar "Flexible, Stretchable and Printable High-performance Electronics", Bad Honnef (Germany): 12–14 January, 2015.
2. **D. D. Karnaushenko**, D. Makarov, O. G. Schmidt
"Rolled-up antenna for on chip applications"
526. Wilhelm und Else Heraeus-Seminar "Functional Magnetic Nanomembranes", Bad Honnef (Germany): 4–6 March, 2013.
3. **D. D. Karnaushenko**, D. Makarov and O. G. Schmidt
"Compact rolled-up antenna for on-chip applications"
IFW Winter School, Oberwiesenthal, Germany, 20–23 January, 2013.

Theses

1. Electromagnetic simulations could completely predict and fit experimental realization of the self-assembled helical antenna.
2. The resonance shift comes to saturation already at small values of dielectric constants for the encapsulation material.
3. The helical antenna experiences shift of the resonance from 5.8 GHz (in a free space) to 2.4 GHz in the human body after the implantation process.
4. The helical antenna could operate either in 5.8 or 2.4 GHz ISM frequency band.
5. If an implant considered to be used at 5.8 GHz, antenna dimensions could be two time smaller.
6. The experiment demonstrates possibility to receive signals from a smartphone or detect reflected signal from the passive antenna.
7. According to standards the simulation demonstrates acceptable SAR level in human tissues.
8. Mechanical simulations could predict physical behavior of large-scale polymeric tubular structures during the self-assembling process.
9. Mechanical simulations give clear understanding for the rolling process of planar polymeric films into tubular structures having different aspect ratios to their curvature.
10. Structures with length smaller than the curvature and the width could be self-assembled into the tube with a well-defined way.
11. The aspect ratio of the planar structure could be artificially limited by introduction of linkers.
12. The optimized design of linkers could significantly improve yield of tubular structures and their self-assembly.
13. The mechanical guidance device introduces further improvement in fabrication yield.
14. The polymeric technology demonstrates superior $\sim 100\%$ yield of self-assembled tubular structures.
15. Fine radius tuning of helical antennas can be done in solutions having different pH levels.
16. The sacrificial frame solution significantly simplifies and improves yield of structures at the encapsulation step.
17. The encapsulation material possesses variable dielectric constant and mechanical stability.
18. The self-assembled helical antennas demonstrate superior scale reduction compared to other antenna types.
19. Mechanical stability of the self-assembled antennas allow implantation via injection.
20. The fabrication process of antennas is compatible with micro fabrication methods, i.e. CMOS.

Curriculum-Vitae

Personal Information

Name Dmitriy Karnaushenko
Day of birth 04.03.1986
Place of birth Novokuznetsk, Russia (USSR)

Education

- Present **Ph.D. candidate** at Institute for Integrative Nanosciences
Sep. 2011 Topic: "Compact helical antenna for smart implant applications"
Leibniz Institute for Solid State and Materials Research in Dresden (Germany)
Supervisors: Prof. Oliver G. Schmidt and Dr. Denys Makarov
- Jul. 2011 **Research assistant** at Physics Department of the Faculty of Natural Sciences
Oct. 2009 Topic: "Investigation of physical and chemical processes in lithium-ion batteries using
chronopotentiometry and impedancometry"
Department of the Electronic Devices. Radio Engineering Faculty of the Novosibirsk State
Technical University, Novosibirsk, (Russian Federation)
Supervisors: Prof. Dr. V. K. Makukha and Dr. N. V. Kosova
- Sep. 2009 DAAD-Summer-Academy "Structure formation - From a Cloud of Atoms to a Crystal"
Technical University of Chemnitz (Germany)
- Jun. 2009 **Master of Science in Electronic and Microelectronic Engineering.**
Sep. 2007 Topic: "Development and realization of infrared scanning microscope"
Department of Semiconductor Devices and Microelectronics.
State Technical University of Novosibirsk (Russian Federation)
Supervisor: Dr. V. G. Polovinkin
- Jun. 2007 **Bachelor in Electronic and Microelectronic Engineering.**
Sep. 2003 Topic: "Electronic paramagnetic resonance in heterostructure with Ge/Si quantum dots"
Department of Semiconductor Devices and Microelectronics. Radio Engineering Faculty
of Novosibirsk State Technical University, Novosibirsk, (Russian Federation)

Languages

Russian: native **English:** fluent **German:** basic